MAX PLANCK INSTITUTE FOR HUMAN COGNITIVE AND BRAIN SCIENCES LEIPZIG

Gert Wollny: Analysis of Changes in Temporal Series of Medical Images. Leipzig: Max Planck Institute for Human Cognitive and Brain Sciences, 2004 (MPI Series in Human Cognitive and Brain Sciences; 43)

cc BY NC

Analysis of Changes in Temporal Series of Medical Images

Der Fakultät für Mathematik und Informatik
der Universität Leipzig
eingereichte

DISSERTATION

zur Erlangung des akademischen Grades
DOCTOR rerum naturalium
(Dr. rer. nat.)

im Fachgebiet Informatik

vorgelegt von Dipl. math. Gert Wollny
geboren am 31.08.1968 in Leipzig

Defence: Leipzig, 22.10.2003

Advisor: Dr. habil. Fritjhof Kruggel, MPI for Human Cognitive and Brain Sciences, Leipzig
Co-Reviewer: Prof. Dr. Martin Rumpf, Gerhard-Mercator-University, Duisburg
Prof. Dr. Dietmar Saupe, University of Konstanz

Abstract

This thesis focuses on the development of a tool chain to analyze time series of medical images automatically. Time series of medical images are acquired when monitoring disease progression or medical treatment by using, e.g., *magnetic resonance tomography* (MRT) or *computer tomography* (CT). If the disease or treatment induces structural change of tissue and/or bone, this change may result in differences between the images that can be quantified and further analyzed.

However, additional differences between the images may be present due to the imaging process only. They have to be eliminated prior to the quantification of relevant changes. Besides noise and artifacts, which are only discussed in brief, rigid registration is used to eliminate altered positions of the patient during image acquisition. A review on the established methods is given, and two voxel based approaches are finally selected to be included in the tool chain. Also, MR image series often represent identical materials at different intensities even when acquired by using the same protocols, e.g. due to the imperfection in the scanner hardware. Therefore, a variety of approaches was investigated to automatically adjust the intensity of pairs of MR images of the head. It is shown that the optimization of statistical measures is useful to improve the material-intensity consistence.

With the preprocessing steps given above, the images of a time series are adjusted for position, orientation, and intensity distribution. Hence, the residual differences between the images are assumed to be induced by the disease/treatment process only. Non-rigid registration based on fluid dynamics is employed to quantify these differences. Since fluid dynamics based registration is known to be computational intensive, approaches are tested speed up registration. As a result of this work, it is shown that a variant of the Gauss-Southwell-relaxation is best suited to solve the registration problem with a sufficient accuracy on a workstation class computer.

With non-rigid registration, the differences between the images of a time series are given as large scale vector fields that are difficult to interpret. Therefore, I propose contraction mapping to detect critical points (e.g., attractors and repellors) in order find deformation spots in the time series images. The accuracy of this method is demonstrated by its application to synthetically generated vector fields.

As the last analysis step, a visualization based on surfaces extracted from the anatomical image data, overlaid with the deformation fields, and in conjunction with possible critical points is used, to illustrate the monitored anatomical change.

This tool chain was applied to pathological MRT data, such as data acquired during the progression of Alzheimer's disease or during the post-acute phase following an intra-cerebral hemorrhage. It is illustrated how a better understanding of the disease process may be achieved.

Another example, CT examinations during midfacial distraction osteogenesis demonstrate the usefulness of a proper 3D analysis of a treatment process. These examples demonstrate that this tool chain even captures minute changes in time series data that are easily overlooked. In addition, it allows the quantification and qualification of structural changes on a high level description.

Acknowledgment

Foremost, my gratitude goes to my supervisor Dr. Fritjhof Kruggel. He was always there for discussion and when I was searching for advice, he guided me with gentle hands and he always left room for my own ideas. Without him, this thesis would never have happened.

Many thanks go to Dr. Marc Tittgemeyer. He helped me to understand the elasticity theory, which I was oblivious to, before I started my PhD. It was a pleasure to work with him, and I'm looking forward to be colleagues with him for some more time.

My appreciation goes to Dr. Dr. Thomas Hierl from the Department of Oral and Maxillofacial Plastic Surgery at the University of Leipzig. For his request, I started to use my tools for the analysis of the midfacial distraction osteogenesis, which proved to be a very interesting application. Further, I wish to thank Prof. Dr. R. Klöppel from the Department of Diagnostic Radiology of Leipzig University, for providing the necessary CT data sets.

My thanks goes to the working group, especially to Claire, Vassili, and Markus; I really appreciated our time together, and especially our lunch breaks that helped me to improve my spoken English. I'm grateful to my colleagues who keep the wheels turning in the background; above all I wish to thank Nicole Pöschel, our secretary, and Gerline Lewin, our librarian. Also, I very much appreciated Constanze's help to get the language of this thesis straight.

After having acknowledged my dissertation supervisor and colleagues, I wish to thank the creators of free software. My work relied on your creations, and therefore, most of the tools discussed in this thesis, i.e. all the software that I can claim copyright on, are made freely available under the terms of the GNU public license agreement [119].

Of course no such work can be achieved without a place for the mind to relax. Therefore, I wish to thank all my friends, especially for all the wonderful hours I spend with you; I hope we will share a lot more time with each other.

Finally, my thanks go to my parents, my sister and my brother, to whom I dedicate this work.

To my parents, Peter and Karin Wollny,
to my sister and my brother.

Symbols and Abbreviations

Notation	*Description*
$\mathbb{N}$	set of natural numbers
$\mathbb{Z}$	set of integral numbers
$\mathbb{R}$	set of real numbers
$\mathbf{u}, vv, \mathbf{x}$	vectors and vector fields
α, β, γ	Eulerian angles
$A \subseteq B$, $(A \subset B)$	A is a (true) subset of B
$A \cap B$	intersection of sets A and B
$\wedge$	logical *and*
$\Leftrightarrow$	if and only if
$[a,b]$, $]a,b]$, $[a,b[$, $]a,b[$	closed, left half open, right half open, open interval from a to b
$f : A \rightarrow B$	f is a mapping from A to B
$\forall$	for all ...
Ω	continuous image domain
$\widehat{\Omega}$	discretized image domain
Ψ	intensity range
$I : \Omega \rightarrow \Psi$	image I with coordinate domain Ω and intensity range Ψ
$S : \Omega \rightarrow \Psi$, $(R : \Omega \rightarrow \Psi)$	study (reference) image
$\mathbb{I}_{\Omega,\Psi}$, $\mathbb{I}$	image space
$\mathbb{T}$	coordinate transformation space
$P(I(\mathbf{x}) = u)$	probability that intensity of image I at location $\mathbf{x}$ equals u
$H(I)$	histogram of image I
$\hat{H}^{w}(I)$	histogram of image I filtered with a Gaussian kernel of width w
$E(I)$ $\left(D^2(I)\right)$	mean (dispersion) of intensities of image I
$\eta(I)$	entropy of image I
$J(T)\vert_{\mathbf{x}_0}$	Jacobian of transformation T at $\mathbf{x}_0$
$A_{\mathrm{reg}}(R,S,T)$, A_{reg}	registration accuracy when registering study image S to reference image R by using transformation T
$\mathfrak{L}$	Navier-Stokes-operator
μ, λ	Lamé's elasticy constants μ (shear) and λ (dilatation)
AD	Alzheimer's Disease

Notation	*Description*
CC	cross corelation
CSF	cerebrospinal fluid
CT	computer tomography
MR(T)	magnetic resonance (tomography)
MINRES	minimum residual algorithm
(N)MI	(normalized) mutual information
RED	rigid external distraction
SOR(A)	succesive over-relaxation (with adaptive update)
SSD	sum of squared differences

Contents

Abstract 1

Acknowledgment 3

Symbols and Abbreviations 5

1 Introduction 3
- 1.1 Focus of this work . . . 3
- 1.2 Motivation . . . 4
- 1.3 A Review of Time Series Medical Image Analysis . . . 6
- 1.4 Outline . . . 7

2 Basic Concepts 9
- 2.1 Notation . . . 9
- 2.2 Images and Transformations . . . 9
- 2.3 Registration . . . 11
- 2.4 Image Acquisition . . . 12
- 2.5 Similarity Measures and Corresponding Cost Functions . . . 15
- 2.6 Discretization of the Image Domain . . . 16

3 Pre-Processing 17
- 3.1 Position Correction by Rigid Registration . . . 17
- 3.2 Normalization of the Image Intensity Range . . . 18
- 3.3 Approaches to Intensity Adjustment . . . 19
- 3.4 Experiments . . . 21
- 3.5 Results and Discussion . . . 22
- 3.6 Conclusion . . . 24

4 Quantification of Deformation 25
- 4.1 Approaches to Non-Rigid Registration . . . 25
- 4.2 The Non-Rigid Registration Based on a Fluid Dynamical Model . . . 28
- 4.3 Solving the Linear PDE of Fluid Dynamics . . . 29
- 4.4 Experiments and Results . . . 33
- 4.5 Conclusion . . . 38

5 Describing Vector Fields by Means of Critical Points 39
5.1 Motivation 39
5.2 The Concept of Critical Points 40
5.3 Metric Space and Fix Points 41
5.4 Estimation Algorithm 43
5.5 Conclusion 45

6 Visualization 47
6.1 A Brief Note About the Implementation 47
6.2 Preparing Anatomical Data for Visualization 47
6.3 Critical Points 48
6.4 The Vector Field 49

7 Application 51
7.1 Analyzing MR Time Series Data 51
7.2 Analysis of CT Time Series Data 60

8 Discussion 65
8.1 Achievements and Limitations 65
8.2 Outlook 68

A Mathematics 71
A.1 Derivation of Euler Step 71
A.2 Discretization of the Navier-Stokes Equation 71
A.3 SOR Update 72
A.4 Convolution Filter 73

B Algorithms 75

Bibliography 78

Chapter 1

Introduction

In this chapter it is outlined, why the automatic analysis of time series medical images is an interesting and important research area. Relevant literature on the topic is reviewed, and at the end of the chapter it is outlined how this thesis is organized.

1.1 Focus of this work

This thesis focuses on the quantification and qualification of changes in time series of medical images of the head. Quantification of changes in such series is performed by a matching procedure, the *registration*. Based on measures that describe the similarity of images, so-called *cost functions*, a displacement field (*transformation*) is calculated which maps corresponding structures from one image (the *study image*) to another (the *reference image*). Interesting regions of change are then segmented from this transformation. Finally, a concise visualization helps to understand the nature and pattern of change.

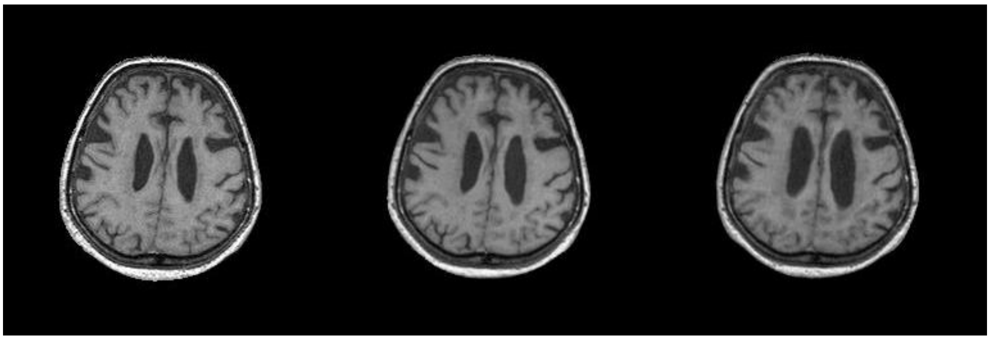

Figure 1.1: Example slices from a MR volume dataset of a patient with diagnosed Alzheimer's Disease. The left image was taken first, the middle one twelve month later, and the right one 32 month after the first. Visual inspection, which is still the gold standard in clinical neuroscience, allows for a qualitative description of the disease progression only.

Time series of medical images may be acquired by monitoring disease processes or treatment. With the application of *magnetic resonance tomography* (MRT) or *computer tomography* (CT), images are obtained as 3D matrices of gray scale values. Relevant differences between these images are induced by the monitored disease / treatment process. The assessment and interpretation of these differences is the main focus of this thesis. In addition, also methods are described that eliminate differences between time series images introduced by the imaging process only.

1.2 Motivation

Monitoring Disease Progression

As a first impression of time series of medical images, consider the development of a patient with the clinical diagnosis of Alzheimer's Disease (AD). The most prominent clinical feature of AD is the progressive memory impairment. While the recall of information stored in long term memory is preserved until advanced stages of the disorder, especially the ability to learn new information decreases. For research and clinical purposes, clinical criteria have been developed to distinguish probable, possible, and definite AD, based on deficits in cognition and memory, the onset age, and the presence of a dementia syndrome (McKahn et al. [78]). However, the accuracy of these criteria is limited (cf. Varma et al. [114]).

Neuro-imaging is the most widely used ancillary test to support the clinical diagnosis. However, its value in clinical practice is still not very well known. Images given in Fig.1.1 have been acquired during a 32 month interval. As a consequence of disease progression, an enlargement of the ventricles can be seen. However, visual inspection allows a qualitative description only. Analyzing shape changes quantitatively has the potential to reveal a disease pattern that may support an early diagnosis.

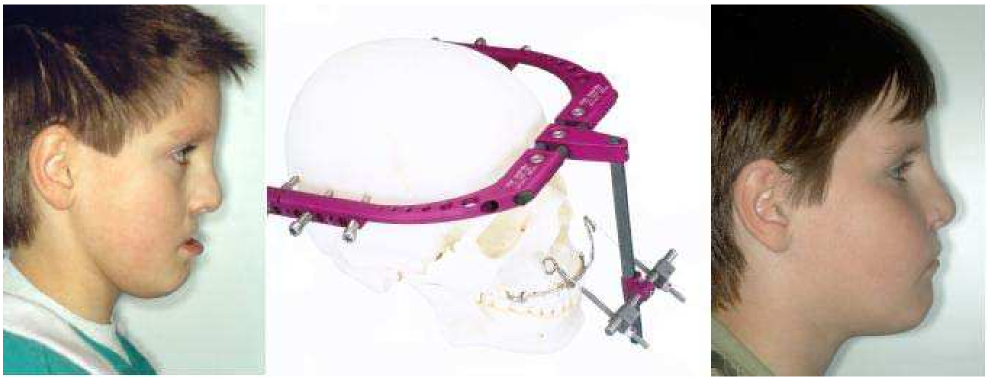

Figure 1.2: From left to right: A twelve year old boy suffering from a bilateral cleft lip and palate, pre-operative status; the RED system applied to a model skull; post-operative status. Esthetic improvements are obvious, but the analysis of the bony changes was impossible so far.

Evaluating Medical Treatment

As another example of time series medical images the monitoring of active treatment may hold forth. Consider the sutural midfacial distraction osteogenesis with simultaneous rapid maxillary expansion by using a *rigid external distraction* (RED) system, to correct a bilateral cleft lip and palate (Fig. 1.2).

Using a RED system for midfacial distraction osteogenesis is a method to correct the underdevelopment of the midface, surpassing traditional orthognathic surgical approaches for these patients (Hierl and Hemprich [56], Polley and Figueroa [87, 88]). In complex malformations, surgery planning is based on CT images followed by a modified midfacial osteotomy. Finally the midface is slowly advanced by a halo-borne distraction device until a correction of the midfacial deficiency is achieved.

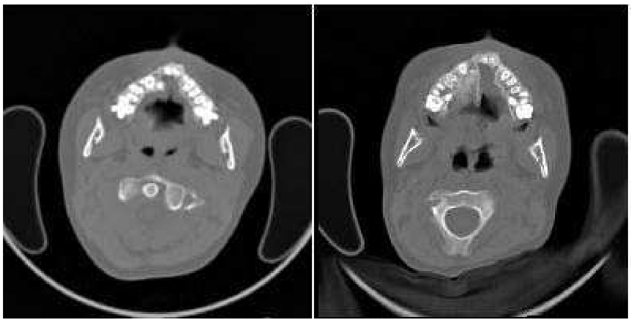

Figure 1.3: Pre- (left) and postoperative CT scans of a person treated with the RED-System (see also Fig. 1.2).

Although striking esthetic improvements are obvious, the analysis of the three-dimensional bony changes of the skull was impossible so far. A thorough analysis of these changes, however, is necessary to get a better understanding of the effects of the distractor onto the whole skull, and thus, to improve therapy planning. This is of eminent importance for the new field of sutural distraction, in which the midface is displaced without or with only limited osteotomies (Hierl et al. [57]). Furthermore, bio-mechanical considerations on midfacial advancement dynamics, e.g., the determination of the point of force application by using the RED-system and its relation to the center of rotation, are important to get an understanding of the final treatment outcome and to improve treatment planning. Routinely acquired pre- and postoperative CT scans are used to monitor these changes (Fig. 1.3), but again, a manual quantification of changes seems not feasible.

In both examples, an analysis of structural changes with time may increase knowledge about the underlying disease or treatment process. Disease patterns may be revealed, and the impact of medical treatment can be measured. Also, a better understanding of a disease or a treatment can help to improve computational models of head and brain. These models, finally, can be used to enhance treatment planning in general and enhance navigation systems for (neuro-)surgery in particular.

1.3 A Review of Time Series Medical Image Analysis

The manual analysis of medical images is dependent on the expertise and objectiveness of the observer. Lemieux at el. [67] described methodologies for manual volumetric measurements of the hippocampus and the cerebellum in MRT data. They noted that it was necessary to blind the operator to the chronological order of the data sets and the nature of the subject (patient or normal control) to avoid human prejudice.

But with the emergence of better tools for image registration (see chapter 3 and chapter 4), methods were developed to analyze images automatically.

Usually, the first step in an automatic analysis of serial medical images includes rigid registration, to eliminate positional differences of the patients during image acquisition. Rigid registration restricts the transformations applied to the images to rotation and translation. Consequently, these transformations are not able to deal with local variations between the images, but only with global ones.

Based on rigid registration, Lemieux et al. [68] introduced a method to detect and assess changes in lesions, which can be found in image data of epilepsy patients. Intra-subject pairs of serially acquired MR images, rigidly registered, were used to calculate difference images. The difference images were normalized into Talairach space (Talairach and Tournoux [103]). By using only images of normal controls, a structured map was created to represent the noise, generally present in MR images. By comparing a patient's difference images with this structured noise map, changes in the time series image could be detected, even in image areas which originally were reported as "unchanged" after visual inspection. Nevertheless, this method is strongly dependent on the accuracy of the initial rigid registration.

Another method to analyze time series medical images by rigid registration was presented by Fox et al. [40]. The brain was segmented in rigidly registered image pairs of AD patients that were acquired with a 12-month interval. The change in cerebral volume was computed directly from the image sets by using an interactive tool [43]. Fox et al. [40] reported that their method offers the ability to measure the rate of atrophy, and thus, to measure a drug effect in patients.

Non-rigid registration adds local variability to the registration process. Therefore, the structural change over time, monitored by medical imaging (e.g., MRT or CT), can be quantified by a non-rigid transformation. This transformation can then undergo further analysis.

One approach to analyze a transformation is the evaluation of its Jacobian. The Jacobian [15] can be seen as a measure for the volume variation introduced by a transformation T at a certain point $\mathbf{x}$. It is given as

$$J(T)|_{\mathbf{x}} = \det(\nabla T|_{\mathbf{x}}), \tag{1.1}$$

(for a discussion see section 2.2). If $J(T)|_{\mathbf{x}} > 1$, the displacement field describes growth, and if $1 > J(T)|_{\mathbf{x}} > 0$, it describes shrinkage in the vicinity of point $\mathbf{x}$; for topology preservation $J > 0$ has to be ensured during non-rigid registration.

Based on this property of the Jacobian, Rey et al. [91] proposed a method to detect and quantify evolving lesions in time series images of *Multiple Sclerosis* (MS) patients. The images, acquired by monitoring disease progression, were registered non-rigidly, yielding a transformation that describes the disease progression. By calculating an image whose intensity values correspond to the Jacobian of this transformation and by thresholding the image, Rey et al. [91] were able to segment shrinking and growing regions. Compared with Lemieux et al. [68], their method is robust with respect to misalignment during rigid registration, since errors in rigid registration are compensated when the Jacobian is evaluated.

Chung et al. [27] extended this approach by creating probability maps of shape change. With their application to time series MR images of children, they demonstrated how this method can be used to detect growth patterns of the brain.

Another approach to analyze time series images for growth pattern was introduced by Thompson et al. [108]. The developing brain of children (aged 3-15 years) was monitored with MR examinations. Later, the non-rigid transformation describing the structural change in the course of time was analyzed by evaluating continuum mechanical tensor maps [49, 109, 110]. Amongst other things, Thompson et al. [108] identified that the fiber system, which mediates language function and associative thinking, grew more rapidly in the time before and during adolescence, with growth attenuated shortly afterwards – a pattern that coincides with the ending of a well-known critical period for learning language (Grimshaw et al. [50]).

In summary, the analysis of time series medical images is an active research area. Its aims are the analysis of the individual development of the brain during growth and disease, the measurement of treatment impact, as much as the detection of growth and disease patterns by statistical means.

1.4 Outline

Throughout this work, a tool chain for the analysis and the interpretation of time series of 3D medical images will be outlined and developed. Furthermore, this tool chain will be applied to sample data in order to analyze its applicability.

In chapter 2, the mathematical foundation is outlined by introducing basic concepts, such as *images*, *transformation*, *registration*, *voxel similarity*, *cost functions*, and *multi-resolution image processing*. Chapter 3 discusses differences between time series images that result from different imaging conditions only. Approaches to rigid registration, used to eliminate differences in head positions, are addressed, and a method for automatic intensity adaption of intra-modal images is proposed and tested. In chapter 4, an overview of non-rigid registration is given and non-rigid registration based on a fluid dynamic model will be discussed in detail. Approaches for performance optimization of this computational intensive algorithm are studied. Chapter 5 is dedicated to the qualitative analysis of non-rigid transformations. The concept of *critical points* is illustrated, a novel method for detection of critical points on a discrete lattice is proposed and tested. Afterwards, a short insight into visualization techniques is given in chapter 6. Chapter 7 shows applications of the tool chain, and finally, a critical review concludes this thesis as chapter 8.

Chapter 2

Basic Concepts

This chapter focuses on the definition of images, transformations, and statistical measures. Further, the main concepts of registration, similarity measures and cost functions will be illustrated. Finally, the discretization of an image domain and an approach to multi-resolution image processing is introduced.

2.1 Notation

In the following $\mathbb{N}$ denotes the set of natural numbers; vectors and vector fields are denoted by lower case letters in bold font such as $\mathbf{u}, \mathbf{v}, \mathbf{x}$ and upper case letters in bold font represent matrices ($\mathbf{A}, \mathbf{P}$). If not otherwise indicated, all scalars, constants, vectors elements, and matrix elements considered here are real, i.e. are taken from the set of real numbers $\mathbb{R}$. The Landau symbols [15] $o(\ldots)$ and $O(\ldots)$ are used in the following manner: $f(x) = o(g(x))$ if $\frac{f(x)}{g(x)} \to 0$ for $x \to 0$, and $f(x) = O(g(x))$ if $\left|\frac{f(x)}{g(x)}\right| \leq C$ for $x \to \infty, C = \text{const}$. Other symbols will be introduced when applicable.

2.2 Images and Transformations

Definition 2.1. *With* $\Omega \subseteq \mathbb{R}^3$ *and* $\Psi \subseteq \mathbb{R}$ *an image* I *is defined as a mapping* $I : \Omega \to \Psi$. Ω *is called the* image domain*, and* Ψ *its* intensity range*.* $I(\mathbf{x})$ *denotes the intensity of image* I *at coordinate* $\mathbf{x} \in \Omega$*. The set of all images* $\{I : \Omega \to \Psi\}$ *is called the* image space $\mathbb{I}$.

If not otherwise indicated, $\Omega = [0,1]^3 \subset \mathbb{R}^3$, and since this thesis focuses on gray scale images only, $\Psi = \{0, 1, \ldots, 255\}$. The *study image* will be denoted as $S : \Omega \to \Psi$, and the *reference image* as $R : \Omega \to \Psi$. The ordered pair $(\mathbf{x}, I(\mathbf{x}))$, consisting of a coordinate $\mathbf{x} \in \Omega$ and the corresponding image intensity $I(\mathbf{x})$, is referred to as a volume element (*voxel*).

Two types of mappings change a voxel: an intensity mapping $M : \Psi \to \Psi$, acting on the intensity values $I(x)$, and a spatial mapping $T : \Omega \to \Omega$, acting on the coordinates $\mathbf{x}$. This yields the following definitions:

Definition 2.2. *A mapping* $M : \Psi \to \Psi$ *of the image intensity range onto itself is called an* intensity adjustment*.*

Definition 2.3. *A mapping* $T : \Omega \rightarrow \Omega$ *of the image domain onto itself is called a* transformation, *the set of all such transformations* $T : \Omega \rightarrow \Omega$ *is called the transformation space* $\mathbb{T}$. $T_0(\mathbf{x}) := \mathbf{x} \forall \mathbf{x} \in \Omega$ *is called the* identity transformation. *An image can be deformed by means of a transformation T like* $I(\mathbf{x}) \rightarrow I(T(\mathbf{x})) \forall \mathbf{x} \in \Omega$. *The transformed image* $S(T(\mathbf{x}))$ *will also be denoted as* S_T.

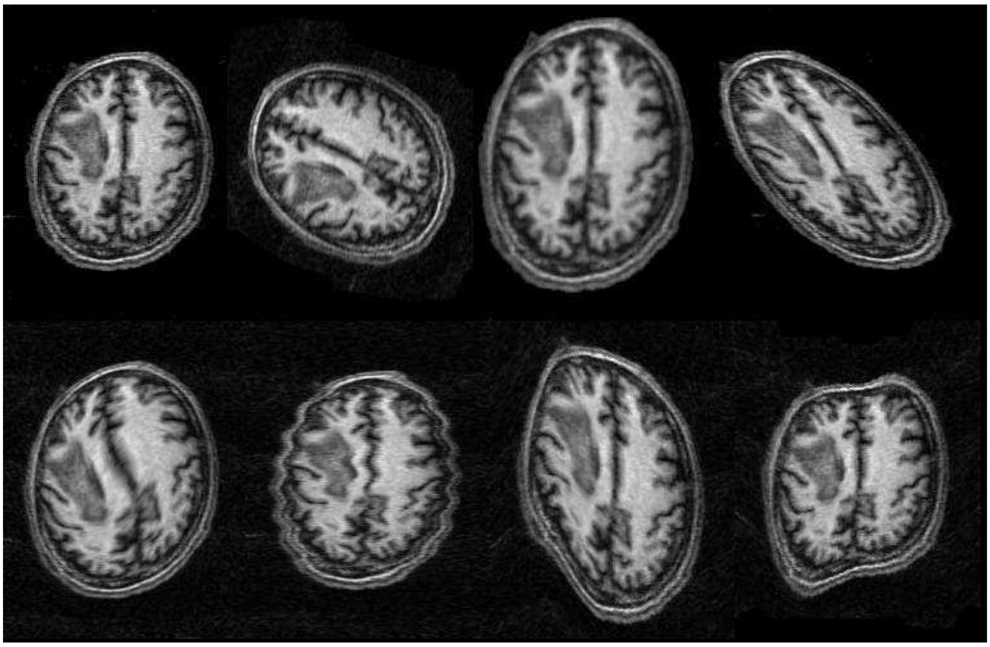

Figure 2.1: Examples of affine-linear transformations (first row): original image, rotation, scaling, shear, and examples of non-linear transformations (second row).

In general, linear and non-linear transformations can be distinguished (Fig. 2.1). With non-linear transformations, the transformation space $\mathbb{T}$ is not restricted per se. With a linear transformation T, on the other hand, the transformation space $\mathbb{T}$ is restricted to the affine-linear mapping

$$T(\mathbf{x}) := \mathbf{A}\mathbf{x} + \mathbf{b}, \mathbf{A} \in \mathbb{R}^{3\times 3}, \mathbf{x}, \mathbf{b} \in \mathbb{R}^3. \tag{2.1}$$

For transformation T, this yields 12 degrees of freedom: nine for rotation, scaling, and shear (matrix $\mathbf{A}$) and three for translation (vector $\mathbf{b}$). When the transformation is further restricted to six degrees of freedom, i.e. to rotation and translation only, the transformation is called *rigid*.

Since the transformations considered here describe spatial displacements of voxels, they are best described in the so-called *Eulerian reference frame* where the voxels are tracked by their position: A voxel originates at time $t_0 = 0$ at coordinate $\mathbf{x} \in \Omega$. As it moves through Ω, its displacement at time $t \in \mathbb{R}$ is given as a vector $\mathbf{u}(\mathbf{x}, t) \in \mathbb{R}^3$. The set of the displacements of all voxels of an image is called a displacement field over domain Ω, and its value at time t

is denoted as $\mathbf{u}(t)$. The corresponding transformation T can be given coordinate-wise:

$$T(\mathbf{x},t) := \mathbf{x} - \mathbf{u}(\mathbf{x},t) \, \forall \mathbf{x} \in \Omega. \tag{2.2}$$

The concatenation of two transformations T_1 and T_2 with the displacement fields $\mathbf{u}_1$ and $\mathbf{u}_2$, respectively, can then be given:

$$(T_1 \oplus T_2)(\mathbf{x}) = \mathbf{x} - \mathbf{u}_1(\mathbf{x} - \mathbf{u}_2(\mathbf{x})) - \mathbf{u}_2(\mathbf{x}) \, \forall \mathbf{x} \in \Omega. \tag{2.3}$$

Note, the concatenation of transformations is not commutative, i.e. in general $(T_1 \oplus T_2) \neq (T_2 \oplus T_1)$.

The Jacobian Operator

Definition 2.4. *The Jacobian of a mapping* $T : \mathbb{R}^3 \to \mathbb{R}^3$ *at coordinate* $\mathbf{x} \in \mathbb{R}^3$ *is defined by [15]*

$$J(T)|_{\mathbf{x}} := \det(\nabla T|_{\mathbf{x}}). \tag{2.4}$$

Since the transformation T is described by means of a displacement field $\mathbf{u}$: $T(\mathbf{x}) := \mathbf{x} - \mathbf{u}(\mathbf{x})$; the Jacobian can also be written as

$$J(T)|_{\mathbf{x}} = \det(\mathbf{I} - \nabla \mathbf{u}|_{\mathbf{x}}). \tag{2.5}$$

Consider now the dilatation $\delta\mathbf{x}'$ of a line defined by a pair of points $(\mathbf{x}, \mathbf{x} + \delta\mathbf{x})$:

$$\delta\mathbf{x}' = \delta\mathbf{x} + \mathbf{x} - \mathbf{u}(\mathbf{x} + \delta\mathbf{x}) - (\mathbf{x} - \mathbf{u}(\mathbf{x})) = \delta\mathbf{x} - \nabla\mathbf{u}(\mathbf{x}) \cdot \delta\mathbf{x}. + O(\|\delta\mathbf{x}\|^2) \tag{2.6}$$

and in a first order approximation

$$\delta\mathbf{x}' = (\mathbf{I} - \nabla\mathbf{u})|_{\mathbf{x}} \cdot \delta\mathbf{x}. \tag{2.7}$$

Thus the local volume dilatation $\delta V'$ around point $\mathbf{x}$ is given by

$$\delta V' = J(T)|_{\mathbf{x}} \cdot \delta V, \tag{2.8}$$

and the transformation $\frac{\delta V'}{\delta V}$ of a small volume is classified by the Jacobian of the deformation mapping T. If $J(T)|_{\mathbf{x}} > 1$ then the transformation describes a local expansion at point $\mathbf{x}$, and if $0 < J(T)|_{\mathbf{x}} < 1$ it describes local shrinking. For the problem domain considered here, transformations have to preserve topology. Therefore, the case $J(T)|_{\mathbf{x}} \leq 0$ does not apply.

2.3 Registration

Registration aims at transforming a study image S with respect to a reference image R, so that structures at the same coordinates in both images finally represent the same object. In practice, this is achieved by finding a transformation $T_{\text{reg}} \in \mathbb{T}$ which minimizes a cost function $F_{\text{cost}} : \mathbb{I} \times \mathbb{I} \to \mathbb{R}$, while constraining the transformation through the joint minimization of an energy term $E(T)$:

$$T_{\text{reg}} := \arg\min_{T \in \mathbb{T}} \left(F_{\text{cost}}(S_T, R) + \kappa E(T)\right). \tag{2.9}$$

The cost function F_{cost} accounts for the mapping of similar structures. $E(T)$ ensures topology preservation, which is necessary to maintain structural integrity in the study image, and it thus introduces a smoothness constraint on the transformation T. The parameter κ is a weighting factor that balances registration accuracy and transformation smoothness.

Similar to the classification of transformations, a registration can be classified as *rigid*, *affine*, or *non-rigid*, corresponding to the transformation applied. Approaches to rigid registration will be addressed in chapter 3; chapter 4 will discuss non-rigid registration.

The registration, as described above, requires a cost function that has its (global) minimum when the images match best

$$F_{\text{cost}}(S,R) \rightarrow \min \Leftrightarrow (S \rightarrow R). \tag{2.10}$$

Cost functions can rely on image features (edges, extremal points, crest lines) or on voxel intensities. The registration approaches used here are voxel based. Therefore, measures have to be introduced that describe image similarity based on intensity values. In order to discuss such measures, it is necessary to review the imaging process, since it provides the connection between the material and its representation in the images.

2.4 Image Acquisition

Medical volume images can be acquired by using a variety of imaging technologies and imaging protocols. The images considered in this work were acquired by using *computer tomography* (CT) or *magnetic resonance tomography* (MRT). With these methods, each voxel of the image corresponds to a cubical sub volume of the imaged object.

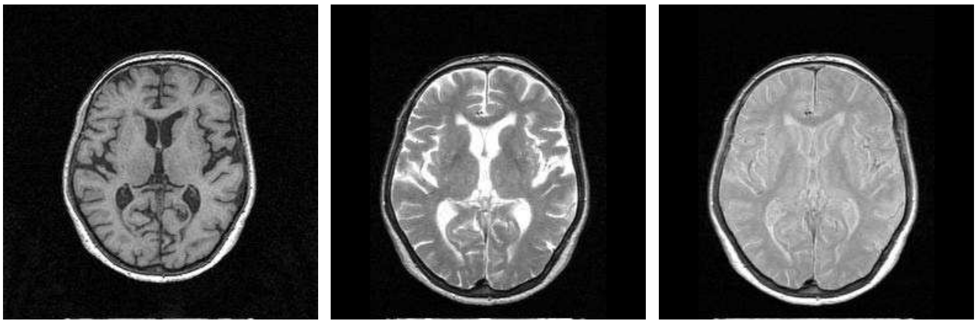

(a) T1-weighted (b) T2-weighted (c) Proton-Density-weighted

Figure 2.2: Examples of an axial head slice acquired by using different MRT protocols. The MR images considered here will all be T1-weighted.

Because CT is based on x-ray, for each image voxel the absorption in the corresponding sub volume is measured. The absorption corresponds to the average atom mass of the sub volume's materials. A mapping from absorption to voxel intensity is realized by the so-called Hounsfield-scale (Kak and Slaney [63]) that normalizes the absorption values to the reference material *water*. Therefore, the material-intensity mapping in CT images is similar to the mapping in traditional x-ray images: materials with a low atom mass are represented by low intensities and materials with a high atom mass are represented by high intensities. Moreover, the Hounsfield scale provides a normalized material-intensity mapping and, hence, a normalized intensity range for all CT images. As it is with traditional x-ray-images, in CT images different types of soft tissue can hardly be distinguished.

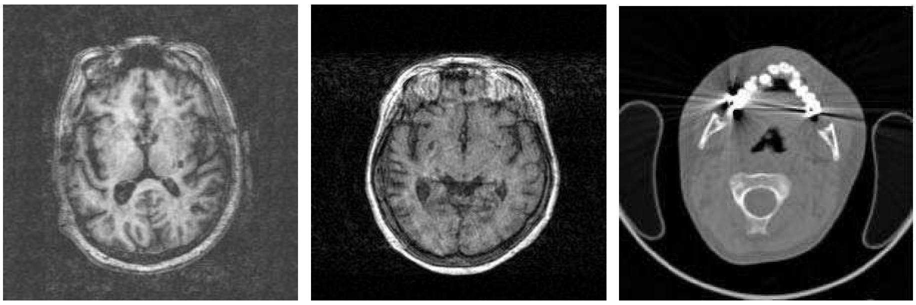

(a) noise (MR) (b) motion artifact (MR) (c) streak artifacts (CT)

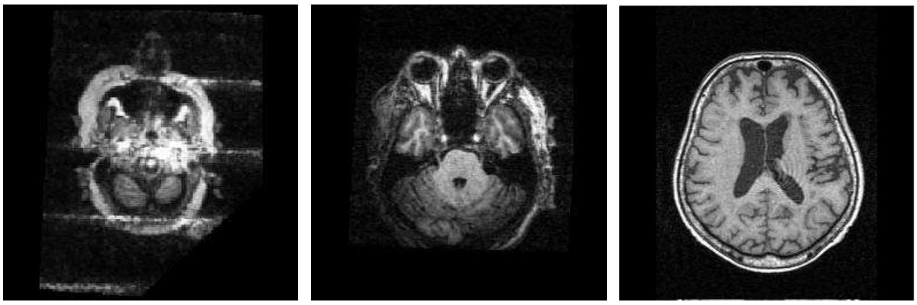

(d) susceptibility artifact (MR) (e) B^1-field inhomogeneity (MR) (f) gibbs ringing (MR)

Figure 2.3: Examples of artifacts and noise in medical images

In MR images, the signal strength of a voxel corresponds to the hydrogen-1 density [1] and, especially, the material, e.g., white matter, gray matter, or water, the hydrogen-1 is bound to in the respective cubical sub volume. Two material constants, the so-called *T1* and *T2* constants, influence the mapping of these materials to the voxel intensity. The imaging protocols can, therefore, be adjusted to enhance different aspects of the examined objects (Fig. 2.2). Hence, in MR images it is possible, to distinguish between different types of soft tissue. If MR images are acquired by using the same device and the same protocol, the assumption of a normalized intensity range also may hold to a certain amount. However, because of the wide variety of parameters that influences the mapping of hydrogen density to intensity, and also because of the imperfection of the scanner hardware that yields varying intensity-material mappings, often no intensity range normalization can be given for MR images. For a thorough discussion of MR imaging the reader is referred to the literature, e.g., Brown and Semelka [16], Chen and Hoult [21], Markisz and Whalen [76].

---

[1] Although various nuclei are of biological interest [76], the images used in this work are all imaging the single unpaired proton of hydrogen-1.

Furthermore, the image quality of MR images and CT images, and hence, the material-intensity mapping, in general, is also influenced by a variety of additional factors. Noise affects images; CT usually has a high signal to noise ratio, therefore, the influence of the Gaussian noise present in these images can be neglected. However, MRT often has a low signal to noise ratio (Fig. 2.3 (a)), hence, it has to be considered whether steps are taken to reduce the influence of the Rayleigh noise post-hoc. Smoothing the images with edge preserving filters may be applied, but it may also remove information about a certain structural change. There is bound to be a trade-off between noise reduction and information loss; here the case has to decide importance. By exploring a focal lesion, for instance, noise reduction might be appropriated, while the analysis of diffuse lesions may better rely on structural information, which would be lost if the image data is filtered.

One may also distinguish several imaging artifacts, e.g.:

- Patient related artifact
  - *Motion artifacts* (Fig. 2.3 (b)) resulting from an uncontrolled movement of the subject during image acquisition. A proper fixating of the subject can be used to suppress it.
  - Metallic implants like dental fillings and orthodontic devices may cause *streak artifact* in CT images (Fig. 2.3 (c)). With a sufficient knowledge about the image acquisition process, the artifact may be removed from the images [52, 117].
  - In MR images the high susceptibility of metallic implants yield a distortion of the magnetic field and, hence, a distorted image (Fig. 2.3 (d)).
- System caused artifacts
  - The imperfection of the imaging devices, e.g. the B^1*-field inhomogeneities* in MRT, yields intensity inhomogeneities in images (Fig. 2.3 (e)). Besides a better coil setup to reduce the artifact beforehand, the adaptive fuzzy c-means method [85] can be used to correct the inhomogeneities post-hoc.
  - The image reconstruction may yield errors, e.g. *Gibbs ringing* (Fig. 2.3 (f)) in MR images.

More examples could be given, but are out of the scope of this work. For a further discussion of artifact and post-hoc image enhancement, the reader is referred to, e.g., Ahmed et al. [2], Archibald and Gelb [3], Haacke et al. [52], Kak and Slaney [63], Markisz and Whalen [76], Pham and Prince [85], and Wang et al. [117].

The focus is now turned to the definition of cost functions needed for image registration.

2.5 Similarity Measures and Corresponding Cost Functions

If it can be assumed that materials are represented by the same intensities in all images, like it is the case in normalized CT images, the *identity relationship* can be used to describe the material-intensity mapping. With this relationship, two voxels are similar, if their intensity values are similar. Therefore, a study image S is similar to a reference image R, $S \to R$, if for each voxel the intensity values are similar, $S(\mathbf{x}) \to R(\mathbf{x}) \forall \mathbf{x} \in \Omega$. Moreover, two images match *exactly*, if the intensity values of all corresponding voxels match:

$$S = R \Longleftrightarrow S(\mathbf{x}) = R(\mathbf{x}) \forall \mathbf{x} \in \Omega. \tag{2.11}$$

This yields the *sum of squared differences* (SSD) as a cost function, describing similarity of two images S and R:

$$F_{\mathrm{SSD}}(S,R) := \int_{\Omega} (S(\mathbf{x}) - R(\mathbf{x}))^2 . \tag{2.12}$$

In case no normalization of the intensity range between images is possible, other measures have to be found, to describe the similarity of voxels. Several authors proposed mutual information (MI) as similarity measure [28, 73, 115]:

Definition 2.5. *Given $P(I(\mathbf{x}))$, the probability that the voxel $(\mathbf{x}, I(\mathbf{x}))$ has a certain intensity, and given the entropy $\eta(I)$ of the image I*

$$\eta(I) := \sum_{\mathbf{x} \in \Psi} P(I(\mathbf{x})) \log_2 P(I(\mathbf{x})). \tag{2.13}$$

Then mutual information *(MI) between an image R and an image S is given as*

$$MI(R,S) := \eta(R) + \eta(S) - \eta(R,S). \tag{2.14}$$

with $\eta(R)$ and $\eta(S)$ denoting the entropy of the image R and S respectively, and $\eta(R,S)$ referring to the entropy of the cross-correlate $R \times S$.

Another interpretation of MI can be given as follows: Consider the intensities $R(\mathbf{x})$ and $S(\mathbf{x})$, $\mathbf{x} \in \Omega$ are random quantities with corresponding probability densities $P(R(\mathbf{x}))$, $P(S(\mathbf{x}))$, and the cross-correlate $R(\mathbf{x}) \times S(\mathbf{x})$ is a random quantity with density $P(R(\mathbf{x}), S(\mathbf{x}))$. Then MI can also be written as (Viola [115])

$$\mathrm{MI}(S,R) := \sum_{\mathbf{x}} P(R(\mathbf{x}), S(\mathbf{x})) \log_2 \frac{P(R(\mathbf{x}), S(\mathbf{x}))}{P(R(\mathbf{x}))P(S(\mathbf{x}))}. \tag{2.15}$$

This can be interpreted like follows: If $R(\mathbf{x})$ and $S(\mathbf{x})$ are two independent random variables, then $P(R(\mathbf{x}), S(\mathbf{x})) = P(R(\mathbf{x}))P(S(\mathbf{x}))$. Whereas, if $R(\mathbf{x})$ and $S(\mathbf{x})$ are dependent, then $P(R(\mathbf{x}), S(\mathbf{x})) > P(R(\mathbf{x}))P(S(\mathbf{x}))$, and $\mathrm{MI}(R,S)$ increases. Thus, with increasing similarity of the images R and S the mutual information increases.

Studholme et al. [102] showed that MI is dependent on the overlap of the images considered. To circumvent this property, they proposed the *normalized mutual information* (NMI), an extension to MI:

$$\mathrm{NMI}(S,R) := \frac{\eta(R) + \eta(S)}{\eta(R,S)}. \tag{2.16}$$

Other voxel similarity measures, such as the *correlation ratio* (CR) [92] and the *cross correlation*(CC) [46], are discussed in the literature.

Contrary to the *sum of squared differences*, with these statistical measures (CC,CR, MI, NMI) a normalization of the intensity range of the images is not required. However, the evaluation of derivatives of these measures is difficult, and thus, their optimization requires the application of optimization methods that do not rely on derivatives. Such approaches, including *Powell's direction set* [34] as well as *genetic optimization* [100], require many evaluations of the optimization criterion, making their application computationally expensive, especially if the transformation search space is not restricted, as it is the case in non-rigid registration.

Therefore, a further pre-processing step, to normalize the intensity range of serial MR images acquired by using the same protocol, will be addressed in chapter 3.

2.6 Discretization of the Image Domain

So far, only images defined on a continuous domain Ω $I : \Omega \to \Psi$ have been considered. However, digital images are given on a discrete lattice, in the case of medical volume image data they are given as 3D Matrices of gray values. The continuous image domain Ω therefore has to be discretized by using a grid constant $g > 1, g \in \mathbb{N}$

$$\Omega \to \widehat{\Omega} := \left\{ \frac{1}{g-1} \begin{pmatrix} i \\ j \\ k \end{pmatrix} \middle| i, j, k = 0, 1, \ldots, g-1 \right\}. \tag{2.17}$$

Usually, the grid constant g corresponds to the (finite) resolution of the images.

Registration algorithms, as they will be discussed later, demand a lot of computational power. They yield linear systems of equations that are often too large for a direct solution. Thus, the application of iterative methods, like *successive over-relaxation* or *conjugated gradients*, are necessary. Although in most cases these methods converge, they need many iterations and frequently their application is hardly feasible.

Several authors (e.g. Unser [112], Wesseling [118]) propose a multi-resolution approach to speed up computation. Registration starts with a coarse discretization of the image domain Ω, introduced by a low grid constant g. If the registration is achieved at a certain grid level, the grid constant will be increased; and the obtained transformation is propagated to the higher resolution. The multi-resolution iteration stops, when the grid constant g matches the finite resolution of the input images.

It is shown by Heitz et al. [54] that a coarse-to-fine procedure exhibits fast convergence properties when it is applied to high-dimensional, non-linear optimization problems (with many local minima). Since registration is first achieved for coarse structures, local minima are avoided, and thus local deterministic optimization algorithms may be used to track the solution from coarse to fine scales.

Chapter 3

Pre-Processing

Differences between medical images arise for a wide variety of reasons. Some of these differences are introduced by the imaging process and not due to structural changes. To separate these effects, images must be preprocessed to remove differences in position and intensity scale. In particular, rigid registration is addressed and a new method for automatic intensity adjustment is introduced and tested in this chapter.

3.1 Position Correction by Rigid Registration

Rigid registration is the tool of choice to eliminate different positions and orientations of objects in the imaged volume. A rigid transformation is smooth per se, i.e. the topology of the objects in the images does not change. Therefore, the problem of registration (2.9) reduces to the minimization of a suitable cost function, F_{cost}, describing the similarity of images:

$$T_{\text{rr}} := \arg \min_{T \in \mathbb{T}_{\text{rigid}}} F_{\text{cost}}(S_T, R). \tag{3.1}$$

The minimization of the cost function F_{cost} takes place in the six-parameter space, describing a rigid transformation; i.e. the three Eulerian angles which describe a rotation around the three coordinate axis and a three-dimensional translation vector have to be optimized. This is a standard optimization problem that can be solved by using, e.g. *Powell's direction set* (Eberly [34]), *genetic optimization* (Goldberg [45]), or the *Marquardt-Levenberg* algorithm (Marquardt [77]).

A variety of approaches has been discussed to select an appropriate cost function. Early methods use markers that are placed on the persons during image acquisition. These markers appear as points of high contrast in the images and can easily be found and set into correspondence. Registration is achieved by finding a rigid transformation (2.1) that minimizes the distance between corresponding marker points. The drawback of this method is that the patient must carry a stereotactic frame between successive acquisitions. Moreover, it is not possible to register images which were taken without markers.

To overcome these limitations, later approaches propose to extract extremal points, so-called *landmarks* and *crest lines*, as intrinsic markers from the image data instead (Thirion [106], Guéziec et al. [51]). The precise extraction of landmarks is a requirement to use a technique like this. As far as this thesis is concerned, the imaged brain does change. Therefore, to obtain landmarks only the shape of the head should be referenced to. This delivers usable extremal points and crest lines only for the face area. Moreover, when the monitoring of distraction osteogenesis is concerned, this area is also changed. Hence, landmark based rigid registration is unstable in this application.

In order to use available image information better, structures in the images, e.g. complete organs, can be segmented and set into correspondence to obtain a rigid registration (Malandain and Rocchisani [75]). However, registration accuracy is strongly dependent on the initial segmentation step.

Recent methods of rigid registration are based on voxel intensity. Here, the cost function is derived from a voxel-similarity measure (see Section 2.5). In consequence, the driving force of the registration is calculated directly from the given image data.

Thévenaz et al. [105] used this approach and employed the sum of squared differences (SSD) (2.12) as cost function. Optimization is achieved by using a modified version of the traditional *Marquardt-Levenberg* algorithm [77]. Since a consistent material-intensity mapping between the images is mandatory for a successful registration by using SSD as cost function, differences in the intensity distributions of the images being registered might yield registration errors. Therefore, this method is only applicable to an intra-modal registration, on which this thesis focuses. In Section 2.5 other similarity measures, like *mutual information*(MI), *normalized mutual information*(NMI), *cross correlation*(CC), and the *correlation ratio*(CR), were already discussed. Holden et al. [59] investigated their applicability for rigid registration. When they tested the registration accuracy by using hand segmented clinical 3D serial MR images as much as simulated brain model data, they found that entropy based methods (MI, NMI) are most appropriate for rigid registration of serial MR images under the conditions of typical scalp deformations and small scale anatomical change.

In this work, two methods were used to achieve rigid registration of serial medical images: One implementation is based on source code provided by Thévenaz et al. [104] that was adapted to work with the image data used here. Since this method employs the sum of squared differences (2.12) as criterion, it was considered for the registration of images with equal intensity distributions, like CT images. For images with different intensity distributions (i.e. MR images), an implementation from the SimBio bio-numerical simulation environment (Kruggel and Barber [64]) was used. It utilizes normalized mutual information (2.16) as the criterion and uses *genetic optimization* (Staib and Lei [100]) for global minimization, followed by a simplex algorithm for local optimization. Both methods employ a coarse-to-fine multi-grid scheme for faster convergence and to avoid local minima.

With both methods, an acceptable registration of images of size $200 \times 256 \times 200$ was achieved in approximately 20 minutes, measured on an Intel Pentium II 450MHz.

3.2 Normalization of the Image Intensity Range

Section 2.4 demonstrated that several imaging parameters influences the intensity mapping and tissue contrast in MR image [16, 76]. Even with the same protocol, the imperfection of the scanner hardware yields varying intensity-material mappings. As a result, no unique mapping from material to intensities can be given for MR images (see e.g. Fig. 3.1).

Voxel-based non-rigid registration will be used here to analyze time series MR images.

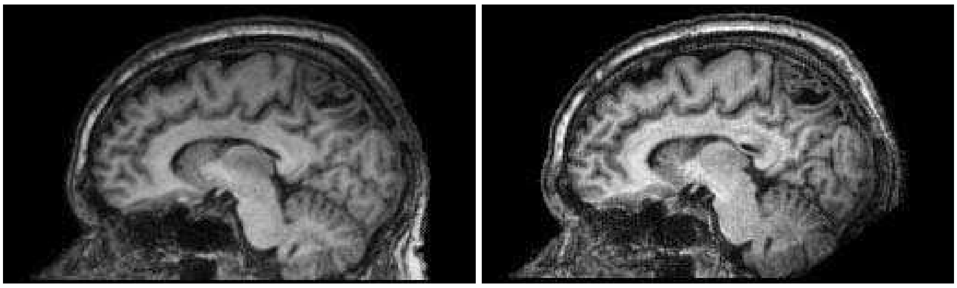

Figure 3.1: Two T1-weighted MR images of the same subject. Note the different intensity distributions and the intensity decrease in the fronto-occipital direction introduced by a B^1-field inhomogeneity (right).

During rigid registration, it is feasible to deal with varying intensity distributions, using complex voxel similarities as discussed above. Since the optimization of these measures is computationally intensive, it is hardly feasible to employ them as a criterion in non-rigid registration [4, 23].

If the images represented the same materials with similar intensities, simple voxel similarity measures, such as SSD (2.12), could be employed during the subsequent image processing in order to reduce the computation time. Therefore, several approaches have been proposed to correct the intensities in series of MR images. The methods used rely on the normalization of statistical data, such as average and standard derivation of the intensities (Chen et al. [22]), or on histogram-landmarks (Nyúl and Udupa [81]). Nylú's approach assumes a large set of MR images of the same body region. Since here, the focus is laid on pairs (and small sets) of images, this approach will not be considered.

Three criteria for automatic intensity adjustment of MR images will be investigated and their optimization with different optimization methods will be analyzed. Since it is feasible to employ complex voxel similarity measures to obtain rigid registration, it can be assumed that the images are already rigidly registered.

3.3 Approaches to Intensity Adjustment

Below, consider a study image S which will be intensity adjusted to a reference image R. To adjust a gray scale image I with values for brightness b and contrast c, the intensities of all voxels $p \in I$ are changed according to the following formula:

$$p(b,c) := \left(\left(\frac{p}{255}\right)^{2^{-b}} - 0.5\right) * 2^c + 0.5. \tag{3.2}$$

Additionally, intensity values are clamped to the intensity range Ψ. An Image I accordingly adjusted with brightness b and contrast c is then denoted as $I(b,c)$.

Even though the images are already rigidly registered, they may still differ in the scanned areas. To consider only the overlap of study image S and reference image R, with both images having intensities above a given threshold h, the processing will be restricted to the *significant domain*, as follows:

$$\Omega_h := \{\mathbf{x} | R(\mathbf{x}) > h \wedge S(\mathbf{x}) > h \wedge \mathbf{x} \in \Omega\}. \tag{3.3}$$

On this domain, the images intensities map to the *significant range*

$$\Psi_h := \{i | i > h \wedge i \in \Psi\}. \tag{3.4}$$

In the following, three cost functions are suggested and their applicability to automatic intensity adaption will be tested afterwards.

Cost Functions

If the anatomical differences between the images are small, compared to the image volume, it can be assumed that at the same location the same material is present. Thus, the intensity differences of the voxels in the significant domain Ω_h can directly be used. A *voxel cost function*, F_V, can be defined as the sum of squared differences over the significant domain Ω_h

$$F_\mathrm{V}(S,R) := \sum_{\mathbf{x}\in\Omega_h} (S(\mathbf{x}) - R(\mathbf{x}))^2. \tag{3.5}$$

Usually, noise and image artifacts yield a varying representation of material over the image domain (see, e.g., the B^1-field inhomogeneity artifact in Fig. 3.1 (right), cf. [16]). In time series MR images, anatomical changes have to be considered as well. This is a contradiction to the presumption taken for the voxel cost function. Hence, other cost functions might be more appropriate.

Definition 3.1. *With $p_i := P(I(\mathbf{x}) = i)$ denoting the probability that the voxel of image I at coordinate $\mathbf{x}$ has an intensity i, the histogram of an image I is defined as*

$$H(I) := \{p_i | i \in \Psi_h\}. \tag{3.6}$$

A distance between the histograms of study and reference image S and R with respect to threshold h can be defined as

$$d_h(H(S), H(R)) := \sum_{i\in\Psi_h} (p_i(S) - p_i(R))^2. \tag{3.7}$$

For the Rayleigh noise present in MR images and for the *partial volume effect*[1], one material is usually represented by not only one intensity but by a small intensity range. Optimizing (3.7) to adjust intensities, does not honor this. Therefore, an additional smoothing of the intensity histograms with a one-dimensional Gaussian kernel of width w is applied. Then, the *histogram cost function* F_H can be given as

$$F_\mathrm{H}(S,R) := d_h(H^w(S), H^w(R)). \tag{3.8}$$

Finally, statistical measures can be optimized (Chen et al. [22]):

---

[1] For the limited resolution of the images, a voxel might represent more then just one material.

Definition 3.2. *The mean $E(I)$ of the intensities of an image* I *is defined as*

$$E(I) := \frac{1}{size(\Omega)} \sum_{\Omega} I(\mathbf{x}). \tag{3.9}$$

The respective derivation $D^2(I)$ is

$$D^2(I) := \frac{1}{size(\Omega) - 1} \sum_{\Omega} (I(\mathbf{x}) - \bar{I})^2. \tag{3.10}$$

By introducing an weighting factor κ the *statistical cost function* F_S can be given:

$$F_\text{S}(S,R) := \left(\sqrt{D^2(S)} - \sqrt{D^2(R)} \right)^2 + \kappa \left(E(S) - E(R) \right)^2. \tag{3.11}$$

Optimization

Due to the discrete nature of the intensity space Ψ, the cost function is not continuous. Standard methods to optimize such functions are Powell's direction set [34] and genetic optimization [45]. Additionally, a new search pattern was implemented that works on a finite grid: For all image pairs (*R, S*), it exists a $\tau \in \mathbb{R}, \tau > 0$, with

$$A(b_0, c_0, \tau) := [b_0 - \tau, b_0 + \tau] \times [c_0 - \tau, c_0 + \tau] \subset \mathbb{R}^2, \tag{3.12}$$

so that $(b,c)_\text{min} \in A$, A is called the search area with center (b_0, c_0) and spread τ. Let $g \in \mathbb{N}$ be the grid constant. Then a search grid on $A(b_0, c_0, \tau)$ is defined as

$$G := \left\{ (b,c) | b = \pm\tau \frac{i}{g} + b_0, c = \pm\tau \frac{j}{g} + c_0, \ g \in \mathbb{N}, i, j = 0, 1, ..., g \right\}. \tag{3.13}$$

The grid search approach for automatic intensity adaption is then given by restricting the search to the grid points

$$(b,c)_\text{min} := \arg \min_{(b,c) \in G} F(S(b,c), R). \tag{3.14}$$

Usually, the center of the search area will be set (0,0). A sufficient minimum of the cost function will obviously surrendered by using a sufficient large spread τ, which ensures $(b,c)_\text{min} \in A$, and by using a high grid constant g.

In order to reduce computational load, a coarse to fine search pattern will be employed which utilizes only a small grid constant and adapts the search center while the spread of the search area will be reduced simultaneously. A minimal value of the spread τ_{min} and a minimal value ε of the cost function are stopping conditions. In the following, this optimization method will be called *grid search*.

3.4 Experiments

To test the cost functions and search strategies, three experiments were executed: First, an original MR image *I* was taken, and its intensity distribution was changed according to (3.2)

value recover error		F_S		F_V		F_H	
		$\overline{\Delta b}$	$\overline{\Delta c}$	$\overline{\Delta b}$	$\overline{\Delta c}$	$\overline{\Delta b}$	$\overline{\Delta c}$
1	grid	0.00	0.00	0.00	0.00	0.00	0.00
	genetic	0.00	0.01	0.00	0.01	0.01	0.01
	powell	0.00	0.00	0.00	0.00	0.01	0.02
2	grid	0.01	0.02	0.02	0.09	0.02	0.03
	genetic	0.01	0.03	0.03	0.11	0.02	0.04
	powell	0.01	0.03	0.03	0.11	0.08	0.11

Table 3.1: Parameter recover errors: In the first experiment grid search recovers intensity adjustment parameters perfectly, the other methods show very small errors. In the second experiment all search methods perform comparable well with the statistical cost F_S.

by using 80 different pairs of values for brightness b and contrast c to create images $\tilde{I}$. Then, the intensity of both images was automatically adjusted back and forth. In the second experiment, each image $\tilde{I}$ was additionally deformed non-rigidly prior to intensity adjustment. Finally, in the last experiment, the intensities of pairs of serially acquired MR images were adjusted automatically.

In all cases, the intensity threshold h of the significant domain Ω_h was set to 60. This value is lower then the voxel intensity of the white and gray matter in common MR images, but it masks out most of the background noise, especially outside of the head volume. The search area $b \times c$ was set to $[-2,2] \times [-2,2]$. Powell's direction set used 16 line segments, the grid search constant g was set to 32, and genetic optimization used a population of 100 members over 100 generation with a mutation rate of 0.07, a crossover rate of 0.9 and an extinction rate of 0.8. The statistical cost function F_S (3.11) was optimized with the weighting factor κ set to 1.0, and the histogram cost function used a filter width of $w = 11$. The comparison of the methods was done by measuring the ratio between the value of the three cost function $F_\mathrm{V}, F_\mathrm{H}, F_\mathrm{S}$ before and after the adjustment

$$C_* := \frac{F_*(S(b_{\mathrm{min}}, c_{\mathrm{min}}), R)}{F_*(S,R)}, \; * \in \{S, V, H\}, \tag{3.15}$$

and by measuring the computation time needed. When adjusting the original images to the changed images in Experiment 1 and 2, an additional comparison of the original values of brightness and contrast with the estimated values was possible.

3.5 Results and Discussion

The first experiment demonstrated that all combinations of cost functions and optimization methods are able to recover the values used to change the intensity distributions of an image with a very small error (see Table 3.1). If the images are additionally deformed non-rigidly, the minimization of F_S (3.11) yields minimal recovery errors for all optimization methods. Additionally, grid search and genetic optimization perform well if F_H is used (3.8).

cost decrease ratio		F_S			F_V			F_H		
		C_S	C_V	C_H	C_S	C_V	C_H	C_S	C_V	C_H
1	grid	0.01	0.04	0.21	0.01	0.04	0.20	0.08	0.09	0.16
	genetic	0.01	0.03	0.21	0.01	0.03	0.21	0.07	0.09	0.18
	powell	0.01	0.03	0.20	0.01	0.03	0.20	0.07	0.09	0.16
2	grid	0.02	0.24	0.31	0.10	0.23	1.22	0.03	0.24	0.13
	genetic	0.02	0.23	0.22	0.10	0.23	1.24	0.03	0.24	0.20
	powell	0.01	0.23	0.33	0.09	0.23	1.23	0.14	0.30	0.17
3	grid	0.01	0.90	0.98	188.48	0.85	26.57	0.44	0.91	0.49
	genetic	0.43	0.90	1.07	370.72	0.85	60.02	0.82	0.90	0.60
	powell	0.05	0.90	1.06	368.67	0.85	60.37	0.45	0.91	0.51

Table 3.2: Ratio of cost function value between before and after intensity adjustment. In the first and second experiment all methods yield a similar optimization of the used cost function. In the last experiment grid search performs best when using F_S or F_H as cost function. With these cost functions Powell's direction set performs better then genetic optimization.

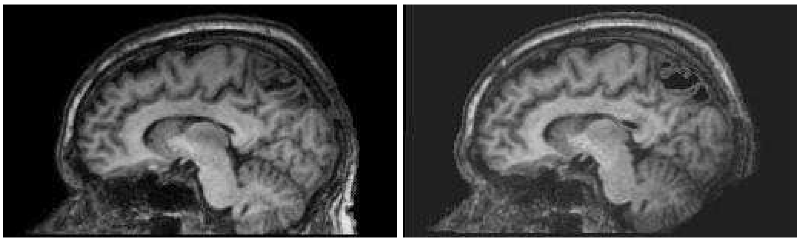

(a) reference (b) F_S

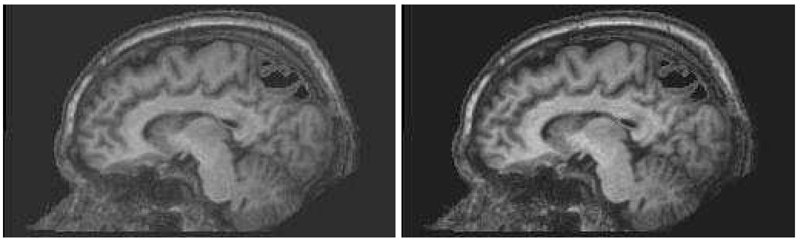

(c) F_V (d) F_H

Figure 3.2: A T1-weighted MR image was intensity adjusted to a reference image (a) using Powell's direction set. Statistical cost (b) and histogram cost (d) yield good results. Note the decrease of contrast in when optimizing the voxel based measure (c).

Table 3.2 shows that all optimization methods yielded a comparable optimization of the cost function used in the experiments with synthetic intensity changes, whereas grid search always offered a slight advantage over the other optimization methods in the third experiment.

Powell's direction set also yielded better optimization of the statistical cost F_S (3.11) and the histogram cost F_H (3.8) then the genetic optimization.

If the voxel cost function F_V (3.5) is used in the third experiment, the values of the other cost functions increased, while optimizing F_H and F_S also decreased (or at least maintained) the other cost function values. This conforms with the statement that anatomical variations, noise, and artifacts alter the behavior of F_V compared to statistical measures like used in F_H and F_S. A visual inspection of the adjustment results supports this statement, additionally (Fig. 3.2).

The decrease of contrast, when using F_V (Fig. 3.2(c)), can be interpreted as follows: In the study image (Fig. 3.1, right), an intensity inhomogeneity is present, which can not be found in the reference image (Fig. 3.1(left) and Fig. 3.2(a)). Thus, even with only small anatomical variations, voxels comprising the same materials in the reference image may correspond to voxels with higher and lower intensities in the study image. F_V has its minimal value when all these voxels are mapped to the same intensity in the study image. Therefore, a decrease of contrast minimizes F_V. On the contrary, F_H and F_S optimize the all-over intensity distribution, and hence, preserve contrast better.

times in s		F_S	F_V	F_H
1	grid	6.74	8.35	8.15
	genetic	9.99	11.28	11.48
	powell	5.30	6.14	5.40
2	grid	6.60	62.24	8.59
	genetic	9.45	99.41	11.62
	powell	5.01	21.64	5.25
3	grid	6.47	179.48	8.54
	genetic	10.21	299.98	11.58
	powell	4.62	59.78	5.21

Table 3.3: Adjustment times: Powell's direction set gives fastest results, followed by the multi-grid search. The voxel based cost function yields high processing times.

Finally, Table 3.3 shows that optimizations using the statistical cost function F_S are the fastest, followed by the histogram cost function F_H. The evaluation the voxel cost function F_V is computationally intensive. Powell's direction set is the fastest optimization method, and genetic optimization is significantly slower then grid search.

3.6 Conclusion

Using Powell's method to minimize the statistical cost function F_S offers the fastest approach to automatic intensity adjustment. Since it preserves more information of the image data, the histogram cost function F_H may be considered to be the better choice. It should be optimized by using grid search, for this method yields a better optimization of this cost function then Powell's direction set (with only a low speed penalty, see Table 3.3).

Chapter 4

Quantification of Deformation

Non-rigid registration is the tool to quantify the relevant differences in time series medical images. A comprehensive overview of registration approaches has been given by Maintz and Viergever [74]. In this chapter, a brief review of the development of non-rigid registration will be given and further focus will be laid on Christensen's fluid dynamics based approach [23]. New optimizations to this algorithm will be presented that enable its application on *of the shelf* PC hardware. The results of this chapter were partially published in Wollny and Kruggel [120].

4.1 Approaches to Non-Rigid Registration

Re-consider the minimization problem of registration (2.9) from Section 2.3:

$$T_{\text{reg}} := \arg\min_{T\in\mathbb{T}} \left(F_{\text{cost}}(S_T, R) + \kappa E(T)\right). \tag{4.1}$$

In order to solve this minimization problem (4.1), the roots of its first order derivative, determined by

$$\kappa \frac{\partial}{\partial T} E(T) = -\frac{\partial}{\partial T} F_{\text{cost}}(S_T, R), \tag{4.2}$$

can be consulted.

Here, the first order derivative of the cost function defines a force **f**, driving the registration:

$$\mathbf{f}(\mathbf{x}) := \left.\frac{\partial}{\partial T}\right|_{\mathbf{x}} F_{\text{cost}}(S_T, R). \tag{4.3}$$

Since the shape of an object in the images is not necessarily preserved in non-rigid registration, a smoothing term $E(T)$ has to be used in (4.2), i.e. $\kappa > 0$.

Different smoothing terms $E(T)$ are discussed in the literature. Several approaches to non-rigid registration are based on the the Navier-Stokes-operator (Segel [97]), here modified to account for non-mass-conserving deformations (Christensen et al. [24]),

$$\mathfrak{L} := \mu\nabla^2 + (\mu + \lambda)\nabla(\nabla\cdot), \tag{4.4}$$

with Lamé's elasticy constants μ (shear) and λ (dilatation).

Linear elastic smoothing can be formulated in terms of this operator:

$$\mathfrak{L}\mathbf{u}(\mathbf{x}) = -\mathbf{f}(\mathbf{x}), \tag{4.5}$$

with, $\mathbf{x} \in \Omega$, $T(\mathbf{x}) := \mathbf{x} - \mathbf{u}(\mathbf{x})$.

As an alternative, the energy regularisation may be based on a fluid-dynamical model. The formulation is similar to the linear elasticy, also by using the Navier-Stokes-operator $\mathfrak{L}$ (4.4), but acting on the velocity field $\mathbf{v}$:

$$\mathfrak{L}\mathbf{v}(\mathbf{x},t) = -\mathbf{f}(\mathbf{x}). \tag{4.6}$$

In this case, the connection between the velocity and the displacements has to be given (Christensen [23], see also Appendix A.1):

$$\mathbf{v}(\mathbf{x},t) = \frac{\partial \mathbf{u}(\mathbf{x},t)}{\partial t} + \nabla \mathbf{u}(\mathbf{x},t)\mathbf{v}(\mathbf{x},t). \tag{4.7}$$

Other smoothness measures introduced are based on *thin plate splines* (Bookstein [10], Evans et al. [36]), or diffusion (Cachier et al. [19], Fischer and Modersitzki [37], Thirion [107]), but will not further be discussed here.

Besides the energy regularisation, non-rigid registration approaches are also distinguished based on the formulation of the cost function; feature based methods and voxel based methods are known.

Feature based approaches

Feature-based approaches use information from identifiable brain structures, such as landmarks, curves, and surfaces. At first, these structures have to be extracted and set into correspondence. Then, the distance between corresponding structures is used as a cost function to drive the registration. The spatial transformations, resulting from feature matching, are finally propagated to the whole volume by using some energy regularisation $E(T)$.

Evans et al. [36] introduced non-rigid registration based on landmarks utilizing thin-plate interpolating splines (Bookstein [10, 11]) to propagate the registration to the whole image domain. Exact landmark placement is mandatory for this approach but hard to achieve (cf. Beil et al. [8], Frantz et al. [41, 42]). Therefore, Rohr et al. [93, 94] introduced approximating thin-plate splines to cope with landmark localization errors. Landmarks can have a weight according to their localization uncertainty, and hence, a control of the influence of the landmarks on the registration result is added. In a further extension, Fornefett et al. [38] added a mapping of landmark orientations as a new constraint to the registration. With this method, rigid parts of images are better preserved during registration. However, Fornefett also notes that landmarks have to be well distributed over the image domain in order to achieve good registration results.

Davatzikos et al. [31] automated the finding of corresponding features in head images by using a deformable surface algorithm [30], in order to obtain a one-to-one mapping between approximations of the cortical surfaces. Whence it is possible to determine some corresponding regions in a highly automated way. Nevertheless, anatomical variability in individual brain features still yields considerable localization errors. Depending on the parameters used, the linear elastic model either restricts the registration to small deformations, or yields an ill conditioned problem with a variety of possible solutions. Therefore, this method is not well suitable to handle large deformations. To overcome this limitation, Peckar et al. [84] introduced a parameter free approach to landmark based registration. Their model does not contain any material properties, such as elasticity constants, yielding a well conditioned problem.

In a recent work, Joshi and Miller [62] used a fluid dynamics based smoothing to propagate landmark correspondences to the whole image space. They gave conditions for the existence of a diffeomorphism in the solution space, since restriction to diffeomorphic transformations is crucial for physical consistence in this approach.

In summary, landmarks provide an effective constraint for non-rigid registration, but their extraction and correspondence is a difficult task that usually needs human interaction.

Voxel based approaches

In voxel based approaches, the force in (4.2) is derived from local or global image intensity similarity measures. The advantage of these methods lies in the independence of human interaction. Though, especially in the case of large differences between the images, the mapping of structures might be simply wrong, i.e. corresponding identifiable structures, as used in feature based approaches, may not map onto each other.

Bajcsy and Kovacic [4] published a seminal paper on a general purpose method for non-rigid registration of 3D image data by utilizing a cost function based on local voxel similarity and by using linear elastic smoothing. A multi-resolution approach was employed to achieve a global matching, to allow large deformations, and to reduce computational complexity. The computation of the similarity function to obtain the deforming forces was the most time consuming step during each iteration. Christensen et al. [25] relied on the Bayesian approach to map a digital anatomical MR-textbook of the brain to individual data sets. They showed that it is possible to map all information of the text book to the individual brain, and that MR based textbook information can be used to improve output obtained from images acquired by using different imaging modalities. Unfortunately, linear elasticy restricts the ability of non-rigid registration to handle large deformations which are necessary for mapping an atlas to individual brains. To overcome this limitation, Christensen et al. [26] later extended their work and described a registration approach in which a viscous fluid model (4.6) was used to control the deformation. In particular, the study image is modeled as a viscous fluid which is able to flow so as to match the reference image. Due to attenuation, internal forces disappear in this model and registration can be achieved, even when large scale deformations are required. To preserve the topology with this model, a “re-gridding” method, which will be discussed later, had to be introduced to ensure a positive Jacobian. The forces driving the transformation are derived from the sum of squared differences (2.12). With their circle-to-C experiment they showed that large deformations can be modeled nicely when using viscous fluids (Fig. 4.1). Therefore, the method is able to deal with large local anatomical variability and is applicable for the inter-subject registration of neuro-anatomical structures.

Bro-Nielsen [13] extended the work of Christensen [23] by introducing digital filters derived from the linear Navier-Stokes operator (4.4), to speed up computation. They stated that using this filter reduced the registration time in the order of at least a magnitude.

Later, Lester et al. [69] added a further constraint to viscous fluid registration, variable

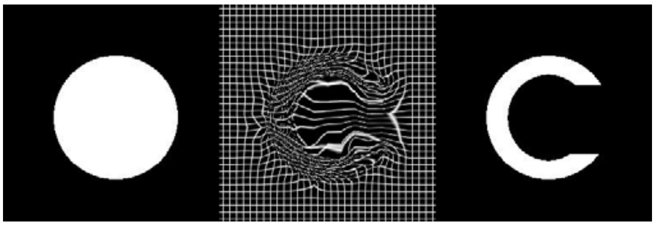

Figure 4.1: Registration of the circle (left) to the letter "C" (right). The middle image visualized the transformation obtained by the application of fluid dynamics based non-rigid registration.

viscosity: With three modifications to the data, they improved physical consistence of the registration:

- Regions are marked, whether they contribute actively to the registration or not, i.e. forces derived from the image data are weighted.
- Pixels are labeled *motionless* or *mobile*, and the velocities, and thus displacements at motionless locations, remain zero during the solution of the registration.
- The viscosity parameter varies spatially over the image.

Since topology preservation is a crucial aspect of non-rigid registration on discrete lattices, Musse et al. [79] recently proposed a new topology preserving constraint into non-rigid registration. Contrary to existing approaches that track discrete approximations of the Jacobian on a discrete image lattice, their approach enforces the Jacobian to be positive over the whole image domain to ensure topology preservation. Still, this method has its limitations concerning very large deformations, and Musse points out that in this case a viscous fluid approach is more appropriate.

4.2 The Non-Rigid Registration Based on a Fluid Dynamical Model

In this thesis, Christensen's approach was used to obtain non-rigid registration for the following reasons:

- The method is able to model large deformations, i.e. it is capable of modeling changes induced by pathologies, e.g. by tumors, injuries and infarcts, when brain matter appears or disappears to a larger extend.
- Only minimal pre-processing (the rigid registration and intensity adaption) is required.
- The model has a physical basis which uses material parameters. Knowledge about these parameters may be used to extend the method in the future, in order to enhance registration results.

However, the original implementation based on *successive over-relaxation* (SOR) is demanding, w.r.t. computional power, and therefore time consuming. Hence, different approaches for its solution are studied in order to select a method which offers superior registration speed while maintaining registration accuracy. The original algorithm of Christensen et al. [26] will be compared with the convolution based algorithm (CONV) of Bro-Nielsen [13] and an alternative, which is based on the minimum residual algorithm (MINRES), in terms of speed, memory usage, and registration accuracy. An optimization of SOR, which focuses on regions with significant deformations, will be studied, as well.

Since intensity-adaption is applied prior to the non-rigid registration, the sum of squared differences (2.12) can be used as a cost function. Thus, the deforming force **f** is given as its first order derivative

$$\mathbf{f}(\mathbf{x}-\mathbf{u}(\mathbf{x},t)) := -[S(\mathbf{x}-\mathbf{u}(\mathbf{x},t)) - R(\mathbf{x})]\ \nabla S|_{\mathbf{x}-\mathbf{u}(\mathbf{x},t)}\,. \tag{4.8}$$

An iterative scheme for the solution of the viscous fluids based registration can now be given which is based on the Navier-Stokes equation (4.6) as well as the connection between the velocity field **v** and displacement field **u** (4.7). With the integration time step parameter Δt and with the iteration index i it reads:

$$\mu\nabla^2\mathbf{v}(\mathbf{x},t_i) + (\mu+\lambda)\nabla(\nabla\cdot\mathbf{v}(\mathbf{x}.t_i)) = -[S(\mathbf{x}-\mathbf{u}(\mathbf{x},t_i)) - R(\mathbf{x})]\ \nabla S|_{\mathbf{x}-\mathbf{u}(\mathbf{x},t_i)} \tag{4.9}$$

$$\mathbf{u}(\mathbf{x},t_{i+1}) : = \mathbf{u}(\mathbf{x},t_i) + \Delta t * [\mathbf{v}(\mathbf{x},t_i) - \nabla\mathbf{u}(\mathbf{x},t_i)\mathbf{v}(\mathbf{x},t_i)]\,. \tag{4.10}$$

In each iteration, time step Δt is chosen according to

$$\Delta t := \frac{d}{\max_{\mathbf{x}\in\Omega}\|\mathbf{v}(\mathbf{x},t_i) - \nabla\mathbf{u}(\mathbf{x},t_i)\mathbf{v}(\mathbf{x},t_i)\|}, \tag{4.11}$$

d is a parameter for adaptive control of the integration time step and should be chosen from an interval $[d_{\min}, d_{\max}]$, to permit a smooth but steady deformation. $\Delta d \ll d_{\max} - d_{\min}$ is used to re-adjust d during the registration.

Smoothing with the Navier-Stokes operator $\mathfrak{L}$ ensures topology preservation on the continuous image domain Ω. Unfortunately, this is not the case on its discretization $\widehat{\Omega}$. Thus, the Jacobian J (2.4) has to be preserved from falling below a certain threshold on the discretized image domain $\widehat{\Omega}$; Christensen et al. [26] achieve this by re-gridding: Every time the Jacobian J falls below the heuristic value 0.5, the global deformation T is updated $T := T \oplus T_t$ by using the current transformation $T_t := \mathbf{x} - \mathbf{u}(\mathbf{x},t)$, and a new template $\tilde{S}$ is generated by applying the new global transformation $\tilde{S} := S(T)$. The displacement field **u** and time t are set to zero, and for further registration the new template $\tilde{S}$ is used. The full registration algorithm is outlined in Appendix B, Algorithm 1.

Note, that the registration of high resolution images is performed best by employing a coarse to fine multi-resolution strategy, as outlined in section 2.6, in order to improve registration speed and to avoid local minima of the cost function.

4.3 Solving the Linear PDE of Fluid Dynamics

The core problem and most time consuming step in algorithm 1 is the solution of PDE (4.9) for constant time and force. Now different approaches for solving (4.9) on a discretized coordinate domain $\widehat{\Omega}$ (2.17) are discussed to obtain a numerical solution of this PDE (4.9) with a necessary precision in a short computation time. These approaches are (A) successive over-relaxation, (B) successive over-relaxation with adaptive update, (C) the minimal residual algorithm, and (D) convolution filters. They will be compared in terms of speed, memory usage, and accuracy of the resulting registration.

Successive Over-Relaxation (SOR)

Discretizing (4.9) by using finite differences [90] yields a linear system

$$\mathbf{A}\mathbf{v} = \mathbf{f},\, \mathbf{A} \in \mathbb{R}^{3n\times 3n},\, \mathbf{v},\mathbf{f} \in \mathbb{R}^{3n}. \tag{4.12}$$

One method to solve (4.12) is *successive over-relaxation* (SOR) [7, 35, 82, 90]. Splitting $A = (a_{r,s}) \in \mathbb{R}^{3n\times 3n}$ into a diagonal matrix $\mathbf{A}_d$, a lower left matrix $\mathbf{A}_l$, and an upper right one $\mathbf{A}_r$,

$$\mathbf{A} = \mathbf{A}_d + \mathbf{A}_l + \mathbf{A}_r; \tag{4.13}$$

the obtained iteration rule of SOR, with the iteration index l and the over-relaxation factor ω reads:

$$\mathbf{v}^{(l+1)} := \mathbf{v}^{(l)} + \omega\mathbf{A}_d^{-1}\left(\mathbf{f} - \mathbf{A}_l\mathbf{v}^{(l+1)} - (\mathbf{I} + \mathbf{A}_r)\,\mathbf{v}^{(l)}\right). \tag{4.14}$$

In each iteration, the component $\mathbf{v}_m$ of vector field $\mathbf{f}$ is updated with a residual

$$\mathbf{r}_m^{(l+1)} := \frac{\omega}{a_{mm}}\left(\mathbf{f}_m - \mathbf{v}_m^l - \sum_{j=1}^{m-1} a_{m,j}\mathbf{v}_j^{(l+1)} - \sum_{j=m+1}^{n} a_{m,j}\mathbf{v}_j^{(l)}\right). \tag{4.15}$$

Note that $j < m$ in the term $\sum_{j=1}^{m-1} a_{m,j}\mathbf{v}_j^{(l+1)}$, i.e. to evaluate $\mathbf{r}_m^{(l+1)}$, already updated elements of $\mathbf{v}$ are used.

The sparse structure of $\mathbf{A}$ yields that one update of the discretized velocity field $\mathbf{f}$ needs an order of $66n$ floating point operations ($O(66n)$ FLOPs) (Appendix B, Algorithm 2). The update scheme does not require additional memory cells for the iteration process.

Successive Over-Relaxation with Adaptive Update

Non-rigid registration is usually preceded by rigid registration. Thus, one may expect differences between the images only in certain regions of interest. Since a coarse-to-fine multi-resolution approach is used, large differences are roughly registered at coarser levels, yet. Hence, large regions of the images may have little (if any) influence on the solution of PDE (4.9).

By setting the residuum $\mathbf{r}_{i,j,k} = \mathbf{r}_m$ (4.15), in each iteration $\mathbf{v}_{i,j,k}$ depends only on the 19 values with indices $\beta \in \Im$:

$$\Im := \left\{ \begin{pmatrix} i \\ j \\ k \end{pmatrix}, \begin{pmatrix} i\pm 1 \\ j \\ k \end{pmatrix}, \begin{pmatrix} i \\ j\pm 1 \\ k \end{pmatrix}, \begin{pmatrix} i \\ j \\ k\pm 1 \end{pmatrix}, \begin{pmatrix} i\pm 1 \\ j\pm 1 \\ k \end{pmatrix}, \begin{pmatrix} i \\ j\pm 1 \\ k\pm 1 \end{pmatrix}, \begin{pmatrix} i\pm 1 \\ j \\ k\pm 1 \end{pmatrix} \right\}. \tag{4.16}$$

Therefore, it makes sense to update $\mathbf{v}_{i,j,k}$ only, if at least one residuum $\left\|\mathbf{r}_\beta\right\|$ ($\beta \in \Im$) is larger then a threshold value $\hat{r}$ evaluated in the preceding iteration step:

$$\hat{r} := \begin{cases} 0 & m = 1 \\ \overline{r}^{(m)} \cdot \frac{\overline{r}^{(m)}}{\overline{r}^{(m-1)}} \cdot \frac{1}{m^2} & otherwise \end{cases}, \tag{4.17}$$

with

$$\bar{r} := \frac{1}{X \cdot Y \cdot Z} \sqrt{\sum \|\mathbf{r}_{i,j,k}\|^2}. \tag{4.18}$$

To obtain all residues $\mathbf{r}_{i,j,k}$ initially, this threshold $\hat{r}$ is set to zero during the first iteration. Later on, the threshold is set to the average over the square norms $\bar{r}$ of the residual vectors combined with a term which involves the evolution of the respective residuum and another term to decrease the threshold in subsequent iterations. With an increasing number of iterations, the solution search space thus increases and converges to the search space of the original SOR. Therefore, if SOR is convergent, then SOR with adaptive update (SORA) will also converge. This update scheme (SORA) can also be seen as a variant of the Gauss-Southwell relaxation (Southwell [99]).

The number of operations needed for one update of the velocity field, depends on the input data, but is well below the O(66n) FLOPs that are needed for the unmodified SOR. Additional storage $O(n)$ is required for residues and update markers.

The Minimum Residual Algorithm (MINRES)

The solution of the linear system (4.12) can also be regarded as the minimum of:

$$\Phi(\mathbf{f}) := \frac{1}{2}(\mathbf{Av} - \mathbf{f})^2. \tag{4.19}$$

If $\mathbf{A}$ is a symmetric matrix, though not necessarily positive definite, the *minimum residual algorithm*[1] (Barrett et al. [7]), as a variant of the conjugate gradient method, can be employed to solve this minimization problem.

In the linear system (4.12), the diagonal elements of $\mathbf{A}$ are $a_{i,i} = 1$, thus the system can be considered as treated with a Jacobi pre-conditioner. For the simple structure, a multiplication with $\mathbf{A}$ is achieved with only $O(51n)$ FLOPs (Appendix B, Algorithm 4). Hence, solving (4.12) by using MINRES seems feasible. In summary, this algorithm requires $O(117n)$ FLOPs per iteration (Algorithm 4). No storage is required for $\mathbf{A}$, but the temporary vectors require $O(n)$ storage cells. Employing an adaptive update, similar to the one given for SORA, would break the search strategy of MINRES, which depends on orthogonal search directions. Therefore, an adaptive update was not considered.

Convolution Filters

Bro-Nielsen and Gramkov [14] suggested the usage of convolution filters for solving (4.9). A linear operator comprising the form of (4.9) is given as (4.4):

$$\mathfrak{L} := \mu\nabla^2 + (\mu + \lambda)\nabla(\nabla\cdot). \tag{4.20}$$

With a filter width parameter d, the filter components $\mathbf{L} \in \mathbb{R}^{3\times3}$ [13] (see Appendix A.4), and with $\mathbf{y}_{r,s,t} = (\frac{r}{d}, \frac{s}{d}, \frac{t}{d})^T \,|\, r,s,t \in [-d,d] \cap \mathbb{Z}$, the solution of PDE (4.9) at $\mathbf{x} \in \widehat{\Omega}$ can be calculated by convoluting the impulse response of operator $\mathfrak{L}$ with the input force $\mathbf{f}$:

---

[1] The usage of the standard conjugated gradient method (CG) is discouraged; without any boundary conditions, $\mathbf{A}$ is singular, and thus, not positive definite. For large n, $\mathbf{A}$ becomes ill conditioned and numerical experiments show that this will lead to an instable operation of CG, even if boundary conditions are specified.

$$\mathbf{v}(\mathbf{x}) = \sum_{r,s,t=-d}^{d} \mathbf{L}(\mathbf{y}_{r,s,t}) \cdot \mathbf{f}(\mathbf{x} - \mathbf{y}_{r,s,t}). \tag{4.21}$$

The filter components $\mathbf{L} \in \mathbb{R}^{3\times3}$ can be pre-calculated. For each location (r,s,t) in (4.21) a product with a 3×3 matrix and the sum of two 3D vectors have to be calculated. The computional cost for solving (4.9) on the discretized grid $\widehat{\Omega}$, therefore, is $O(18(2d+1)^3 n)$ FLOPs. Additional storage space is only needed for the filter components. It can be neglected, because the filter width is small compared to the image size. A given filter width restricts the maximum length of the deformation during a transformation step in the registration algorithm. For a filter width smaller than the largest image dimension, it is not possible to obtain an accurate solution of PDE (4.9). Thus, a multi-resolution approach for solving the registration problem is mandatory to accommodate large deformations [14].

Now, approaches A-D can be compared with respect to the respective computational costs as obtained above (Table 4.1). MINRES needs nearly twice as much FLOPs per iteration as SOR. Since conjugated gradient-based methods are known for their fast convergence, MINRES may still perform better. The cost of CONV increases very quickly with growing filter widths.

$\frac{\text{SOR}}{\text{iteration}}$	$\frac{\text{SORAU}}{\text{iteration}}$	$\frac{\text{MINRES}}{\text{iteration}}$	CONV$_3$	CONV$_5$	CONV$_7$	CONV$_9$
$O(66n)$	$\leq O(66n)$	$O(117n)$	$O(486n)$	$O(2250n)$	$O(6174n)$	$O(13122n)$

Table 4.1: Computational Cost to Solve (4.9); The individual cost of iterative methods is given per iteration. Subscripts of CONV denote the filter width. Note, the cost of MINRES is nearly doubled w.r.t. SOR, and the cost of CONV increases rapidly with larger filter widths.

To get a first impression of the performance ratio between CONV and iterative methods, for different filter sizes the number of iterations of the latter methods are now summarized, with which their theoretical computational cost exceeds that of the convolution based solver (Table 4.2) .

	CONV$_3$	CONV$_5$	CONV$_7$	CONV$_9$
SOR	8	35	94	199
MINRES	5	20	53	113

Table 4.2: Ratio of Cost of Iterative Methods w.r.t. CONV Number of iterations at which the computational cost of the iterative methods exceeds the cost of convolution filters. If the number of iterations to solve (4.9) can be restricted, using CONV with high filter order does not offer an advantage over the iterative methods.

These numbers indicate that using CONV with large filter sizes does not offer an advantage over iterative solvers, if the number of iterations can be restricted with these methods somehow. On the other hand, the minimum filter size must be chosen carefully to solve (4.9) with an adequate precision to achieve a good registration.

4.4 Experiments and Results

A first test was run to determine the performance of the iteration methods alone, i.e. outside the context of the registration problem, because the absolute cost of SOR, SORA and MINRES depends on the number of iterations to achieve some predefined relative residuum in the solution of PDE (4.9).

Discrete random force fields **f** were generated on a grid of $128 \times 128 \times 128$ voxels and (4.9) was solved. In the moment when the relative residuum of the solution fell below a certain threshold during the iteration, time and number of iterations were measured. If matrix **A** is a symmetric, positive definite, tridiagonal or block wise tridiagonal matrix, the theoretically optimal relaxation factor ω can be approximated by:

$$\omega = \frac{2}{1 + \sqrt{1 - \lambda^2}}, \tag{4.22}$$

with λ being the *spectral radius* of $\mathbf{A}_d^{-1}(\mathbf{A}_l + \mathbf{A}_r)$ [90, pp 84-85]. Since it is difficult to calculate the spectral radius, relaxation factors of 0.8, 1.0, 1.4, and 1.8 were used. A dynamic adaption scheme, known as Chebyshev acceleration, was also supposed [90, pp 84-85] but did not offer any improvement.

Fig. 4.2 (a) shows [2] that the minimal residual method (MINRES) requires least iterations to achieve a given relative residuum. However, in terms of computation time, as obtained by using a 450Mhz Pentium II based workstation, successive over-relaxation is faster (Fig. 4.2 (b)).

Since forces in the generated fields are distributed evenly over the domain, the adaptive update shows only a slight advantage. Better results are expected on realistic data, because forces will typically be localized. An (over-)relaxation factor of 1.0 achieves the best results for the relaxation based methods and will, therefore, be used in the following experiments.

	3	5	7	9
time (s)	23.9 (0.1)	111.4 (0.3)	312.5 (0.5)	723.4 (1.0)
$\frac{\text{res}(v_{sol})}{\text{res}(v=0)}$	0.44 (0.01)	0.42 (0.04)	0.40 (0.07)	0.39 (0.13)

Table 4.3: Time and accuracy for solving (4.9) using CONV; Average registration time (variance) and average relative residuum (variance) respectively, for solution of PDE (4.9) for 20 randomly generated $128 \times 128 \times 128$ force fields using convolution filters (CONV) w.r.t. filter width. Note, CONV is not able to solve (4.9) accurately by using the above small filter widths.

For a comparison this first experiment was also run with convolution filters, but they do not yield adequate results for the solution of PDE (4.9), at least not by using small filter widths (Table 4.3). This supports the statement that CONV does not yield a proper solution for (4.9) if the filter width is well below the images dimensions. Filters of higher order yield a high computional cost. Therefore, they offer no advantage over iterative methods and were, hence, not tested.

---

[2] Relaxation factors of 0.8 and 1.8 did not yield superior results over factors 1.0 and 1.4 and were, thus, omitted from figures.

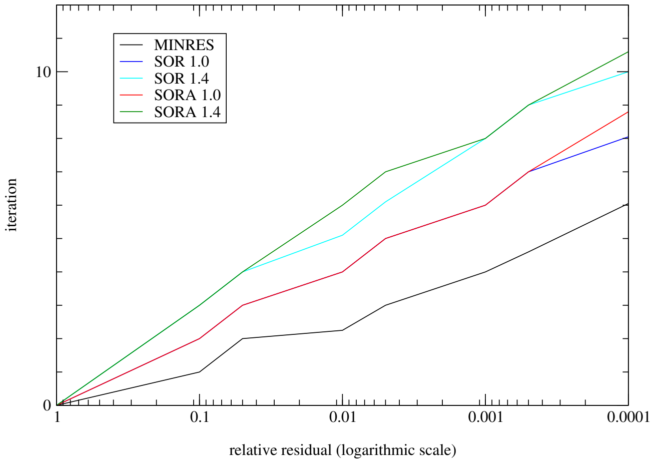

(a) Regarding the number of iterations, MINRES converges fastest.

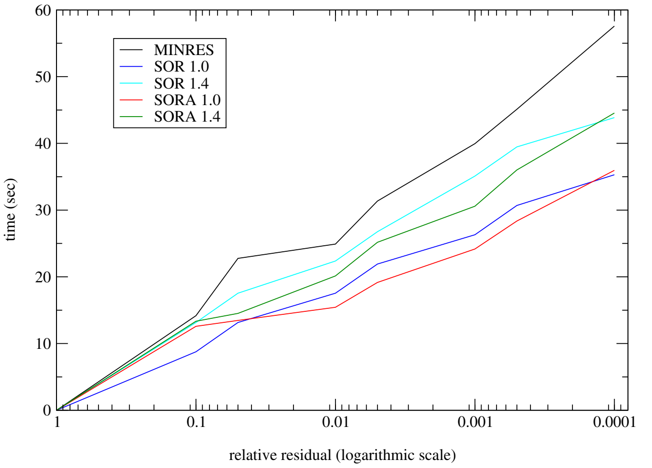

(b) SOR and SORA require less time, since their computational cost per iteration is well below that of MINRES

Figure 4.2: Iterative Methods: Number of iterations (a) and times (b) needed to achieve a certain accuracy (number of iterations and times averaged over 20 registration experiments).

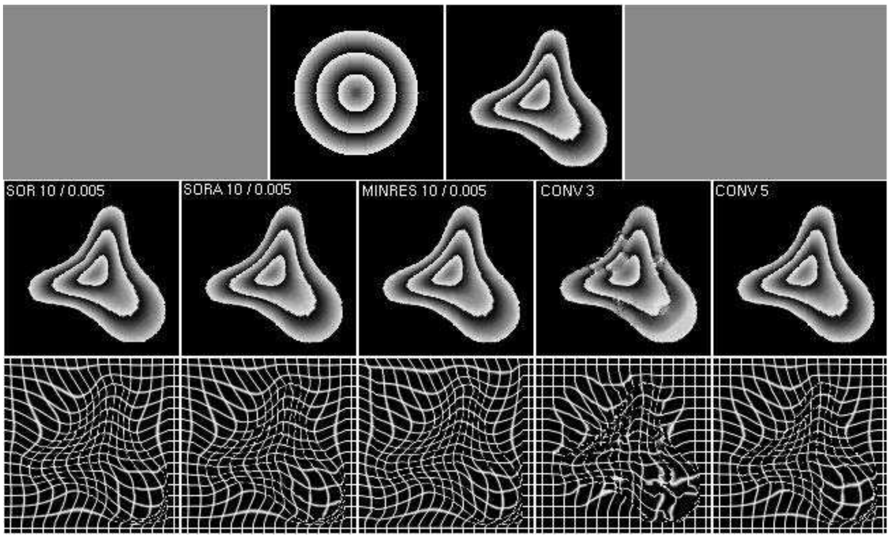

Figure 4.3: In the upper row, images associated with a registration of a synthetic study (left) and an example reference (right) are shown. Registration results are shown in the middle row, and the obtained deformations in the lower row. Iterative methods were applied using a limit of 10 iterations and $\varepsilon = 0.01$. Note the registration error when a very small filter width (CONV_3) is used.

The second experiment focuses on the performance of the different methods in the registration framework (Algorithm 1) for synthetic images of size $64 \times 64 \times 64$ (see also Fig. 4.3). Twenty reference images where generated by deforming the study with a smooth random deformation field; the study was then registered to these references. The time step interval $[d_{min}, d_{max}]$ was set to $[0.2, 0.8]$, the update parameter Δd was set to 0.1, $\mu = \lambda = 1.0$, and the multi-resolution start size was set to $16 \times 16 \times 16$.

In order to compare the registration results, the registration accuracy has to be measured somehow. Since it is difficult to define an absolute measure for the registration accuracy, a measure based on the relative value of the cost function will be used instead:

Definition 4.1. *With identity mapping* $T_0(\mathbf{x}) := \mathbf{x} \forall \mathbf{x} \in \Omega$ *and* $F_{cost}(S_{T_0}, R) \neq 0$*, the accuracy of registration achieved by the transformation* $T(\mathbf{x}) : \Omega \rightarrow \Omega$ *is defined as:*

$$A_{reg}(T) := \frac{F_{cost}(S_{T_0}, R)}{F_{cost}(S_T, R)}. \tag{4.23}$$

Given a perfect registration, this accuracy measure becomes infinite. However, during registration interpolation introduces errors in the image data. Therefore, infinite registration accuracy can not be expected.

The results shown in Table 4.4 suggest that it is not necessary to solve (4.9) with high accuracy. A limit of only 10 iterations yields a registration quality nearly as good as higher numbers of iterations.

For convolution filters, a minimum filter width of 5 is necessary to achieve results which are similar to those of the other methods (Tab 4.5, and Fig. 4.3). Unsatisfactory registration

	MINRES		**SOR**		**SORA**	
max iter	0.01	0.005	0.01	0.005	0.01	0.005
10	9.2 (1.2) 10.4 (1.2)	10.2 (2.0) 10.2 (1.4)	4.7 (1.0) 10.6 (1.3)	4.7 (1.3) 10.5 (1.3)	**3.5 (0.7)** 10.3 (1.3)	**3.5 (0.7)** 10.3 (1.3)
20	13.4 (2.8) 10.6 (0.9)	19.8 (6.3) 10.9 (1.1)	8.0 (1.6) 10.2 (1.1)	9.3 (1.8) 10.4 (1.1)	**5.7(1.0)** 10.0 (0.9)	**5.8(1.0)** 10.2 (1.1)
80	**26.0(4.5)** 10.5 (0.9)	**31.5(15.3)** 9.1 (2.5)	53.5 (17.4) 10.8 (0.8)	55.3 (16.9) 10.6 (0.9)	51.8 (10.7) 11.0 (0.7)	44.2 (10.3) 10.7 (0.7)

Table 4.4: Registration of synthetic images (iterative methods); A registration of synthetic 3D-images of size $64 \times 64 \times 64$ was performed. The respective registration time (upper row in cell), and the registration accuracy A_{reg} (lower row) were averaged over 20 registration experiments (variance in brackets). The best registration times per maximal number of iterations are emphasized using bold fonts. Registration accuracy using only 10 iterations to solve (4.9) is nearly as good as using more iterations. Thus, with a limited number of iterations, SORA performs best.

results for a filter width of 3 are another argument to support that a small filter is not sufficient to solve (4.9) with an adequate accuracy. Since the number of iterations in the iterative methods can be reduced significantly, the computational cost of CONV is similar to these methods, and any speed advantage vanishes. Only with filter width of 3, convolution filters offer an advantage in terms of speed but not in terms of accuracy. These results correspond to the ratio of computational costs as compiled in Table 4.2.

	CONV_3	CONV_5	CONV_7	CONV_9
time (min)	4.4 (0.5)	10.6 (2.5)	28.5 (8.0)	60.3 (13.7)
A_{reg}	5.0 (1.7)	10.9 (1.9)	11.2 (1.5)	11.3 (1.1)

Table 4.5: Registration of synthetic images (Convolution Filters); Registration of synthetic images of size $64 \times 64 \times 64$ by using convolution filters was performed. The respective registration times (upper row in cell) and registration accuracy (lower row) were averaged over 20 registration experiments. Note the low accuracy obtained for CONV_3.

The next test was designed to show how algorithms scale on image resolution by using the optimal parameters, as determined in the preceding experiment. For the iteration based methods, the maximum number of iterations were set to 10, or the iteration stopped if the relative residuum fell below 0.01. Convolution filters were applied with a filter width of 5. Although methods for solving (4.9) need $O(n)$ FLOPs, the time needed to achieve the registration of synthetic images increases at a lower rate then the number of pixels (see Fig. 4.4).

Another result is that SOR and SORA scale better than MINRES and CONV. The super-scalar speed increase for small resolutions (i.e. 32x32x32) is a consequence of caching [44]. SORA proved to be the fastest method.

The last experiment focuses on the performance of the registration of high-resolution medical image data. To generate the reference image, the study (a 250x250x192 MR image of the head) was first deformed with a Gaussian filtered deformation field with only small displacements (“jitter“ field) to simulate random differences due to different imaging conditions. Then, a deformation field of size 90x100x60 was applied to simulate pathological changes in

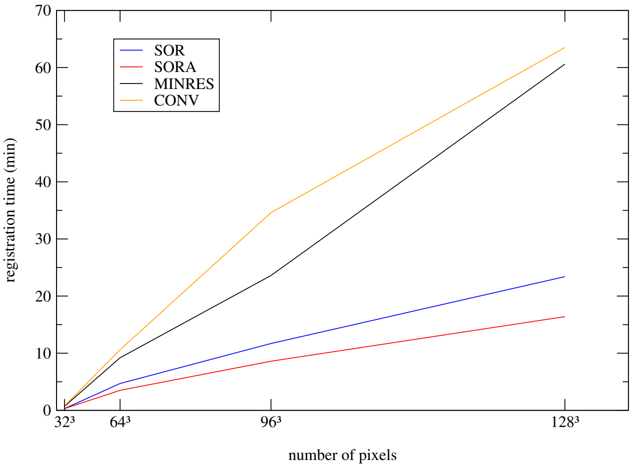

Figure 4.4: Scaling of the execution times with image size: All methods show a sub-proportional time increase w.r.t. images of size 64 × 64 × 64. SORA scales best.

the brain. Acceptable registration results were achieved in approximately 3 hours.

By employing architecture specific optimizations and parallelization, this performance can be improved further:

- At the Intel Pentium II 450MHz, the ratio of time to fetch data from the 1st Level cache vs. the 2nd Level cache vs. main memory is about 1:10:100 measured by using *memtest86* (Brady [12]). During a read from main memory not only the requested data is fetched, but a whole cache line of 32 byte [48]. Therefore, an re-ordering of the data access in the inner loop of SOR(A) (Algorithm 2) improved the reusage of the cache content.

- C++ allows the definition of operators to access 3D data fields like `field(x,y,z)`, and a similar construct in C would look like `field[z][y][x]`. While this notation enhances readability of the code, and was, therefore, used in the initial implementation of the algorithm, the speed penalty is very high: Five machine instructions – two integer additions, two integer multiplications, and the *mov* operation – are necessary to load data from memory. During a SOR(A) iteration the data is accessed sequentially, therefore, a linear addressing scheme, `field[index]`, can be used instead. On ix86 compatible hardware, this notation translates to only one machine instruction (Bentley [9], Wadleigh and Crawford [116]). Additionally, the neighboring elements needed for computation can be accessed by using linear relative offsets.

- By re-ordering of the instructions of the inner loop of SOR (Algorithm 2) to reduce dependencies in the computation, "stalls" are avoided, where the processor has to wait for temporary results (Fried [44]).

- The core step of the registration algorithm (Algorithm 1), the solution of PDE (4.9) was parallelized by using pthreads [17].

Finally, with the development of new hardware, execution times also reduce.

To measure the performance of the registration algorithm on a recent computer (Dual AMD Athlon 1.5GHz, 1GB RAM) and with the optimizations given above, 10 registration experiments with typical MR volume data sets ($200 \times 200 \times 256$ voxels) were executed. The results are summarized in Table 4.6, and show that non-linear registration based on fluid dynamics can now be done on low cost hardware in a reasonable amount of time.

single processor		dual processor	
average	max	average	max
15 min	23 min	11 min	16 min

Table 4.6: Registration times for MR images of size $200 \times 200 \times 256$. 10 registrations were executed. The average registration time is given as well as the maximum registration time.

4.5 Conclusion

Two iterative methods (*Successive Over-Relaxation* and the *Minimal Residuum Algorithm*) and a direct approach (*Convolution Filters*) were compared as methods for the solution of the core problem of non-rigid registration based on fluid dynamics, (4.9) was done. Considering the computional costs of the iterative methods, MINRES needs fewer iterations to solve (4.9) with a given accuracy, but SOR requires less memory cells and less time to achieve the same result and therefore is superior. Numerical experiments on synthetic data demonstrated that it is possible to restrict the numbers of iterations drastically, without a significant loss of accuracy of the registration result. With this optimization, SOR outperformed convolution filters (CONV) in terms of speed and still maintains registration accuracy. SOR was speeded up by introducing an adaptive update scheme (SORA). In summary, SORA proved to be the best approach to solve (4.9). By optimizing the implementation for the used target platform and with parallelization, the non-rigid registration of high-resolution medical images with the fluid dynamics model can now be achieved in approximately 15 minutes on low-cost PC hardware.

Chapter 5

Describing Vector Fields by Means of Critical Points

In this chapter, the transformation which describes the structural change in time series medical images will undergo a further analysis. The concept of *critical points* will be introduced, and a new approach, to detect *repellors* and *attractors* in vector fields will be presented and discussed. An experimental analysis of critical point detection in synthetically created vector fields concludes this chapter. The results of this chapter were partially published in Wollny et al. [121].

5.1 Motivation

After the quantification of differences between time series images by non-rigid registration, the displacements describing these differences are given as a voxel-wise vector field. To improve the perception of the field, and consequently, to improve the understanding of the monitored disease or treatment process, *critical points* are considered as introduced by Abraham and Shaw [1]. Classifying these points by their so called *phase portraits* helps localizing interesting regions, like growth centers or centers of matter loss, and interpreting the observed pathological process or the treatment process.

The detection and visualization of critical points is still an active research area on which rather sophisticated mathematical methods have been employed [53]. Established topological methods decompose vector fields in different global regions of interest based on local linear [55] or higher-order [95] approximations of the Jacobian. Philippou et al. [86] introduced a geometrical method where critical points are found at the intersection of lines tangent with the vector orientation (or at the intersection of planes orthogonal to the vectors). Methods based on the Poincaré-Hopf index theorem [e.g., 47] are also widely employed.

Due to the finite spatial resolution of the images, the displacement field is given on a discrete lattice. Since growth or atrophying processes, for example, take place in finite subcompartments of the brain, the representation of critical points by point sources would be an over-simplification. Therefore, most conventional methods fail to detect critical points when they are applied to medical vector fields. Hence, a novel method for critical point detection

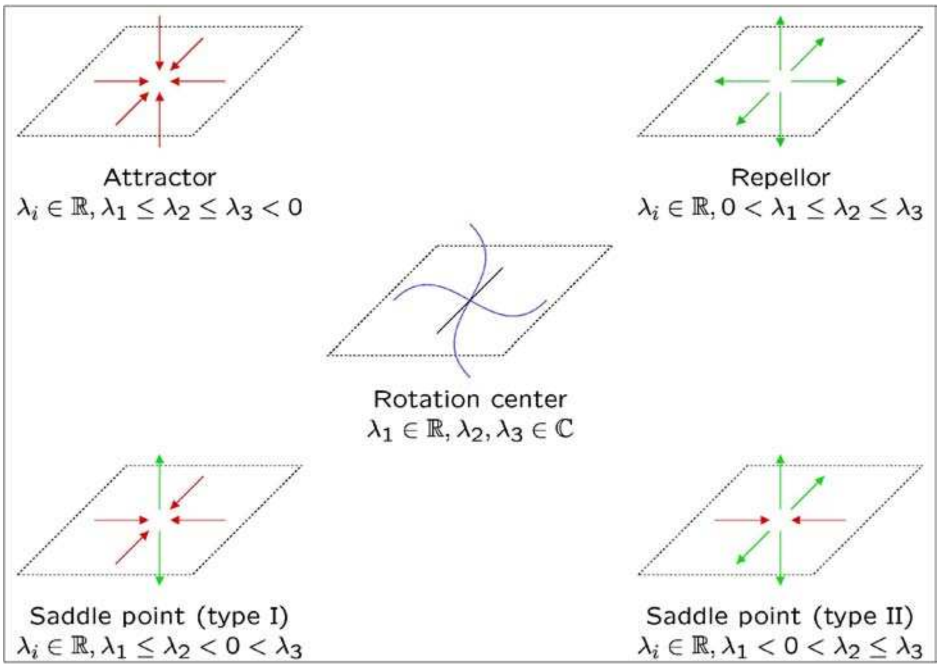
Attractor
$\lambda_i \in \mathbb{R}, \lambda_1 \leq \lambda_2 \leq \lambda_3 < 0$
Repellor
$\lambda_i \in \mathbb{R}, 0 < \lambda_1 \leq \lambda_2 \leq \lambda_3$
Rotation center
$\lambda_1 \in \mathbb{R}, \lambda_2, \lambda_3 \in \mathbb{C}$
Saddle point (type I)
$\lambda_i \in \mathbb{R}, \lambda_1 \leq \lambda_2 < 0 < \lambda_3$
Saddle point (type II)
$\lambda_i \in \mathbb{R}, \lambda_1 < 0 < \lambda_2 \leq \lambda_3$

Figure 5.1: Classification criteria for critical points (after Abraham et al. [1]). λ_i denote the eigenvalues of the phase portrait to a critical point.

is proposed. It is based on the contraction mapping theorem [15].

5.2 The Concept of Critical Points

Consider a vector field $\mathbf{u}$ defined on some compact domain $\Omega \subseteq \mathbb{R}^3$, and consider the set:

$$U_\varepsilon(\mathbf{x}') := \{\mathbf{x} | \parallel \mathbf{x} - \mathbf{x}' \parallel < \varepsilon, \mathbf{x} \in \Omega\}, \tag{5.1}$$

for any $\varepsilon > 0, \varepsilon \in \mathbb{R}$ and a $\mathbf{x}' \in \Omega$; the set U_ε is called the ε-*environment* of $\mathbf{x}'$.

The Taylor series expansion of $\mathbf{u}(\mathbf{x})$ about the point $\mathbf{x}'$ yields:

$$\mathbf{u}(\mathbf{x}) = \left.\frac{\partial u_i}{\partial x_j}\right|_{\mathbf{x}'} (\mathbf{x} - \mathbf{x}') + \mathbf{u}(\mathbf{x}') + o(\mathbf{x}). \tag{5.2}$$

By taking only its linear terms into account, and with the substitution $\mathbf{P} := \left.\frac{\partial h_i}{\partial x_j}\right|_{\mathbf{x}'}, \mathbf{P} \in \mathbb{R}^{3\times 3}$

$$\mathbf{u}(\mathbf{x}) = \mathbf{P}(\mathbf{x} - \mathbf{x}') + \mathbf{u}(\mathbf{x}'), \tag{5.3}$$

is obtained. Thus, it can now be defined [cf. 86]:

Definition 5.1. *A critical point* $\mathbf{x}_{cp}$ *is an equilibrium point in the vector field topology where* $\mathbf{u}(\mathbf{x}_{cp}) = 0$ *while there exists an* $\varepsilon > 0, \varepsilon \in \mathbb{R}$ *so, that* $\mathbf{u}(\mathbf{x}) \neq 0 \forall \mathbf{x} \in U_\varepsilon(\mathbf{x}_{cp}) \backslash \{\mathbf{x}_{cp}\}$.

Within the vicinity of a critical point $\mathbf{x}_{\text{cp}}$, the vector field $\mathbf{u}(\mathbf{x})$ — as it is outlined in (5.3) — can be approximated by

$$\mathbf{u}(\mathbf{x}) = \mathbf{P}(\mathbf{x} - \mathbf{x}_{\text{cp}}), \tag{5.4}$$

where the matrix $\mathbf{P}$ is called the *phase portrait* of the critical point $\mathbf{x}_{\text{cp}}$.

As a first-order Taylor series would have a limited scope in modeling $\mathbf{u}(\mathbf{x})$ adequately, i.e., the influence of critical point $\mathbf{x}_{\text{cp}}$ would decay with distance $\Delta\mathbf{x} = \mathbf{x} - \mathbf{x}_{\text{cp}}$, accuracy in modeling can be increased by introducing the attenuation factor $1/\| \mathbf{x} - \mathbf{x}_{\text{cp}} \|^2$. Consequently, the approximation of $\mathbf{u}(\mathbf{x})$ now reads

$$\mathbf{u}(\mathbf{x}) = \frac{1}{\| \mathbf{x} - \mathbf{x}_{\text{cp}} \|^2} \mathbf{P}(\mathbf{x} - \mathbf{x}_{\text{cp}}). \tag{5.5}$$

A critical point may be classified with respect to the eigenvalues of $\mathbf{P}$ (as proposed by Abraham and Shaw [1]): attractors, repellors, saddle points, and rotation centers are distinguished (see Fig. 5.1). For the application intended in this thesis, namely to interpret morphological changes of the brain, attractors and repellors may be interpreted as areas of matter loss and growth, respectively; saddle points may correspond to configurations at barriers or membranes, and rotation centers may indicate local tissue shearing.

5.3 Metric Space and Fix Points

For the estimation of attractors and repellors, the concepts of a metric space and a contraction mapping have to be reviewed.

Complete Metric Space

Given a set Θ, a function

$$d : \Theta \times \Theta \to [0, \infty) \tag{5.6}$$

is called a metric or distance function, if the following three conditions hold for all $x, y, z \in \Theta$:

$$\begin{aligned} d(x,y) = 0 \Leftrightarrow x = y & \qquad (\textit{identity}) \\ d(x,y) = d(y,x) & \qquad (\textit{symmetry}) \\ d(x,y) \leq d(x,z) + d(y,z) & \qquad (\textit{triangle inequality}). \end{aligned}$$

The pair (Θ, d) is called a *metric space.*

Let then $X = [x_i]_{i=0,1,\ldots}$ be a sequence in $\Theta \subseteq \bar{\Theta}$, and let $x \in \bar{\Theta}$, then X is said to converge to x

$$x_i \xrightarrow[i \to \infty]{} x \Leftrightarrow d(x_i, x) \xrightarrow[i \to \infty]{} 0. \tag{5.7}$$

Furthermore, X is said to be a *Cauchy sequence* in the metric space (Θ, d) if for any positive $\delta > 0$, $\delta \in \mathbb{R}$ there exists an integer $k \geq 0$ such that $d(x_i, x_j) \leq \delta \, \forall \, i, j \geq k$. This is equivalent to

$$d(x_i, x_j) \xrightarrow[i,j \to \infty]{} 0. \tag{5.8}$$

A metric space (Θ, d) is said to be *complete* if any Cauchy sequence $X = [x_i]_{i=0,1,\ldots}$ converges to some point $x \in \Theta$.

Attractors and Repellors as Contraction Transformation Fix Points

Given a complete metric space (Θ, d) with the distance function d defined over the set Θ and a transformation $f : \Theta \to \Theta$. A transformation f is called *contractive* on Θ if there is a constant $s \in [0, 1[$ such that

$$d(f(x), f(y)) \leq s \cdot d(x, y) \, \forall x, y \in \Theta. \tag{5.9}$$

Any such number s is called a *contractivity factor* for the transformation f.

Theorem 5.1. *Let $f : \Theta \to \Theta$ be a contractive transformation on a complete metric space (Θ, d). Then the transformation f possesses exactly one point $a \in \Theta$ with $f(a) = a$, and a is called* fix point *of transformation f. Moreover, for any $x \in \Theta$, the sequence $x, f(x), \ldots, f^k(x) := f(f^{k-1}(x)), \ldots$ or short*

$$\left[f^k(x)\right]_{k=0,1,\ldots} \tag{5.10}$$

converges to the fix point a, i.e.,

$$\lim_{k\to\infty} f^k(x) = a. \tag{5.11}$$

For a proof of this theorem see, e.g., [71]. Fix point a is also called the *attracting point* of set Θ.

Now consider a vector field $\mathbf{u}(\mathbf{x})$ defined on the domain Ω. Additionally assume

$$\mathbf{x} + \mathbf{u}(\mathbf{x}) \in \Omega \, \forall \mathbf{x} \in \Omega, \tag{5.12}$$

which holds for vector fields obtained by non-rigid registration of images defined on Ω.

With the Euclidean distance

$$d(\mathbf{x}, \mathbf{y}) := \|\mathbf{x} - \mathbf{y}\|_2 \, \forall \mathbf{x}, \mathbf{y} \in \Omega, \tag{5.13}$$

the pair (Ω, d) defines a metric space.

Using an Euclidean reference frame and taking assumption (5.12) into account, $\mathbf{u}(\mathbf{x})$ defines a transformation $T : \Omega \to \Omega$ through

$$T(\mathbf{x}) := \mathbf{x} + \mathbf{u}(\mathbf{x}). \tag{5.14}$$

For the limit of each Cauchy sequence $X = [\mathbf{x}_k]_{k=0,1,\ldots}$

$$\lim_{k\to\infty} \mathbf{x}_k = \mathbf{x} \in \Omega, \tag{5.15}$$

is in Ω, (Ω, d) is a complete metric space.

Now consider a fix point $\mathbf{a} \in \Omega$. The set

$$\Theta(\mathbf{a}) := \left\{\mathbf{x} | \mathbf{x} \in \Omega \wedge \lim_{k\to\infty} T^k(\mathbf{x}) = \mathbf{a}\right\} \tag{5.16}$$

is called the *attraction area* Θ of $\mathbf{a}$. For a consideration of the phase portrait $\mathbf{P}_\mathbf{a}$ and its eigenvalues, only fix points are taken into account which have the following property: It exists a positive number $\delta > 0$ with

$$\|\mathbf{u}(\mathbf{x})\| \neq 0 \, \forall \mathbf{x} \in U_\delta(\mathbf{a}) \backslash \{\mathbf{a}\} \wedge U_\delta(\mathbf{a}) \subseteq \Theta, \tag{5.17}$$

i.e., the attraction area of fix point **a** consists of at least a sphere with radius δ around fix point **a**, and the vector field is not zero in this sphere.

For the estimation of the eigenvalues, consider a subset of Θ

$$\tilde{\Theta} := \{\mathbf{x} | \mathbf{x} \in \Theta \wedge \|\mathbf{x} - \mathbf{a}\| < \varepsilon, \varepsilon \geq \delta\}. \tag{5.18}$$

Using (5.5) yields

$$\mathbf{P}(\mathbf{x} - \mathbf{a}) \approx \|\mathbf{x} - \mathbf{a}\|^2 \mathbf{u}(\mathbf{x}). \tag{5.19}$$

Since $\mathbf{x} \rightarrow \mathbf{x} + \mathbf{u}(\mathbf{x})$ for $\mathbf{x} \rightarrow \mathbf{a}$ and with substitution $\lambda = -\|\mathbf{x} - \mathbf{a}\|^2$ follows

$$\mathbf{P}\mathbf{u}(\mathbf{x}) \approx \lambda \mathbf{u}(\mathbf{x}). \tag{5.20}$$

This accounts for all vectors $\mathbf{u}(\mathbf{x}) \in \tilde{\Theta}$, and due to (5.17), $\tilde{\Theta}$ also contains a set of eigenvectors $\mathbf{u}_i \in \tilde{\Theta}$ of $\mathbf{P}_\mathbf{a}$. Therefore, all its three eigenvalues are less then zero $\lambda_1 \leq \lambda_2 \leq \lambda_3 < 0$ and fix point **a** is an attractor which can be seen from the classification in figure 5.1.

By replacing the transformation (5.14) with

$$T_{\text{inv}}(\mathbf{x}) := \mathbf{x} - \mathbf{u}(\mathbf{x}), \tag{5.21}$$

the fix points of sequences $\left[T_{\text{inv}}^k(\mathbf{x})\right]_{k=0,1,\ldots}$ yield repellors. The derivation is similar to the one given above.

5.4 Estimation Algorithm

Now the procedure to estimate attractors by using transformation T (5.14) and repellors by using T_{inv} (5.21), respectively, is described. This is done on the discretized domain $\widehat{\Omega}$ (2.17), with the grid constant g corresponding to the resolution of the studied input images that are registered by transformation T.

Cumulation

To find a fix points **a** in the deformation field **u**, a counter C has to be defined on $\hat{\Omega}$. With a threshold t, and

$$\hat{\Omega}_{\text{start}} := \left\{\mathbf{x} | \, \|\mathbf{u}(\mathbf{x})\| > t, t > 0, \mathbf{x} \in \hat{\Omega}\right\} \tag{5.22}$$

yields a set of sequence start points, that ensures attraction areas $\Theta(\mathbf{a}) \supset \{\mathbf{a}\}$, i.e. the attraction area will contain more then just the starting point. Now consider sequences $\left[T^k(\mathbf{x})\right]_{k=0,1,\ldots}$, $\mathbf{x} \in \hat{\Omega}_{\text{start}}$. When the breaking condition $\mathbf{u}(T^k(\mathbf{x})) < t$ is reached, the counter value $C(T^k(\mathbf{x}))$ is incremented. An additional condition, $k > k_{\max}$ obviates oscillation between accumulation points.

After iteration over all $\mathbf{x} \in \hat{\Omega}_{\text{start}}$, the distribution of counter values $C(\mathbf{x})$ reflects the distribution of fix points of the vector field **u**.

Clustering

Since the cumulation was performed on a finite domain $\hat{\Omega}$, two sequences, $\left[T^k(\mathbf{x}_1)\right]_{k=0,1,\ldots}$ and $\left[T^l(\mathbf{x}_2)\right]_{l=0,1,\ldots}$, are considered to converge to the same fix point $\mathbf{a}$, if for a certain value $\alpha > 0$, $\alpha \in \mathbb{R}$, the following assumption is fulfilled:

$$\mathbf{u}(T^k(\mathbf{x}_1)) < t \wedge \mathbf{u}(T^l(\mathbf{x}_2)) < t \rightarrow \left\| T^k(\mathbf{x}_1) - T^l(\mathbf{x}_2) \right\| < \alpha. \tag{5.23}$$

Here, α should be chosen to be based on the resolution of the grid $\hat{\Omega}$. A convenient value is half a voxel size.

Attracting points are finally obtained by clustering counter C: Given a threshold h, first, find a seed point $\mathbf{s} \in \hat{\Omega}$ with $C(\mathbf{s}) > h$ and create a point size cumulation area $\Theta_\mathbf{s}$. Then, the cumulation area $\Theta_\mathbf{s}$ is grown by adding neighboring grid points $\mathbf{x}$ as long as $C(\mathbf{x}) > h$. After the growth of area $\Theta_\mathbf{s}$ is finished, its center of gravity is calculated, weighting with the counter values $C(\mathbf{x})$, $\mathbf{x} \in \Theta_\mathbf{s}$ and then used as critical point location:

$$\mathbf{x}_{\mathrm{cp}} := \frac{\sum_{\mathbf{x} \in \Theta_\mathbf{s}} C(\mathbf{x})\mathbf{x}}{\sum_{\mathbf{x} \in \Theta_\mathbf{s}} C(\mathbf{x})}. \tag{5.24}$$

Finally, for each $\mathbf{x} \in \Theta_\mathbf{s}$ set $C(\mathbf{x}) := 0$, to ensure that the same points $\mathbf{x}$ are not further used for clustering.

Repeat this procedure until $C(\mathbf{x}) \leq t \, \forall \mathbf{x} \in \hat{\Omega}$.

Phase Portrait Estimation and Classification

Using the approximation of vector field $\mathbf{u}(\mathbf{x})$ in the environment of a critical point $\mathbf{x}_{\mathrm{cp}}$ (5.5), and substituting $\Delta\mathbf{x} := \mathbf{x} - \mathbf{x}_{\mathrm{cp}}$ yields

$$\|\Delta\mathbf{x}\| \, \mathbf{u}(\mathbf{x}_{\mathrm{cp}} + \Delta\mathbf{x}) = \mathbf{P}(\Delta\mathbf{x}). \tag{5.25}$$

Considering a certain environment of $\mathbf{x}_{\mathrm{cp}}$ and taking (5.25) into account, this yields an overdetermined system of linear equations [86] that can be solved by using Householder transformations [90]. Since $\mathbf{A}$ is a 3×3 matrix, calculating the eigenvalues and thus a classification of critical point $\mathbf{x}_{\mathrm{cp}}$ can easily be done by solving

$$\det(\mathbf{P} - \lambda\mathbf{I}) = 0 \tag{5.26}$$

using Cardan's formula [90].

Validation of Critical Point Detection

In order to validate the algorithm, outlined above, the following experiment was run: First, a set of critical points $P_{\mathrm{cp}} := \{\mathrm{cp}_i\}$, all attractors or repellors, was generated. Then, a vector field $\mathbf{u}$ was generated by superposition:

$$\mathbf{u}(\mathbf{x}) := \sum_{\mathrm{cp} \in P_{\mathrm{cp}}} \frac{\mathbf{P}_{\mathrm{cp}} \cdot \left(\mathbf{x} - \mathbf{x}_{\mathrm{cp}}\right)}{\|\mathbf{x} - \mathbf{x}_{\mathrm{cp}}\|^2} \, \forall \mathbf{x} \in \widehat{\Omega}. \tag{5.27}$$

The vector field $\mathbf{u}$ was then used as input for the critical point estimation algorithm. Finally, a comparison between the estimated critical points $P_{\mathrm{cp}}^{(\mathrm{est})}$ and the original points P_{cp} was done in terms of number of estimated points, the location error

$$\varepsilon_{\mathrm{loc}} := \sum_{\mathrm{cp} \in P_{\mathrm{cp}}} \min_{\mathrm{cp}^{(\mathrm{est})} \in P_{\mathrm{cp}}^{(\mathrm{est})}} \|\mathbf{x}_{\mathrm{cp}}^{(\mathrm{est})} - \mathbf{x}_{\mathrm{cp}}\|, \tag{5.28}$$

the error in phase portrait estimation,

$$\varepsilon_{\mathrm{pp}} := \sum_{\mathrm{cp} \in P_{\mathrm{cp}}} \min_{\mathrm{cp}^{(\mathrm{est})} \in P_{\mathrm{cp}}^{(\mathrm{est})}} \|\mathbf{P}_{\mathrm{cp}}^{(\mathrm{est})} - \mathbf{P}_{\mathrm{cp}}\|, \tag{5.29}$$

and the field reconstruction error, with $\mathbf{u}^{(\mathrm{est})}$ being the vector field created by superposition (5.27) from the estimated critical points $P_{\mathrm{cp}}^{(\mathrm{est})}$

$$\varepsilon_{\mathrm{field}} := \sum_{\mathbf{x} \in \widehat{\Omega}} \sqrt{\|\mathbf{u}^{(\mathrm{est})}(\mathbf{x}) - \mathbf{u}(\mathbf{x})\|^2}. \tag{5.30}$$

		1	2	3	4
64^3	n_{cp}	1.00 ±0.00	1.25 ±0.44	1.50 ±0.51	1.65 ±0.75
	$\varepsilon_{\mathrm{loc}}$	1.76 ±1.72	2.82 ±1.80	2.36 ±1.38	1.93 ±1.32
	$\varepsilon_{\mathrm{pp}}$	0.74 ±1.28	5.37 ±2.94	5.28 ±3.29	4.01 ±2.41
	$\varepsilon_{\mathrm{field}}$	0.29 ±0.15	0.61 ±0.24	0.54 ±0.25	0.54 ±0.17
128^3	n_{cp}	1.00 ±0.00	1.75 ±0.44	2.25 ±0.64	3.05 ±0.67
	$\varepsilon_{\mathrm{loc}}$	1.84 ±1.26	2.35 ±2.40	1.82 ±1.12	1.50 ±1.03
	$\varepsilon_{\mathrm{pp}}$	1.13 ±0.97	5.22 ±4.51	4.30 ±2.95	2.56 ±1.45
	$\varepsilon_{\mathrm{field}}$	0.22 ±0.10	0.45 ±0.36	0.41 ±0.27	0.49 ±0.24
256^3	n_{cp}	1.00 ±0.00	1.75 ±0.44	2.75 ±0.44	3.55 ±0.76
	$\varepsilon_{\mathrm{loc}}$	0.56 ±0.28	2.33 ±2.45	1.49 ±0.80	1.78 ±1.30
	$\varepsilon_{\mathrm{pp}}$	0.37 ±0.29	6.21 ±11.70	3.31 ±3.51	3.24 ±3.85
	$\varepsilon_{\mathrm{field}}$	0.07 ±0.03	0.25 ±0.14	0.28 ±0.14	0.31 ±0.18

Table 5.1: Results of critical point estimation of randomly created vector fields with respect to the field size (rows) and the number of critical points to create the fields (columns). Displayed are the number of detected critical points, the location error of the detected points (5.28), the error of the estimated phase portrait (5.29), and the relative error of the vector field (5.30), all averaged over 20 experiments.

The experiment was performed for different grid constants g used to discretized the continuous domain Ω into $\widehat{\Omega}$, and for different numbers of critical points n_{cp}. For each constellation (n_{cp}, g), the experiment was executed 20 times with randomly created sets of critical points P_{cp}. The results of the experiments are summarized in Table 5.1.

5.5 Conclusion

With an increasing size of the vector field, the distance between distinct critical points increases, therefore, the detection of critical points improves with larger field sizes. The location error $\varepsilon_{\mathrm{loc}}$ averages at about 2 voxels, which is admissible, because in the vector fields obtained by non-rigid registration of medical images (chapter 4), critical points will not appear as points, but are "voluminous" areas. For the same reason, the error in phase portrait recovery $\varepsilon_{\mathrm{pp}}$ is acceptable. The eigenvectors and eigenvalues, calculated from these phase portraits, may only be used as a qualitative measure classifying the critical point (see Fig. 5.1). Quantitative implications about a critical point should not be drawn based on its phase portrait, since in the application case, (5.5) does model the vicinity of a critical point only poorly. Clusters, as obtained in the clustering step (section 5.4), may also be used as shape descriptions of critical areas.

Chapter 6

Visualization

Visualization is the final link of the time series image analysis tool chain described. The steps that are necessary to prepare anatomical data for visualization will be introduced, as well as its presentation in conjunction with the results of the preceding analysis.

6.1 A Brief Note About the Implementation

A proper visualization provides results of the time series image analysis in a human readable form. A variety of software toolkits is available to visualize 3D data [5, 61, 96]. The implementation used here utilizes the OpenGL application programming interface (cf. [98, 122]), since it is independent of the operating system, and with MESA [83] a compatible free implementation is available. Also, available graphics hardware can be utilized for fast rendering. Surface meshes often consist of 100.000 or more triangles, so hardware acceleration of the 3D rendering becomes mandatory for an interactive visualization tool.

6.2 Preparing Anatomical Data for Visualization

To visualize the shape change of anatomical data, knowledge about the geometry of the examined objects, the skull and the brain, is necessary. Therefore, surface based rendering will be used. This requires the extraction of surface meshes from the 3D medical images. Different approaches are used to extract the skull from the CT images, and to extract the gray and white matter from MR images.

In CT images bone is mapped to high intensities [63], while soft tissue is mapped to low intensities. Hence, it is possible to segment the bone from the images by thresholding with a certain threshold t. By using this threshold t, the surface of the skull can be extracted from the image data as iso-surface triangle mesh, by using the *marching tetrahedra* algorithm [80]. Then, the mesh is optimized to reduce its triangles count, without loosing geometric detail [60, 70].

To extract surfaces of white and gray matter from MR images, a three step procedure is employed. First, intensity inhomogeneities in the images are corrected by a modification of the *adaptive fuzzy C-means algorithm* [85], yielding an intensity-corrected version of the input image and a segmentation into three classes: background, gray matter and white matter. Then, based on the manual selection of the *posterior commisure*, the cerebellum and the brainstem is removed from the brain, yielding an approximation of the white matter. A surface mesh of this white matter approximation is extracted and optimized like described above. Finally, by using an iso-value that corresponds to the boundary between gray matter and CSF, the surface mesh is deformed in order to adapt to this boundary, and to form the grey matter surface [65]. In an equivalent manner, the approximate mesh is adapted to form the surface of the boundary between the white matter and the gray matter by using an appropriate iso-value.

When anatomical data is visualized, transparency might be used to overlay different states of the objects on the time course. Moreover, a color scheme is be used to visualize shape change: At each point of the surface, the scalar product of the surface normal with the (non-rigid) deformation field is evaluated. If the value of the scalar product is greater then zero, the surface is colored blue, indicating a shift in normal direction, if the value is less then zero, the surface is colored red, indicating a shift against the direction of the surface normal. The color intensity corresponds to the absolute value of the scalar product, indicating the magnitude of shape change in surface normal direction. The corresponding color scale is given in mm (e.g., Fig. 7.4, page 54). By changing the color scale, it is possible to focus on large deformations or to give an impression of the all-over shape change at low scales. Additionally, arrows can be displayed to illustrate the shape change, originating at the surface and with the size and direction corresponding to the vector field value (Fig. 7.4, page 54).

6.3 Critical Points

The method to visualize critical points is two-fold. As described in the previous section, a critical point can be characterized by its phase portrait, and thus, by the eigenvectors and eigenvalues of this phase portrait. The visualization can then be implemented like follows: By considering only the real part of the eigenvalues and eigenvectors, the eigenvectors are used to spawn an ellipsoid, with the length of the half axis set to the absolute value of the corresponding eigenvector. By color-keying positive eigenvalues with green, negative eigenvalues with red, and imaginary components by mixing the color with a blue component attractors, repellors, saddle points, and rotation centers can be distinguished in the visual representation. Transparency is used to improve the perception of a critical point as a spot with decaying influence on his environment (Fig. 6.1, left).

For the eigenvalues and eigenvectors have a limited scope in describing the critical areas in the application context, a second approach for the visualization of critical points was implemented. The counter values, as obtained during the search for critical points (Section 5.4) can be interpreted as 3D gray scale image. Thus, it is possible to segment critical areas by extracting an iso-surface mesh from the image, as described above. This mesh consists of separate blobs. Each blob corresponds to a critical point (or critical area) and is colored similar to the scheme given for anatomical surface meshes; but instead of the red-blue color coding, a red-green one is used. The color intensity is always set to the highest intensity. Therefore, a red blob corresponds to an attractor, a green blob corresponds to a repellor, and saddle points consist of a mix of green and red (Fig. 6.1, right). Unfortunately, it is not possible to represent rotation centers with this scheme.

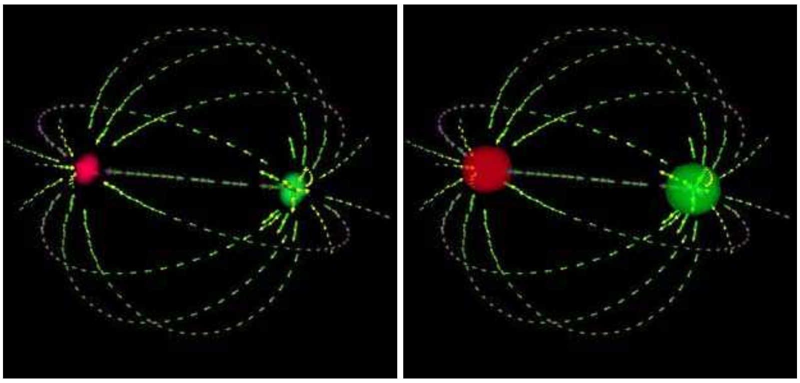

Figure 6.1: Visualization of critical points and the corresponding vector field. Critical points can be visualized by ellipsoids, corresponding to eigenvectors and eigenvalues of their phase portrait (left) or as colored blobs (right). The green color indicates repelling, and the red color attracting properties. Additionally, the vector field is visualized by stream lines of arrow shape icons.

6.4 The Vector Field

The vector field, as obtained by non-rigid registration, can be seen as a snapshot of a dynamical system describing the flow of matter. A number of sophisticated methods for flow field visualization have been proposed including particle tracing [58, 72, 113], icon based methods [33, 89], and texture based approaches [18, 29, 32, 39, 101]. With still images, stream lines can be used to visualize the topology of a vector-field. The environment of critical points can be used as seed points for trajectory tracing. The stream lines are estimated by integrating along the vector field, forward, or backward, depending on the sign of the eigenvalues of the critical point. To include directional information, the stream lines are represented as chains of arrow shape icons, with a size corresponding to the vector field magnitude (Fig. 6.1).

Chapter 7

Application

This chapter focuses on the application of the tool chain to time series medical image data. Revising the tool chain used to analyze MR-data, results are shown that were obtained by analyzing three sample data sets of patients with a different clinical indication. In a similar manner, CT data is analyzed that was obtained by monitoring the midface distraction osteogenesis.

7.1 Analyzing MR Time Series Data

The MR images analyzed in this section were acquired on two different scanners. A patient suffering from Alzheimer's disease was treated at the Clinic of Psychiatry, University Clinic of Leipzig. Images were acquired at the Department of Radiology, University Clinic of Leipzig, by using a volumetric T_1 weighted MPRAGE sequence on a 1.5 Tesla tomograph (Siemens Vision, time of repetition 11.4 ms, 128 slices, matrix 256×256, voxel size $0.9 \times 0.9 \times 1.5\,\mathrm{mm}$).

The other two image series were obtained during treatment at the Day-Care Clinic of Cognitive Neurology of the University of Leipzig. The Images were acquired on a 3.0 Tesla tomograph (Bruker Medspec 100), with a high-resolution, whole-head 3D T_1-weighted MDEFT sequence [66, 111] (128 sagittal slices, 1.5 mm thickness, FOV $25.0 \times 25.0 \times 19.2\,\mathrm{cm}$, data matrix of 256×256 voxels). The analysis tool chain applied to the images is outlined in Fig. 7.1.

The following color plates illustrate the results of the analysis of patients with the following disease:

- *Alzheimer's disease*: three images were acquired, of which the second image was taken 12 months after the first image, and the last image was taken 32 months after the first one.

- *Middle cerebral artery infarction*: the first image was acquired twelve days after stroke, the second one six months later.

- *Spontaneous intra-cerebral hemorrhage*: the first image was taken after the surgical intervention to remove the blood, the second image ten months later.

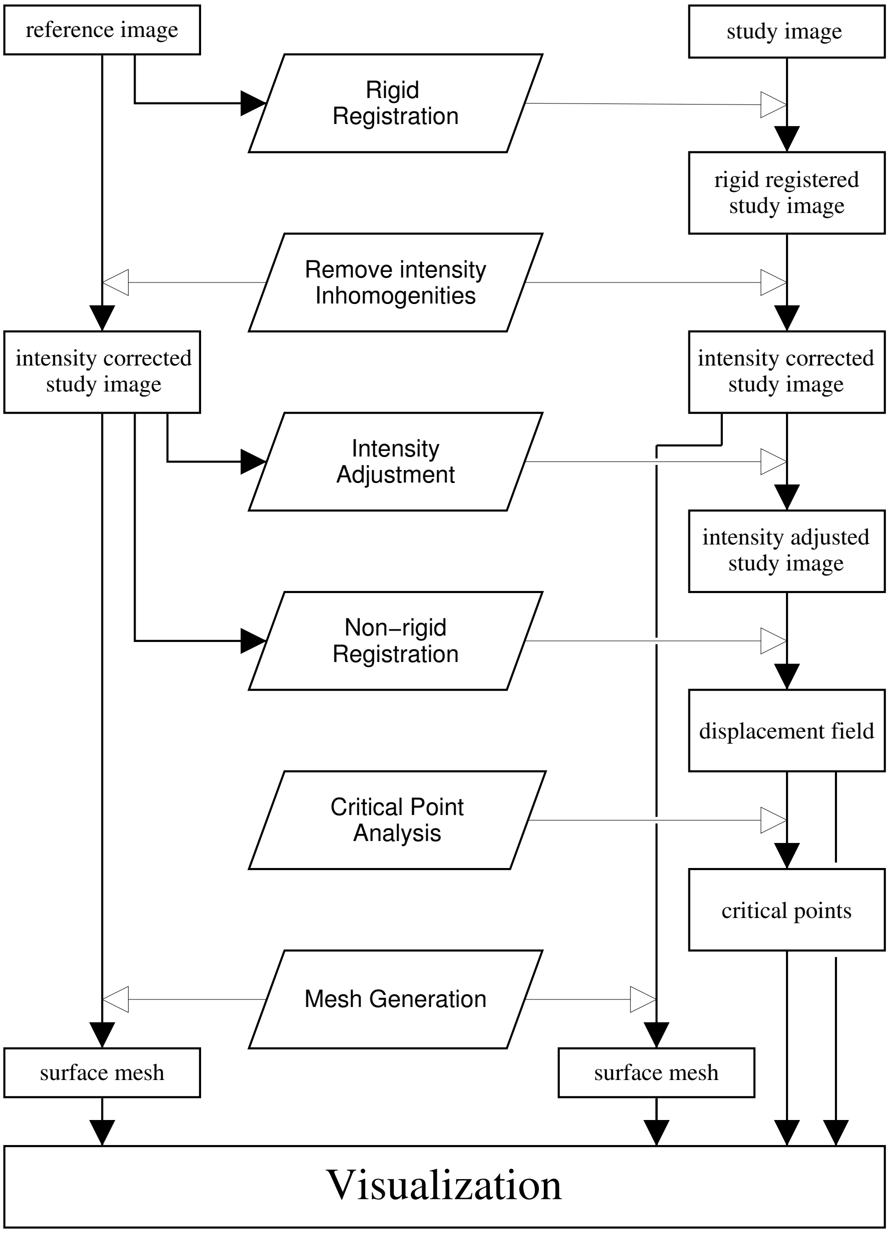
reference image
study image
Rigid Registration
rigid registered study image
Remove intensity Inhomogenities
intensity corrected study image
intensity corrected study image
Intensity Adjustment
intensity adjusted study image
Non−rigid Registration
displacement field
Critical Point Analysis
critical points
Mesh Generation
surface mesh
surface mesh
Visualization

Figure 7.1: Work flow for the analysis of MR time series images. After rigid registration, the intensity inhomogeneities are removed in both images by adaptive fuzzy c-means segmentation, and the further processing is done with these corrected images. Then, the all-over intensity distribution of the study-image is adjusted to the reference image. After non-rigid registration, critical point analysis and mesh generation, finally, the results are visualized.

Monitoring Progression of Alzheimer's Disease

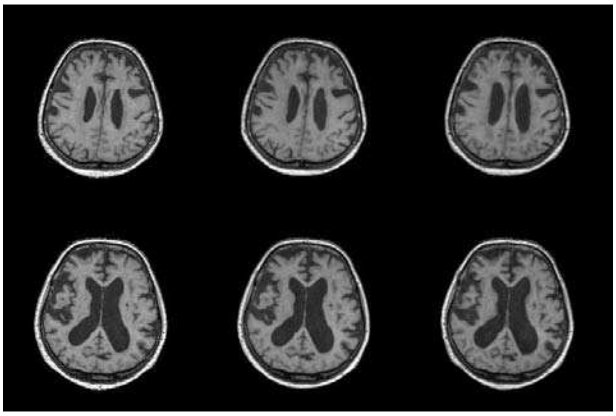

Figure 7.2: (AD) The data of a patient with the clinical indication of Alzheimer's Disease was analyzed. The development of the disease was monitored with three MRT examinations. Example slices are shown from the first examination (left column), the second examination, twelve months later (middle column), and from the third examination, 32 months after the first examination (right column). An enlargement of the inner and outer cisterns is notable.

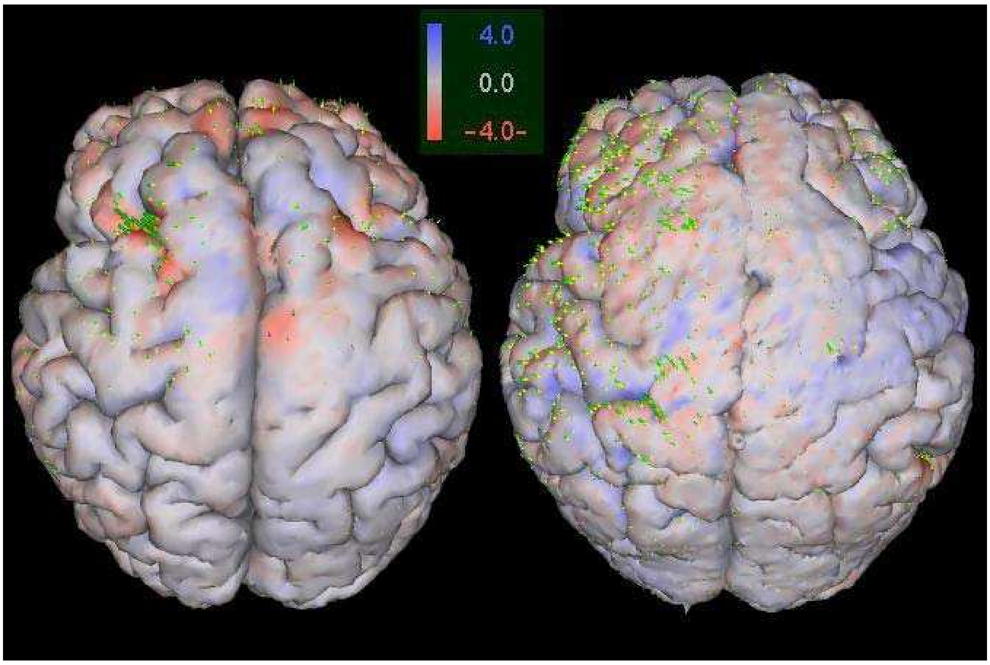

Figure 7.3: (AD) Shape change during progression of the disease; the image on the left resembles the development over the first monitoring interval of twelve month, the image on the right refers to the full 32 months interval. The most prominent change takes place in the frontal lobes.

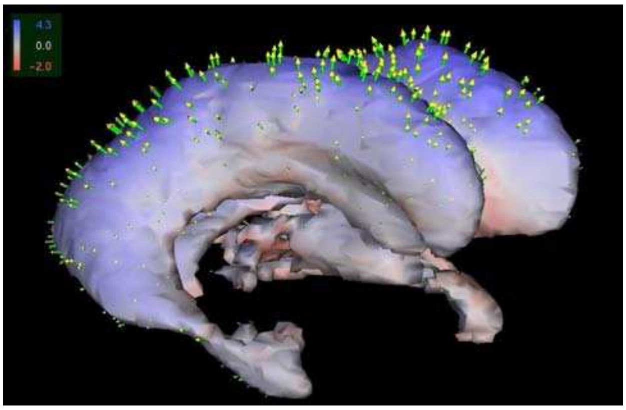

Figure 7.4: (AD) The ventricle at the first examination is shown. The vectors denote the enlargement during the 32 months observation interval. Colors indicate the deformation in the direction of the surface normal. The enlargement of the ventricles is a consequence of a brain tissue loss, resulting in an increase of the inner *cerebrospinal fluid* (CSF) volume. The superior orientation of the enlargement indicates a more profound tissue loss in the supraventricular compartment.

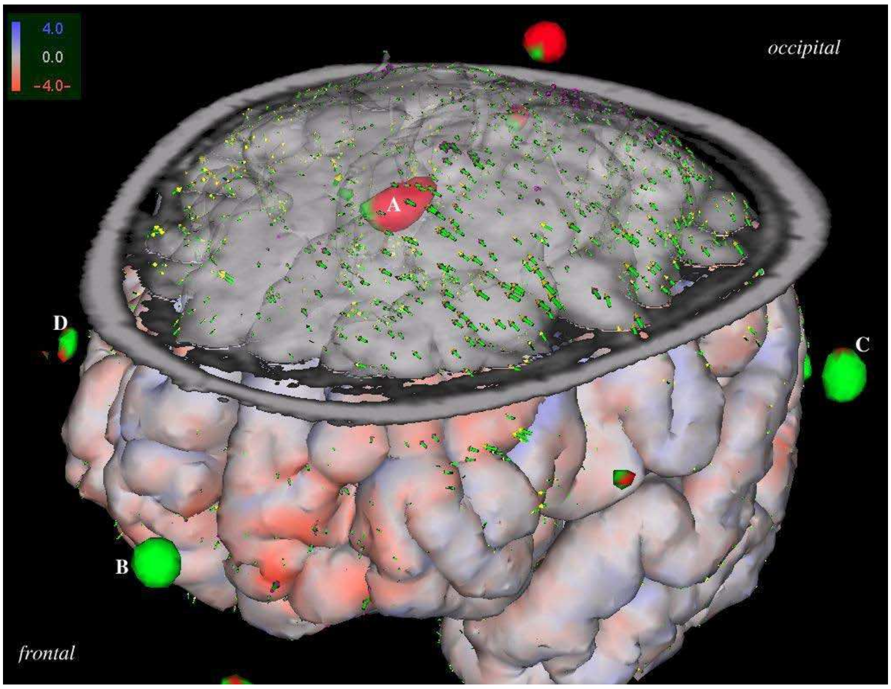

Figure 7.5: (AD) Shape changes during the observation time of 32 month. A large attraction area (A) in posterior portions of the first and second frontal gyrus of the left hemisphere is found. In conjunction with the enlargement of the lateral ventricles in the superior direction (Fig. 7.4), it can be deducted that this is the area with the most prominent matter loss. The repelling areas (B-D) are located in the external CSF. This may be interpreted as an increase of the outer cisterns, indicating a tissue loss of the adjacent gyri.

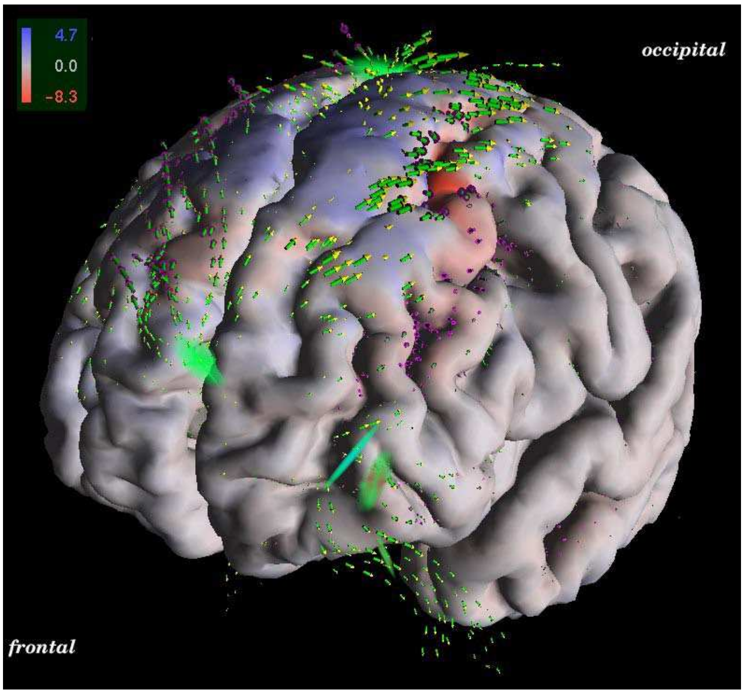

Figure 7.6: (AD) Stream lines map the virtual flow of tissue in the fronto-occipital direction and indicate a retraction of the brain in this direction. Here, critical points are visualized via phase portraits. The repelling area at the frontal pole may be interpreted as an increase of CSF close to the frontal pole that coincidences with a retraction of the brain. This interpretation is supported by the color-coded visualization of the all-over brain shape change.

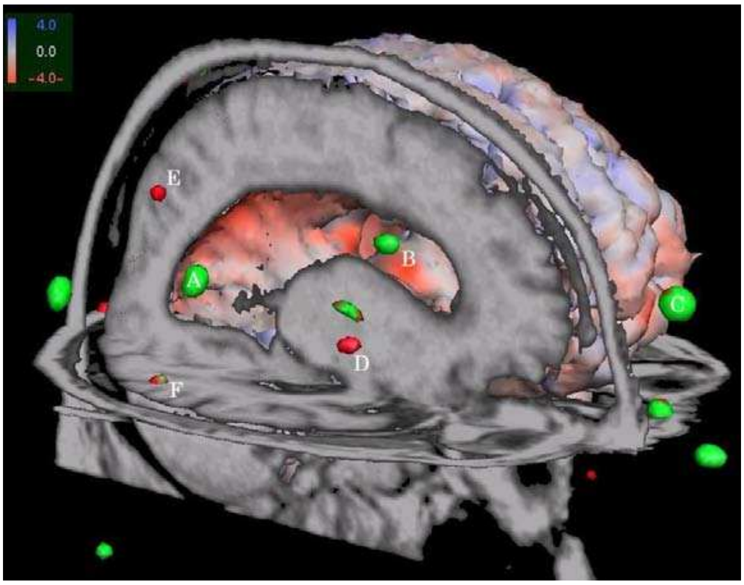

Figure 7.7: (AD) Most notable are the repelling areas in the anterior (B) and posterior (A) part of the right lateral ventricle, and the repellor at the frontal pole (C). All repellors may be interpreted as an increase of CSF coincidenting with the brain atrophy. The attractor near the putamen (D), and in the occipital gyri (E) indicate some center of matter loss. Furthermore, the saddle point near the right angular gyrus (F) indicates another focus of shape change.

Cerebral Infarction

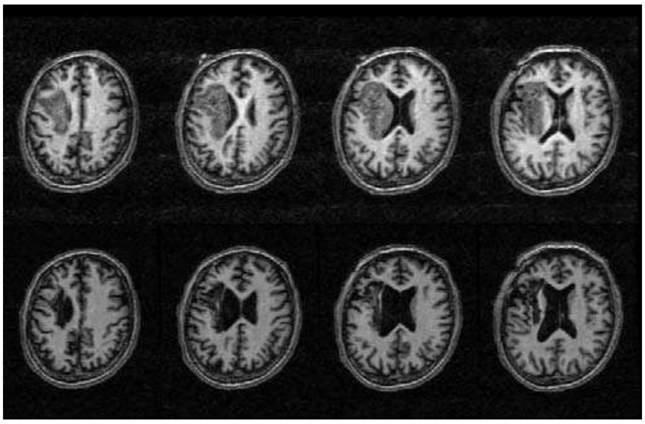

Figure 7.8: (IF) Images of a patient suffering from an incomplete infarction of the middle cerebral artery. The images in the top row were taken after twelve days. Note, the space-occupying effect of the infarction at this early stage. Six months later the edema and tissue were absorbed, leaving a pseudo-cystre necrosis (bottom row).

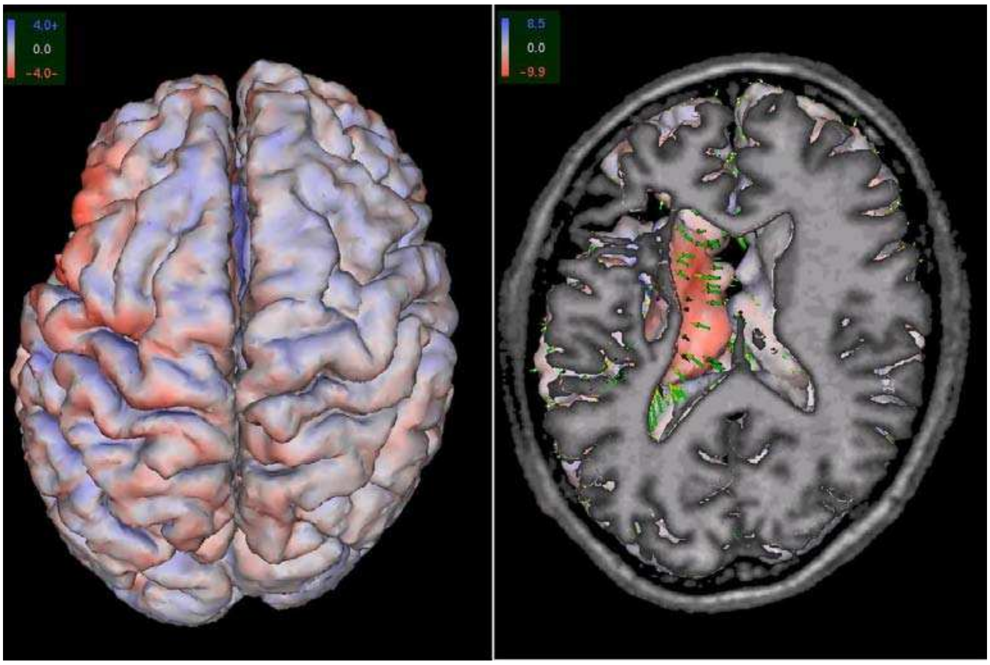

Figure 7.9: (IF) The over-all shape change during the six-months interval is visualized by the vector field. It is very well visible that the shape change is confined to the left hemisphere. Most prominent is the deformation of the left lateral ventricle induced by the edema. The shift of the ventricle boundary is about 10 mm.

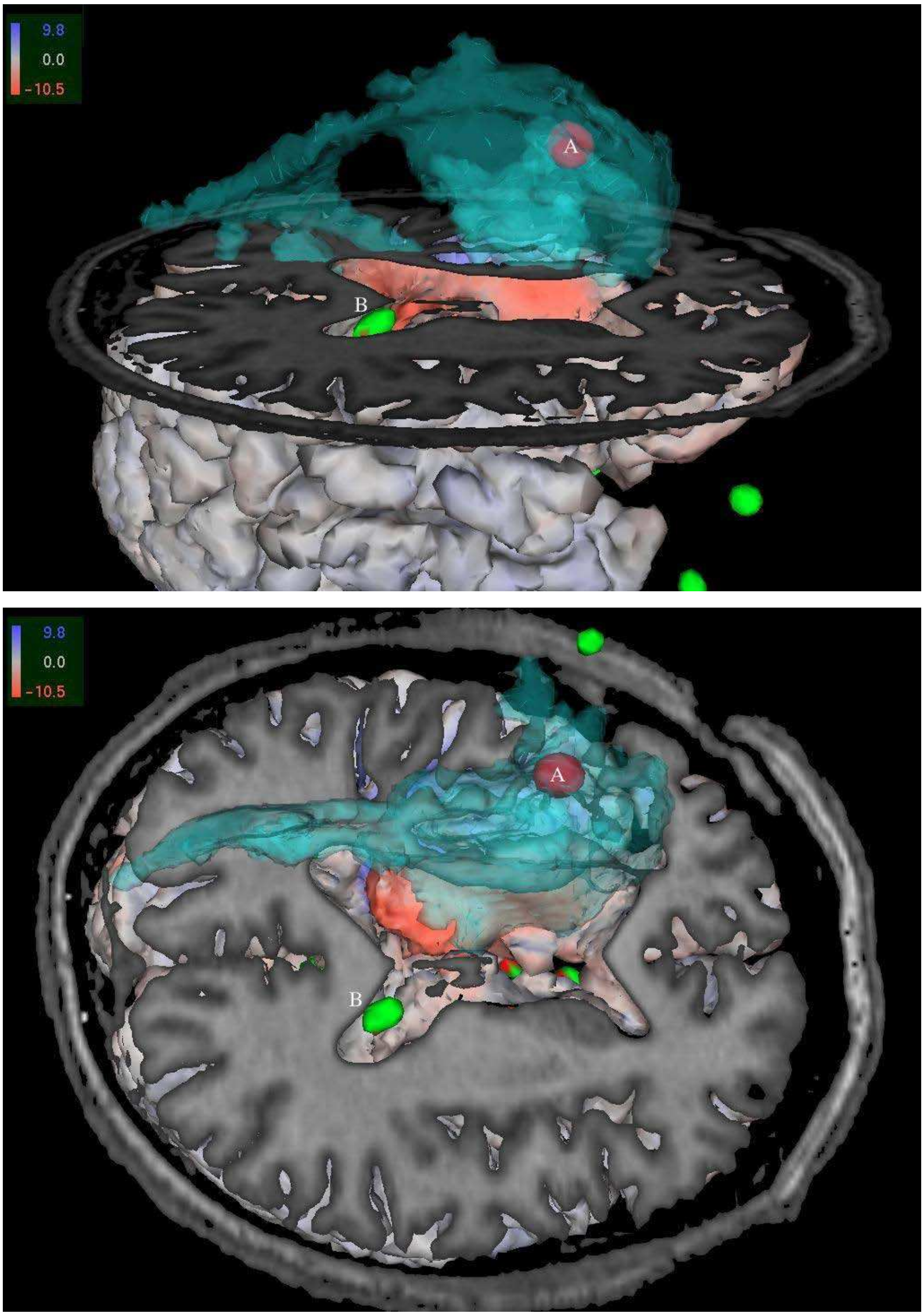

Figure 7.10: (IF) An estimate of the lesion is visualized as a transparent turquoise structure, segmented by methods described elsewhere (Chalopin and Kruggel [20]). The attracting area (A) inside of the lesion can be interpreted as follows: While the edema reduces and damaged tissue is removed from the lesion, the brain is pushed in the direction of the the lesion center; therefore, it appears as attractor. The repellor (B) inside the lateral ventricles indicate an enlargement of the ventricles that coincides with the reducing edema. The other critical points are located outside of the intra cranial space; they are, therefore, of no interest.

Intra-Cerebral Hemorrhage and Intervention

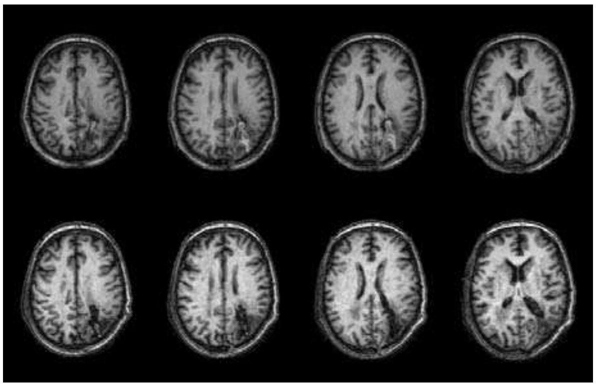

Figure 7.11: (IH) A spontaneous intra-cerebral hemorrhage (cf. Barnett et al. [6]) in the right parietal lobe was removed surgically. The images in the top row show the status shortly after the intervention. Here, remnants of the blood are still visible in the lesion. The images in the bottom row where taken ten months later. During the time after the intervention, necrotic brain tissue and blood were removed.

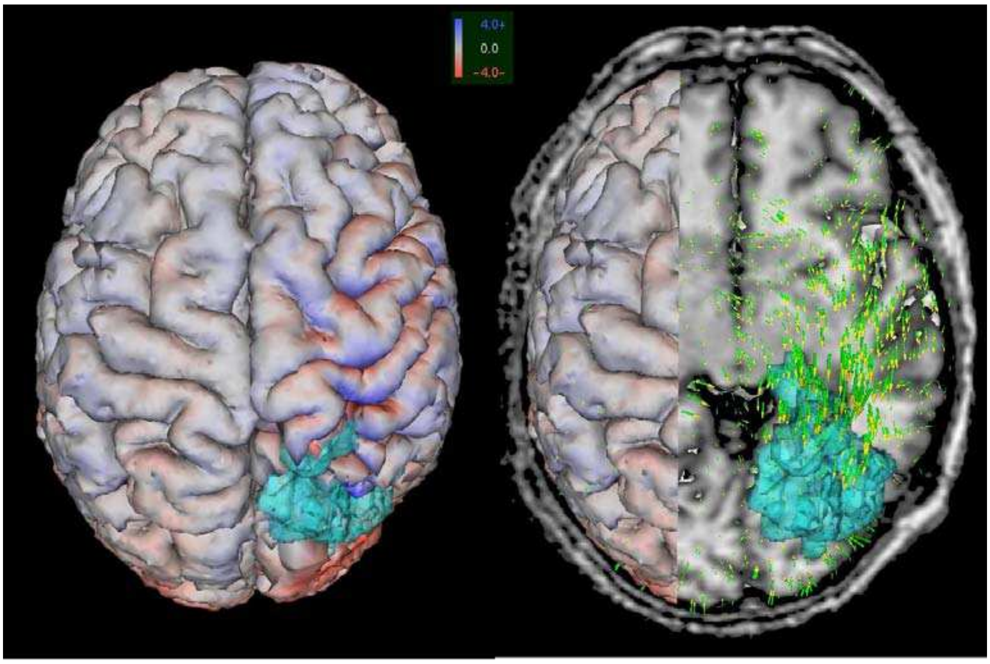

Figure 7.12: (IH) A top view of the deformation pattern is shown. The estimate of the lesion is displayed as a turquoise transparent structure, segmented from the images taken at the second time point with methods described elsewhere (Chalopin and Kruggel [20]). A shift of the brain towards the lesion is visible. The major deformation takes place in the right hemisphere, the left hemisphere remains unchanged.

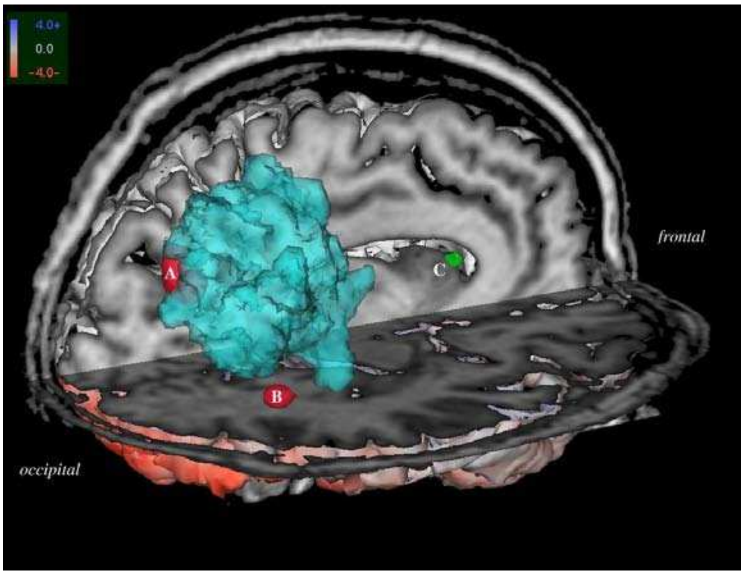

Figure 7.13: (IH) Right view: A large attracting area (A) is located at the boundary of the lesion. Another small attraction area (B) is located near the lesion in the right occipital lobe. Besides these attractor, a repellor (C) can be found in the left lateral ventricle. It indicates an enlargement of the ventricle after the shift of the brain in the direction of the lesion.

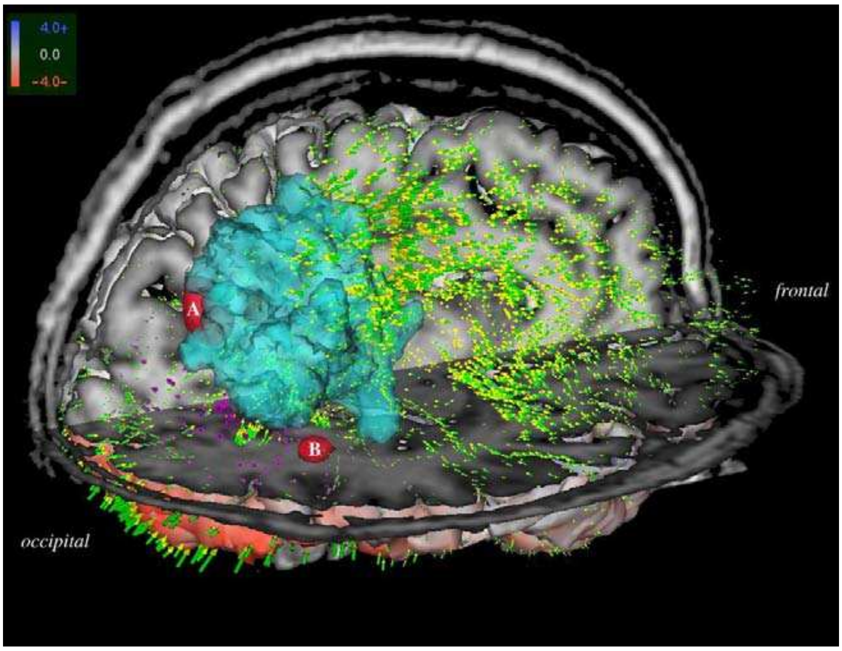

Figure 7.14: (IH) A large attracting area (A) and (B) coincident with the enlargement of the lesion and the simultaneous shift of the right parietal lobe in occipital direction and a shift of the the right occipital lobe in frontal direction.

7.2 Analysis of CT Time Series Data

The tool chain to process the CT image data is outlined in Fig 7.15. The images were acquired at the Department of Radiology of the University of Leipzig (Leipzig, Germany) by using a spiral CT-tomograph (Siemens Volume Zoom plus, 120 kV, collimation 1 mm, slice thickness 2 mm, rotation time 0.75 s, feed/rotation 5.0 mm, matrix 512 × 512, reconstruction increment 1 mm, convolution kernel H50s). To show different aspects of the midfacial distraction osteogenesis, the tool chain was applied to the data of three patients with different treatment planning and treatment outcome. The most notable differences between these patients are that in the first patient the midface was mobilized only partially, in the second patient the distraction was done after an almost complete osteotomy, and in the third patient a high deformability of the whole skull was known beforehand.

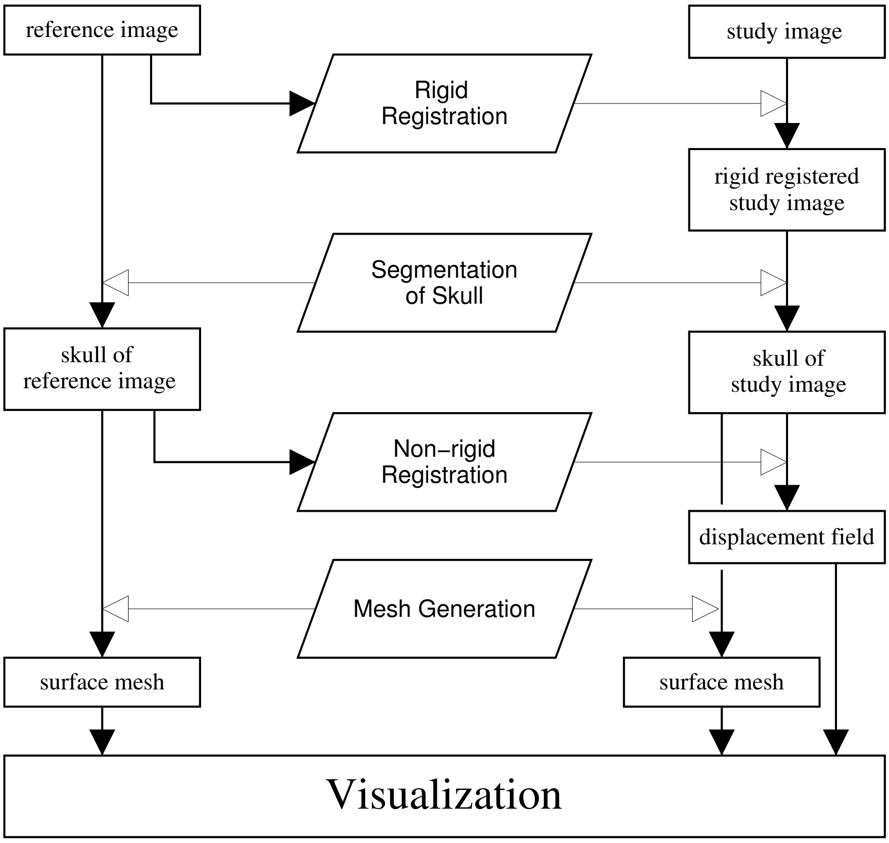
reference image
study image
Rigid Registration
rigid registered study image
Segmentation of Skull
skull of reference image
skull of study image
Non−rigid Registration
displacement field
Mesh Generation
surface mesh
surface mesh
Visualization

Figure 7.15: Work flow of the analysis of CT images. With CT images, the Hounsfield scale offers a normalization of the intensity range, therefore, intensity adaption is not necessary. In the application to distraction osteogenesis image data, the deformation of the skull is of special interest. Therefore, it is segmented from the images prior to non-rigid registration.

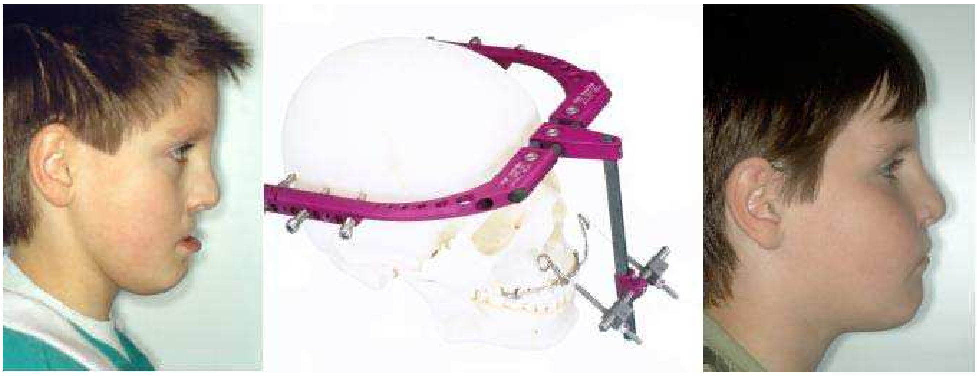

(a) First patient, before (left) and after distraction (right), model skull to adjust RED system (middle)

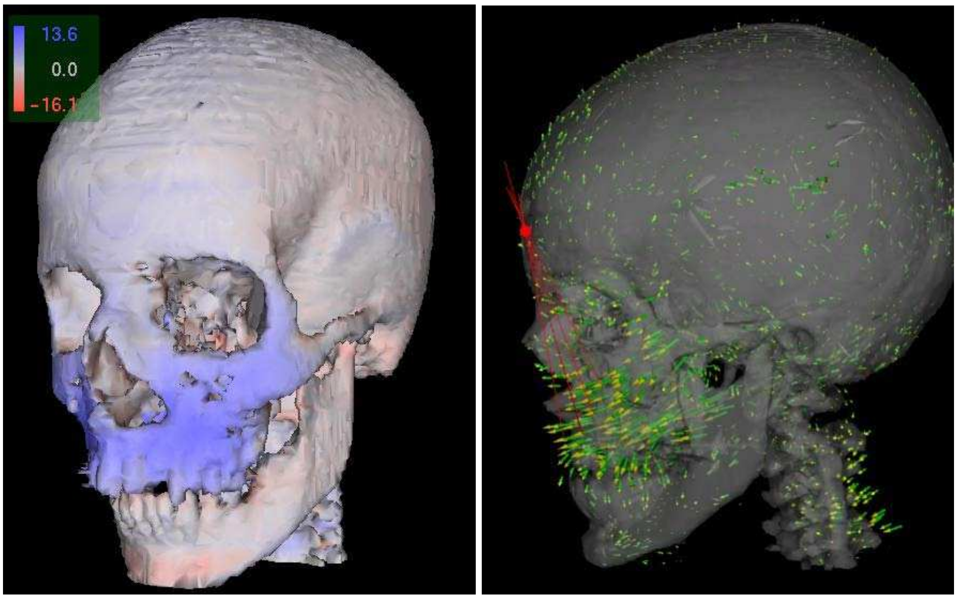

(b) shape change

(c) manually extracted rotation center

Figure 7.16: A 12-year-old boy was suffering from a severe midfacial hypoplasia, resulting from a bilateral cleft lip and palate (a, left). He was treated by way of a sutural midfacial distraction osteogenesis with simultaneous transversal maxillary expansion, guided by a RED system for 10 weeks. The treatment resulted in a 17 mm forward displacement of the midface with an (intended) back slide of 2 mm later on (a, right). The retrospectively performed analysis indicated that the distraction triggered a forward shift of the zygomatic and nasal bones since the maxilla was not mobilized (b). Furthermore, the center of rotation which is dependent on the center of resistance and the point of applied force could be determined manually (c); its location is important in treatment planning and outcome, and was selected properly in this case.

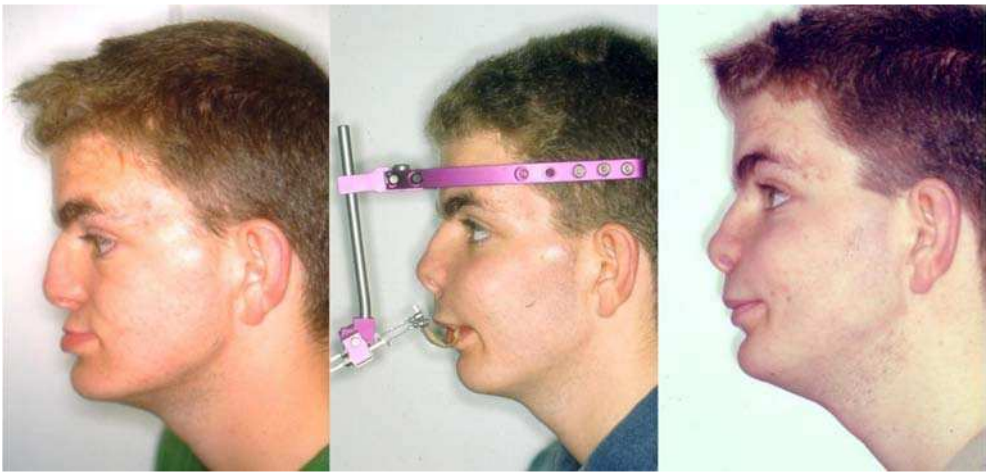

(a) Second patient, before (left), during (middle), and after distraction (right)

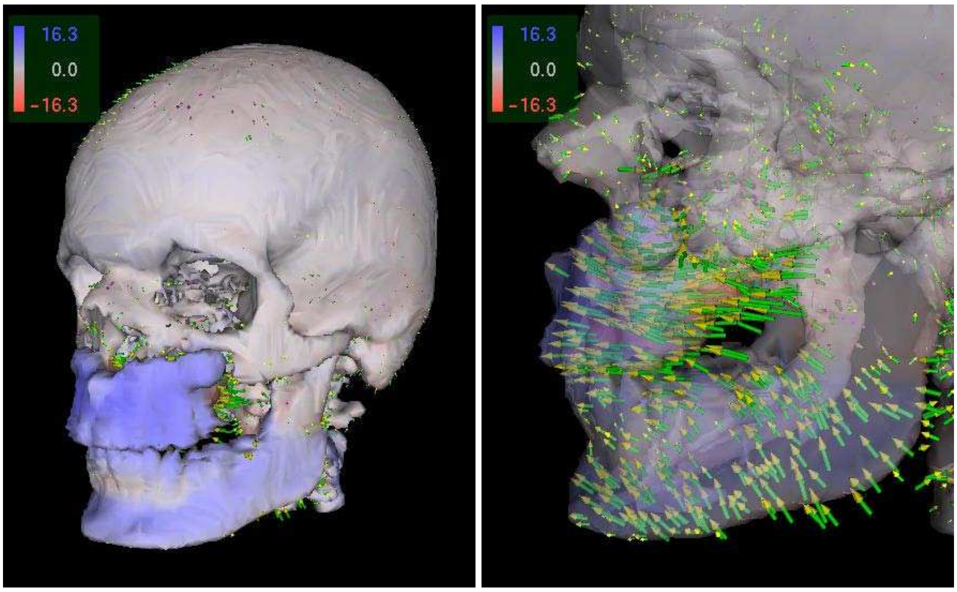

(b) Shape change of the whole skull

(c) Shift of the occlusal plane

Figure 7.17: An 18-year-old boy with an isolated non-syndromatic midfacial hypoplasia. Distraction after an almost complete osteotomy led to a harmonic maxillo-mandibular relationship and improved esthetics (a). Utilizing the visualization tools showed the complex interrelated changes, caused by the forward displacement. In this case the zygomatic bones were not influenced by the distraction (b). A straight anterior movement parallel to the occlusal plane is evident (c)

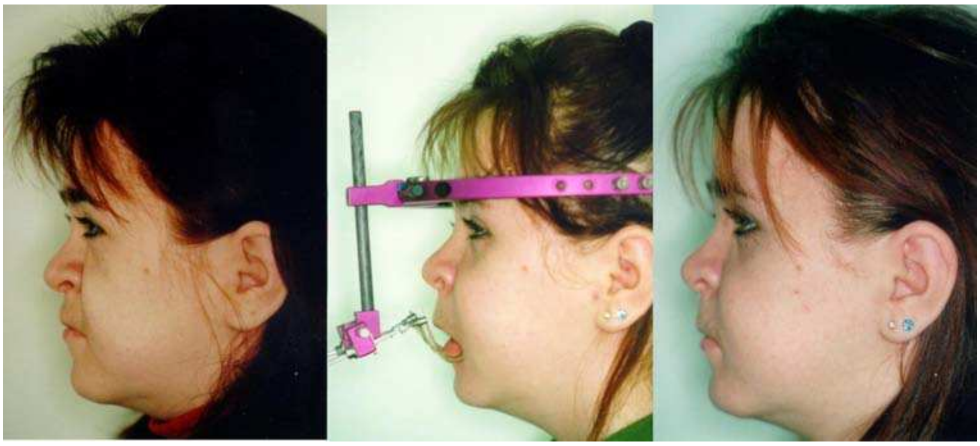

(a) Third patient, before (left), during (middle), and after distraction (right)

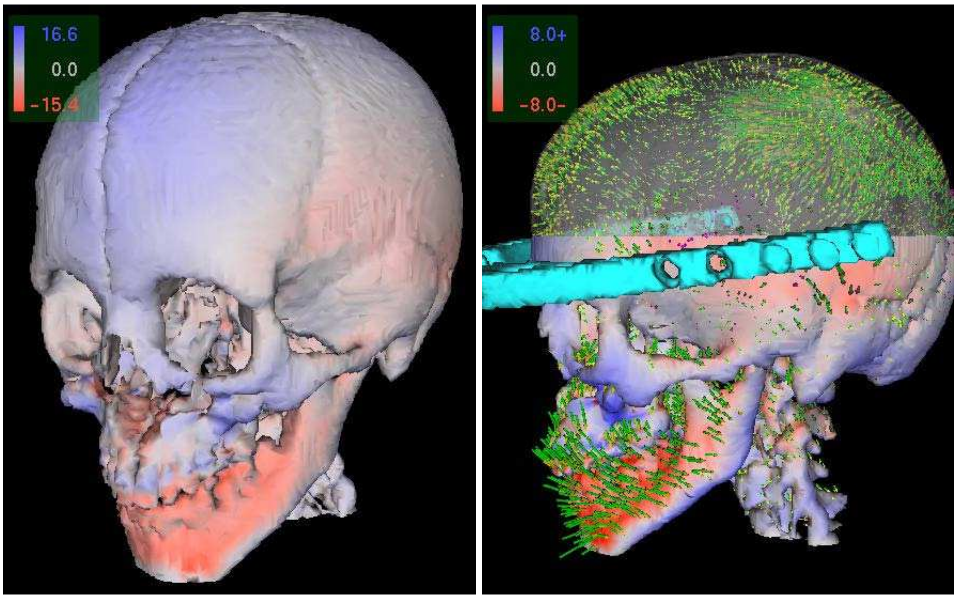

(b) All-over shape-change

(c) Strong deformation of the whole skull

Figure 7.18: An 18-year-old girl, was suffering from a severe midface hypoplasia and retrognathia (a). A malfunction of bone mineralization as well as partially open sutures yielded a high skull deformability (b). This led to an impressive deformation of the whole skull induced by the halo fixation of the RED system (c). The analysis of deformation strength and location yielded important information for the design and placement of the halo-frame, anchoring the distractor.

Chapter 8

Discussion

This chapter summarizes results and outlines problems that arose during the processing of the application data. A discussion of possible enhancements in time series image analysis concludes this chapter.

8.1 Achievements and Limitations

An implementation of the core tools developed here were published under the terms of the GNU General Public License [119], including software for automatic intensity adjustment, for non-rigid registration, for the critical point analysis, and a visualization tool. With these tools it is now possible, to analyze the differences between pairs of serially acquired medical images on standard PC hardware in a reasonable amount of time. From the applications shown in the preceding chapter it is evident that the principal results coincide with the expectation of the monitored therapy processes.

Nevertheless, some problems arose during the application of the tools to time series images: First of all, the validity of applying rigid registration is limited. The images considered here exhibit a shape change. In section 3.1, it was already argued that this renders landmark based registration unstable. However, shape changes also influence the voxel based approaches, since the cost functions used in these approaches are also sensible to shape change. They minimize the selected criterion over the whole image domain. Especially in the case of the midface distraction osteogenesis, where the skull changes to a large amount in the facial area, this minimum might not lead to a registration of the area with the least changes, the cranium. Instead, registration will be achieved slightly off-shape. The positioning of the head may also change the spatial relation between organs. In the case of the datasets obtained monitoring the midface distraction osteogenesis, e.g., the angle between neck and skull changes. This can be seen as a non-rigid deformation of the neck in the corresponding visualization (Fig. 7.16, 7.17, and 7.18)). The error of rigid registration induced by such non-rigid changes has to be quantified.

Problems of the intensity adjustment were already discussed in section 3.2. However, in cases where intensity inhomogeneities are present in the images, and approaches to remove such inhomogeneities fail, intensity adjustments will yield an inconsistent intensity-material-mapping in time series images. Non-rigid registration then yields incorrect results. In some cases, the errors might be subtle, offering room for erroneous conclusions (Fig. 8.1).

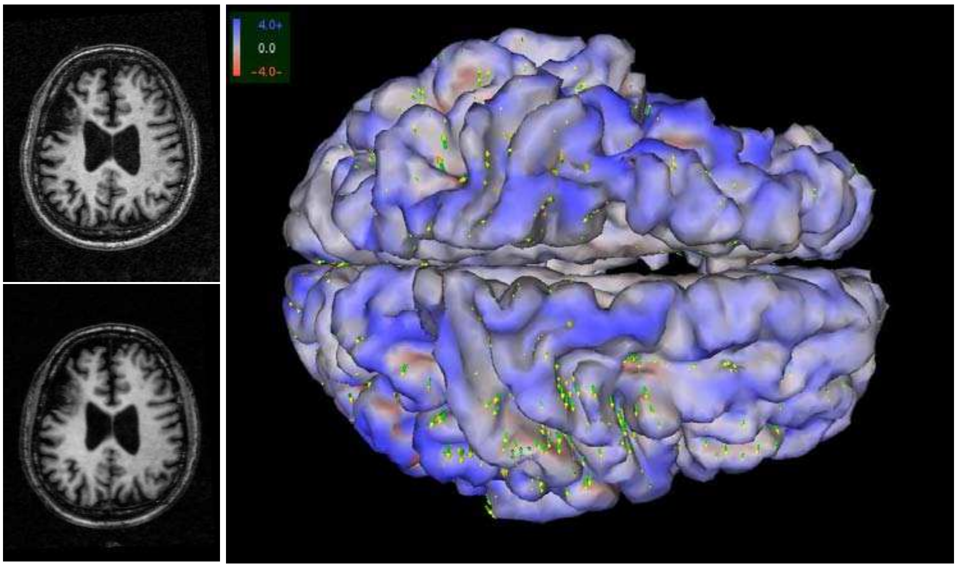

Figure 8.1: The right image shows the result of the registration two images, study (left upper) and reference (left lower). Since the intensities of the gray matter in both images are not well adapted, the non-rigid registration, based on the sum of squared differences, yields a vector field which suggests a major increase of the brain volume that can not be found in the original images. Apparently, the cost function was favoring a registration of the gray matter in the study image to the white matter in the reference image.

Therefore, using the sum of squared differences as a cost function for non-rigid registration, is deprecated in the case of time series MR images. Especially, since the computer technique is developing very fast, the computational load of more complex voxel similarity measures may become acceptable.

Another problem of non-rigid registration based on fluid dynamics is introduced by its main advantage: it is capable of handling large deformations. Therefore, it also tends to misregister, if structures are present in one image which are not present in the other. Consider, the pair of study image and reference image given in Fig. 8.2. A part of the scalp is missing in the study image 8.2 (a) which is present in the reference image 8.2 (b). Parts of the cerebellum where registered to the scalp (Fig. 8.2 (c)).

To overcome such limitations, it might be useful to combine voxel based approaches with landmarks to restrict the transformation at certain points.

Besides the errors in non-rigid registration, an ambiguity in the registration results is also introduced by selecting the method to be used for the registration and by the multi-resolution processing of the image data. In Chapter 4, several approaches for non-rigid registration were discussed. Even though all these methods may find a mapping that ideally maps homologous structures onto each other, they will not yield identical transformations. Bro-Nielsen and Gramkov [14] showed that Thirion's algorithm [107] yields a deformation that is different

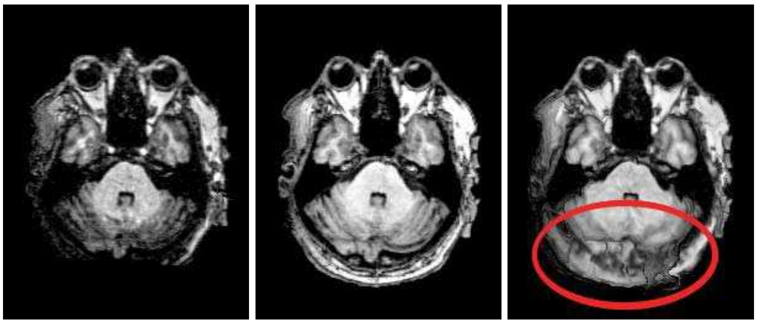

(a) study (b) reference (c) registration result

Figure 8.2: In the study image a part of the scalp is missing (a) which exists in the reference image (b). The registration maps parts of the cerebellum to the scalp yielding a mis-registration (c)

.

from the deformation obtained by using the filter-based fluid dynamics approach. However, it exists no mathematical measure to decide which result is better in modeling the physical reality.

In Chapter 4, support was given for Christensen's approach [23]. In most cases, the method yields acceptable results for non-rigid registration. However, ambiguity is introduced into the results through the multi-resolution processing. Consider a registration experiment with a study image (Fig. 8.3 upper row, left), and a reference image (Fig. 8.3 upper row, middle) by using different starting resolutions. Results with start sizes 8×8 and 16×16 might intuitively be favored, since they coincide more with the expectation of a smooth deformation. Nevertheless, in terms of the cost function and the smoothing term in (2.9), all registration results are very good. Therefore, a decision about the transformation can not be drawn on the basis of methodical considerations only.

Another problem arises from the fact that critical points of deformation fields are not infinitesimally small. It was already discussed that the phase portrait allows a classifying a critical point, but does not yield a quantitative measure. The absolute values of the phase portrait's eigenvalues are strongly dependent on the formula used to model the environment of a critical point. On the other hand, the appearance of the blob representation of a critical point is dependent on the iso-value used for surface extraction (section 6.3). High iso-values will emphasize attractors and repellors with strong focal properties, and low iso-values will give a better impression of the shape of the critical area. The visualization of critical areas as blobs is preferable, because it preserves more information. Since rotation can not be encoded with this visualization scheme, models have to be found that provide a better visualization the qualitative features of critical points.

It has to be noted that the level of visualization detail is usually not sufficient for a concise analysis of the monitored process. In the case of the distraction osteogenesis, the generated surface meshes are sufficient to visualize the all-over shape change, but the localization of landmarks in the images, and therefore, a measurement of deformations at such landmarks is

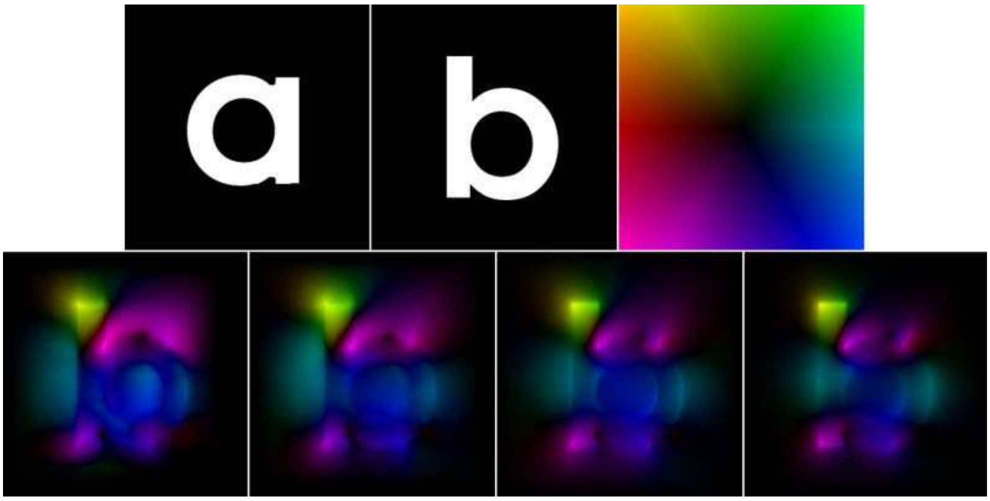

Figure 8.3: Registration of source image (letter **a**) to the reference image (letter **b**) by using different start sizes for the multi-resolution processing. The results are visualized in the lower row by using the following coloring scheme: The deforming vectors (x,y) are transformed to polat coordinates (ϕ,r). ϕ is then represented by a color value according to the scheme (upper row, right), and r is represented by the color intensity. The results are given from left to right for multi-resolution start sizes of 16×16, 32×32, 128×128 and registration of the full resolution of 256×256 only.

very difficult. Here, a more sophisticated segmentation of the skull including artifact removal, is needed.

Besides the methodical problems discussed above, physiological effects have to be considered. The state of body hydration, for instance, may influence the shape of the brain and this influence may change with the examination daytime and with the age of the patient. So far, an investigation has not been performed to measure the magnitude of these physiological effects. Therefore, the measurements of small changes, as they obtained in monitoring slowly atrophying processes has to be interpreted with care.

8.2 Outlook

Several steps are considered as future work on time series image analysis.

First of all, work has to be done to validate the results of the non-rigid registration. Different approaches may be considered here. A validation by using landmarks is possible. Here, it is not necessary to use an extensive set of landmarks, since it only has to be tested how well landmarks are matched by the voxel based registration.

Cross-validation of the fluid-dynamics based registration approach with other approaches is necessary. Vector fields, obtained by different registration methods, will differ. Nevertheless, the shape registration should still be consistent as long as the registration method is able to handle the magnitude of deformation. This kind of cross-validation might help to define application areas for the different methods. If only small deformations are expected, a linear elastic approach might be more appropriate than a fluid dynamic approach. Furthermore, by segmenting structures of the brain and by introducing material parameters the the consistence of the non-rigid registration with the physical reality will be improved.

Another goal is the reduction of the computing time of the analysis tools. A fast quantification of differences between time series images is useful for, e.g., navigation during neurosurgery: When the skull is opened, CSF drains, and the brain deforms due to gravity. This "brain shift" invalidates pre-operatively acquired images (e.g., functional images localizing motor and speech areas). By acquiring images at the beginning and during neuro-surgery, a blue-print of the "brain shift" is available, and with an adequate analysis, the changes could be applied to the pre-operative data used for operation planning in real time. Thereby, the surgeon would get an updated view of the brain including the information available at the time of the operation planning.

Furthermore, the critical point detection needs revision. As can be seen from the analysis of the distraction osteogenesis, rotation centers play a major role during operation planning. Therefore, an automatic detection of this rotation center is of high interest for improving the retrospective analysis of the intervention.

Finally, the feedback from medical experts is very important to discuss results. The establishment of closer links between research and clinical application is necessary in order to improve the applicability of time series medical image analysis in the future.

Appendix A

Mathematics

A.1 Derivation of Euler Step

The relation between velocity field **v** and displacement field **u** can be obtained as follows [23]:

$$\mathbf{u}(\mathbf{x},t) = \mathbf{x} - \mathbf{x}_0, \tag{A.1}$$

$$\mathbf{v}(\mathbf{x},t) = \dot{\mathbf{x}} = \frac{\partial \mathbf{x}}{\partial t}, \tag{A.2}$$

$$\mathbf{v}(\mathbf{x},t) = \frac{\partial(\mathbf{x}_0 + \mathbf{u}(\mathbf{x},t))}{\partial t}, \tag{A.3}$$

$$\mathbf{v}(\mathbf{x},t) = \frac{\partial \mathbf{u}(\mathbf{x},t)}{\partial t} + \nabla\mathbf{u}(\mathbf{x},t)\mathbf{v}(\mathbf{x},t). \tag{A.4}$$

Introducing a time step Δt an update $\Delta\mathbf{u}(\mathbf{x})$ for the displacement is given as

$$\mathbf{u}(\mathbf{x},t+\Delta t) = \mathbf{u}(\mathbf{x},t) + \Delta t\left[\mathbf{v}(\mathbf{x},t) - \nabla\mathbf{u}(\mathbf{x},t)\mathbf{v}(\mathbf{x},t)\right]. \tag{A.5}$$

A.2 Discretization of the Navier-Stokes Equation

$$\mu\nabla^2\mathbf{v} + (\mu+\lambda)\nabla(\nabla\cdot\mathbf{v}) = -\mathbf{f} \tag{A.6}$$

$$\mu\left(\frac{\partial^2}{\partial x^2} + \frac{\partial^2}{\partial y^2} + \frac{\partial^2}{\partial z^2}\right)\mathbf{v} + (\mu+\lambda)\begin{pmatrix} \frac{\partial^2}{\partial x^2} & \frac{\partial^2}{\partial x\partial y} & \frac{\partial^2}{\partial x\partial z} \\ \frac{\partial^2}{\partial x\partial y} & \frac{\partial^2}{\partial y^2} & \frac{\partial^2}{\partial y\partial z} \\ \frac{\partial^2}{\partial x\partial z} & \frac{\partial^2}{\partial y\partial z} & \frac{\partial^2}{\partial z^2} \end{pmatrix}\mathbf{v} = -\mathbf{f}, \tag{A.7}$$

For the x-component of (A.7) we may write:

$$\mu\left(\frac{\partial^2}{\partial x^2} + \frac{\partial^2}{\partial y^2} + \frac{\partial^2}{\partial z^2}\right)v^{(x)} + (\mu+\lambda)\left(\frac{\partial^2}{\partial x^2} + \frac{\partial^2 v^{(y)}}{\partial x\partial y} + \frac{\partial^2 v^{(z)}}{\partial x\partial z}\right) = -f^{(x)}, \tag{A.8}$$

$$(2\mu+\lambda)\frac{\partial^2 v^{(x)}}{\partial x^2}+\mu\left(\frac{\partial^2 v^{(x)}}{\partial y^2}+\frac{\partial^2 v^{(x)}}{\partial z^2}\right)+(\mu+\lambda)\left(\frac{\partial^2 v^{(y)}}{\partial x\partial y}+\frac{\partial^2 v^{(z)}}{\partial x\partial z}\right)=-f^{(x)}. \tag{A.9}$$

Discretizing this using a finite difference scheme using numerical derivatives [90] yields

$$\begin{array}{ll}
\frac{(2\mu+\lambda)}{h^2}\left(v^{(x)}_{i+1,j,k}+v^{(x)}_{i-1,j,k}-2v^{(x)}_{i,j,k}\right) & + \\
\frac{\mu}{h^2}\left(v^{(x)}_{i,j+1,k}+v^{(x)}_{i,j-1,k}-2v^{(x)}_{i,j,k}+v^{(x)}_{i,j,k+1}+v^{(x)}_{i-1,j,k-1}-2v^{(x)}_{i,j,k}\right) & + \\
\frac{(\mu+\lambda)}{4h^2}\left(v^{(y)}_{i+1,j+1,k}-v^{(y)}_{i-1,j+1,k}+v^{(y)}_{i-1,j-1,k}-v^{(y)}_{i+1,j-1,k}\right) & + \\
\frac{(\mu+\lambda)}{4h^2}\left(v^{(z)}_{i+1,j,k+1}-v^{(z)}_{i-1,j,k-1}+v^{(z)}_{i-1,j,k-1}-v^{(z)}_{i+1,j,k-1}\right) & =-f^{(x)}
\end{array}. \tag{A.10}$$

With shortcuts $a=\frac{\mu}{h^2}$, $b=\frac{\mu+\lambda}{h^2}$ follows,

$$\begin{array}{ll}
v^{(x)}_{i,j,k}+\frac{(a+b)}{(6a+2b)}\left(v^{(x)}_{i+1,j,k}+v^{(x)}_{i-1,j,k}\right) & + \\
\frac{b}{(6a+2b)}\left(v^{(x)}_{i,j+1,k}+v^{(x)}_{i,j-1,k}+v^{(x)}_{i,j,k+1}+v^{(x)}_{i-1,j,k-1}\right) & + \\
\frac{b}{4(6a+2b)}\left(v^{(y)}_{i+1,j+1,k}-v^{(y)}_{i+1,j-1,k}+v^{(y)}_{i-1,j-1,k}-v^{(y)}_{i+1,j-1,k}\right) & + \\
\frac{b}{4(6a+2b)}\left(v^{(z)}_{i+1,j,k+1}-v^{(z)}_{i-1,j,k-1}+v^{(z)}_{i-1,j,k-1}-v^{(z)}_{i+1,j,k-1}\right) & =\frac{1}{(6a+2b)}f^{(x)}
\end{array}. \tag{A.11}$$

y- and z- components can be obtained in a similar manner.

With $\hat{\mathbf{f}}:=\frac{1}{(6a+2b)}\mathbf{f}$, writing (A.6) in its discretized representation yields a linear system

$$\mathbf{A}\mathbf{v}=\hat{\mathbf{f}}. \tag{A.12}$$

A.3 SOR Update

Substituting $c=\frac{a+b}{6a+2b}$, $d=\frac{a}{6a+2b}$, $e=\frac{b}{4(6a+2b)}$ we obtain:

$$\begin{array}{rl}
\mathbf{p}_x= & \hat{\mathbf{f}}_{i,j,k,x}+c\left(\mathbf{v}^{(m+1)}_{i-1,j,k.x}+\mathbf{v}^{(m)}_{i+1,j,k,x}\right)+ \\
 & d\left(\mathbf{v}^{(m+1)}_{i,j-1,k,x}+\mathbf{v}^{(m)}_{i,j+1,k,x}+\mathbf{v}^{(m+1)}_{i,j,k-1,x}+\mathbf{v}^{(m)}_{i,j,k+1,x}\right)
\end{array} \tag{A.13}$$

$\mathbf{p}_y$ and $\mathbf{p}_z$ are given similar.

Furthermore, it can be written

$$\begin{array}{ll}
q_x=e & \left(\mathbf{v}^{(m+1)}_{i-1,j-1,k,y}+\mathbf{v}^{(m)}_{i+1,j+1,k,y}-\mathbf{v}^{(m)}_{i-1,j+1,k,y}-\mathbf{v}^{(m+1)}_{i+1,j-1,k,y}+\right. \\
 & \left.\mathbf{v}m+1_{i-1,j,k-1,z}+\mathbf{v}m_{i+1,j,k+1,z}-\mathbf{v}m_{i-1,j,k+1,z}-\mathbf{v}m+1_{i+1,j,k-1,z}\right), \\
q_y=e & \left(\mathbf{v}(m+1)_{i-1,j-1,k,x}+\mathbf{v}(m)_{i+1,j+1,k,x}-\mathbf{v}(m)_{i-1,j+1,k,x}-\mathbf{v}(m+1)_{i+1,j-1,k,x}+\right. \\
 & \left.\mathbf{v}(m+1)_{i,j-1,k-1,z}+\mathbf{v}(m)_{i,j+1,k+1,z}-\mathbf{v}(m)_{i,j-1,k+1,z}-\mathbf{v}(m+1)_{i,j+1,k-1,z}\right), \\
q_z=e & \left(\mathbf{v}(m+1)_{i-1,j,k-1,x}+\mathbf{v}(m)_{i+1,j,k+1,x}-\mathbf{v}(m)_{i-1,j,k+1,x}-\mathbf{v}(m+1)_{i+1,j,k-1,x}+\right. \\
 & \left.\mathbf{v}^{(m+1)}_{i,j-1,k-1,y}+\mathbf{v}^{(m)}_{i,j+1,k+1,y}-\mathbf{v}^{(m)}_{i,j-1,k+1,y}-\mathbf{v}^{(m+1)}_{i,j+1,k-1,y}\right),
\end{array} \tag{A.14}$$

and hence, for the residual vector

$$\mathbf{r}_{i,j,k} = \omega\left(\mathbf{p} + \mathbf{q} - \mathbf{v}^{m}_{i,j,k}\right), \tag{A.15}$$

and finally, the SOR update of $\mathbf{v}_{i,j,k}$ is given by

$$\mathbf{v}^{(m+1)}_{i,j,k} = \mathbf{v}^{(m)}_{i,j,k} + \mathbf{r}_{i,j,k}. \tag{A.16}$$

A.4 Convolution Filter

The linear operator of PDE (4.9) $\mathfrak{L}$ is defined as:

$$\mathfrak{L} := \mu\nabla^2 + (\mu+\lambda)\nabla(\nabla\cdot) \tag{A.17}$$

and its eigenvalues are [23]:

$$\begin{aligned} \kappa_{1,i,j,k} &= -\pi^2(2\mu+\lambda)(i^2+j^2+k^2), \\ \kappa_{2,i,j,k} = \kappa_{3,i,j,k} &= -\pi^2\mu(i^2+j^2+k^2). \end{aligned} \tag{A.18}$$

With $\mathbf{x} \in \Omega$ and by using the shortcuts

$$\begin{aligned} scc_{i,j,k}(\mathbf{x}) &= \sin(i\pi x)\cos(j\pi y)\cos(k\pi z), \\ csc_{i,j,k}(\mathbf{x}) &= \cos(i\pi x)\sin(j\pi y)\cos(k\pi z), \\ ccs_{i,j,k}(\mathbf{x}) &= \cos(i\pi x)\cos(j\pi y)\sin(k\pi z), \end{aligned} \tag{A.19}$$

the associated eigenvectors are given by

$$\phi_{1,i,j,k}(\mathbf{x}) = \sqrt{\frac{8}{i^2+j^2+k^2}} \begin{pmatrix} i\, scc_{i,j,k}(\mathbf{x}) \\ j\, csc_{i,j,k}(\mathbf{x}) \\ k\, ccs_{i,j,k}(\mathbf{x}) \end{pmatrix}, \tag{A.20}$$

$$\phi_{2,i,j,k}(\mathbf{x}) = \sqrt{\frac{8}{i^2+j^2}} \begin{pmatrix} -j\, scc_{i,j,k}(\mathbf{x}) \\ i\, csc_{i,j,k}(\mathbf{x}) \\ 0 \end{pmatrix}, \tag{A.21}$$

$$\phi_{3,i,j,k}(\mathbf{x}) = \sqrt{\frac{8}{(i^2+j^2)(i^2+j^2+k^2)}} \begin{pmatrix} ik\, scc_{i,j,k}(\mathbf{x}) \\ jk\, csc_{i,j,k}(\mathbf{x}) \\ -(i^2+j^2)\, ccs_{i,j,k}(\mathbf{x}) \end{pmatrix}. \tag{A.22}$$

Given

$$\Gamma_{i,j,k} = 2^{\mathrm{sign}(i)+\mathrm{sign}(j)+\mathrm{sign}(k)}, \tag{A.23}$$

introducing a filter width parameter $d > 0$, $d \in \mathbb{N}$, which spawns a filter of size $2d+1$, and with the shortcut

$$\alpha_{i,j,k} = \frac{8}{\pi^2\mu(2\mu+\lambda)(i^2+j^2+k^2)^2\Gamma_{i,j,k}} \tag{A.24}$$

the components of the impulse response $\mathbf{L} \in \mathbb{R}^{3\times 3}$ of the linear operator $\mathfrak{L}$ can be written as [13]:

$$
\begin{aligned}
\mathbf{L}^x(\mathbf{y}) &= \textstyle\sum_{i,j,k=0}^{2d} \alpha_{i,j,k} scc_{i,j,k}(\mathbf{y}_c) \begin{pmatrix} (\mu i^2 + (2\mu+\lambda)(j^2+k^2))scc_{i,j,k}(\mathbf{y}+\mathbf{y_c}) \\ -(\mu+\lambda)ij\, csc_{i,j,k}(\mathbf{y}+\mathbf{y}_c) \\ -(\mu+\lambda)ik\, ccs_{i,j,k}(\mathbf{y}+\mathbf{y}_c) \end{pmatrix}, \\
\mathbf{L}^y(\mathbf{y}) &= \textstyle\sum_{i,j,k=0}^{2d} \alpha_{i,j,k} csc_{i,j,k}(\mathbf{y}_c) \begin{pmatrix} -(\mu+\lambda)ij\, scc_{i,j,k}(\mathbf{y}+\mathbf{y}_c) \\ (\mu j^2 + (2\mu+\lambda)(i^2+k^2))csc_{i,j,k}(\mathbf{y}+\mathbf{y}_c) \\ -(\mu+\lambda)jk\, ccs_{i,j,k}(\mathbf{y}+\mathbf{y}_c) \end{pmatrix}, \\
\mathbf{L}^z(\mathbf{y}) &= \textstyle\sum_{i,j,k=0}^{2d} \alpha_{i,j,k} scc_{i,j,k}(\mathbf{y}_c) \begin{pmatrix} -(\mu+\lambda)ik\, scc_{i,j,k}(\mathbf{y}+\mathbf{y}_c) \\ -(\mu+\lambda)jk\, csc_{i,j,k}(\mathbf{y}+\mathbf{y}_c) \\ (\mu k^2 + (2\mu+\lambda)(i^2+j^2))ccs_{i,j,k}(\mathbf{y}+\mathbf{y}_c) \end{pmatrix},
\end{aligned}
\tag{A.25}
$$

with $\mathbf{y}_c = (0.5, 0.5, 0.5)^T$ and $\mathbf{y} \in \{y_{r,s,t} = (\frac{r}{d}, \frac{s}{d}, \frac{t}{d})^T \,|\, r,s,t \in [-d,d] \cap \mathbf{Z}\}$.

Appendix B

Algorithms

Algorithm 1 non-rigid registration based on fluid dynamics

```
$d := d_{max}$, i:=0, $\mathbf{u}(0):=\mathbf{0}$, $T := T_0$, $\hat{S} := S(T)$
calculate mismatch $m_i$ using SSD (2.12)
repeat
  $i := i+1$
  calculate $\mathbf{f}(t_i)$ (4.8)
  solve the linear PDE Eq. (4.9) for velocity $\mathbf{v}(t_i)$ and force $\mathbf{f}(t_i)$
  label:
  choose $step = \frac{d}{\nabla\mathbf{u}(\mathbf{x})\mathbf{v}(\mathbf{x})}$
  if $\min_{\mathbf{x}} \det(\mathbf{I} - u(\mathbf{x}) - step * (v(\mathbf{x}) - \nabla u(\mathbf{x}) v(\mathbf{x}))) < 0.5$ then
    $T_{\mathbf{u}} := \mathbf{x} - \mathbf{u}(\mathbf{x})$
    $T := T \oplus T_{\mathbf{u}}$, $\hat{S} := S(T)$, $\mathbf{u}$:=0
  end if
  $\mathbf{u}(\mathbf{u}) \leftarrow \mathbf{u}(\mathbf{x}) + step * (v(\mathbf{x}) - \nabla u(\mathbf{x}) v(\mathbf{x}))$
  calculate mismatch $m_i$ using (2.12)
  if $m_i > m_{i-1}$and $d > d_{min}$ then
    $d := \max(d - \Delta d, d_{min})$
    goto label
  end if
  $d := \min(d + \Delta d, d_{max})$
until $m_i > m_{i-1}$
$T := T \oplus \mathbf{u}(t_{i-1})$
$T$ is the transformation minimizing the SSD (2.12)
```

Algorithm 2 SOR

```
$\hat{\mathbf{f}} = \frac{\mathbf{f}}{6a+2b}$, select values for $maxsteps$ and $\varepsilon$
set initial $\mathbf{v}$
repeat
    for $k := 1$ to Z step 1 do
        for $j := 1$ to Y step 1 do
            for $i := 1$ to X step 1 do
                calculate $\mathbf{p}_{i,j,k}$ according to (A.13) { 24 FLOPs }
                calculate $\mathbf{q}_{i,j,k}$ according to (A.14) { 24 FLOPs }
                calculate $\mathbf{r}_{i,j,k}$ according to (A.15) { 9 FLOPs }
                update $\mathbf{v}_{i,j,k}$ according to (A.16) { 3 FLOPs }
                $r := r + \left\|\mathbf{r}_{i,j,k}\right\|^2$ 6 FLOPs
            end for
        end for
    end for
    { one iteration needs $O(66n)$ FLOPs }
    if step=1 then
        $r_{init} := r$
    end if
until $steps \geq maxsteps$ or $r < \varepsilon * r_{init}$
```

Algorithm 3 SORA

1. $\hat{r} := 0$, $m := 1$
2. calculate the first iteration over the whole domain as given in Algorithm 2, and the residue $r_{i,j,k} = \left\|\mathbf{r}_{i,j,k}\right\|$
3. if $r_{i,j,k} \geq \hat{r}$ mark $v^* \in \Im$ as to be updated in the next iteration
4. $r_{old} := r$, $r := \sum_{i,j,k} r_{i,j,k}$
5. set threshold $\hat{r}$ as given in (4.17)
6. in subsequent iterations m of Algorithm 2 update $v_{i,j,k}$ and $r_{i,j,k}$ only at marked positions, update the marks as given in step 3, and threshold $\hat{r}$ as given in step 5.

Algorithm 4 MINRES

```
select values for $maxsteps$ and $\varepsilon$
set initial $\mathbf{v}_0$
$\mathbf{r}_0 = \widetilde{\mathbf{f}} - \mathbf{A}\mathbf{v}_0$
$\bar{\mathbf{r}}_0 = \mathbf{A}\mathbf{r}_0$
$\mathbf{p}_0 = \mathbf{r}_0, \bar{\mathbf{p}}_0 = \bar{\mathbf{r}}_0, \gamma_0 = \bar{\mathbf{r}}_0 * \mathbf{r}_0$
repeat
  $\mathbf{h}_k = \mathbf{A}\mathbf{p}_k${ $O(51n)$ FLOPs }
  $\alpha_k = \frac{\gamma_k}{\bar{\mathbf{p}}_k * \mathbf{h}_k}$ { $O(2n)$ FLOPs }
  $\mathbf{v}_{k+1} = \mathbf{v}_k + \alpha_k \mathbf{p}_k$ { $O(2n)$ FLOPs }
  $\mathbf{r}_{k+1} = \mathbf{r}_k - \alpha_k \mathbf{h}_k$ { $O(2n)$ FLOPs }
  $\bar{\mathbf{r}}_{k+1} = \bar{\mathbf{r}}_k - \alpha_k * (\mathbf{A} * \bar{\mathbf{p}}_k)$ {$O( 53n)$ FLOPs }
  $\gamma_{k+1} = \bar{\mathbf{r}}_k * \mathbf{r}_k${ $O(2n)$ FLOPs }
  $\beta_k = \frac{\gamma_{k+1}}{\gamma_k}$
  $\mathbf{p}_{k+1} = \mathbf{r}_{k+1} + \beta_k * p_k${ $O(2n)$ FLOPs }
  $\bar{\mathbf{p}}_{k+1} = \bar{\mathbf{r}}_{k+1} + \beta_k * \overline{p}_k$ { $O(2n)$ FLOPs }
until $steps \geq maxsteps$ or $|\mathbf{r}_{k+1}| > \varepsilon |\mathbf{r}_0|$
{ one iteration needs $O(117n)$ FLOPs }
```

Bibliography

[1] R.H. Abraham and C.D. Shaw. *Dynamics: The Geometry of Behavior*. Addison-Wesley, Reading MA, 1992.

[2] M. N. Ahmed, S. M. Yamany, N. Mohamed, A. A. Farag, and Th Moriarty. A modified fuzzy c-means algorithm for bias field estimation and segmentation of MRI data. *IEEE Transactions on Medical Imaging*, 21(3):193–199, 2002.

[3] R. Archibald and A. Gelb. A method to reduce the Gibbs ringing artifact in MRI scans while keeping tissue boundary integrity. *IEEE Transactions on Medical Imaging*, 21 (4):304–319, 2002.

[4] R. Bajcsy and S. Kovacic. Multi-resolution elastic matching. *Computer Vision, Graphics and Image Processing*, 1(46):1–21, 1989.

[5] B. Bargen and T. P Donnelly. *Inside DirectX (Microsoft Programming Series)*. Microsoft Press, 1998.

[6] H. J. M. Barnett, J. P. Mohr, B. M. Stein, and F. M. Yatsu (Eds.). *Stroke: Pathophysiology, diagnosis, and management*. Churchill Livingstone, New York, 3rd edition, 1998.

[7] R. Barrett, M. Berry, T. F. Chan, J. Demmel, J. M. Donato, J. Dongarra, V. Eijkhout, R. Pozo, Ch. Romine, and H. Van der Vorst. Templates for the solution of linear systems: Building blocks from iterative methods. SIAM, http://www.netlib.org/templates/templates.ps, 1993.

[8] W. Beil, K. Rohr, and H. S. Stiel. Investigation of approaches for the localization of anatomical landmarks in 3d medical images. In H. U. Lemke, M. W. Vannier, and K. Inamura (Eds.), *Proc. Computer Assisted Radiology and Surgery (CAR'97)*, pp. 265–270, Amsterdam Lausanne, 1997. Elsevier.

[9] J. L. Bentley. *Writing Efficient Programs*. Prentice-Hall, Englewood Cliffs, N. J., 1982.

[10] F. L. Bookstein. Principal warps: Thin-plate splines and the decomposition of deformations. *IEEE Transactions on Pattern Analysis and Machine Intelligence*, 11(6): 567–585, 1989.

[11] F. L. Bookstein. *Morphometric Tools for Landmark Data*. Cambridge University Press, New York, 1991.

[12] Ch. Brady. Memtest86 - a stand-alone memory diagnostic. http://www.memtest86.com/, 2000.

[13] M. Bro-Nielsen. *Medical Image Registration and Surgery Simulation*. PhD thesis, Technical University of Denmark, 1996.

[14] M. Bro-Nielsen and C. Gramkov. Fast fluid registration of medical images. In *Visualisation in biomedical computing (VBC'96)*, volume 1131 of *Lecture Notes in Computer Science*, pp. 267–276, Hamburg, 1996. Springer-Verlag.

[15] I.N. Bronstein, K.A. Semendjajew, G. Musiol, and H. Mühlig. *Taschenbuch der Mathematik*. Verl. Harri Deutsch, Thun; Frankfurt am Main, 5th edition, 1995.

[16] M. A. Brown and R. C. Semelka. *MRI : Basic Principles and Applications*. Wiley, New York, 2nd edition, 1995.

[17] D. R. Butenhof. *Programming with POSIX threads*. Addison-Wesley, Massachussets, 1999.

[18] B. Cabral and L. Leedom. Imaging vector fields using line integral convolution. In *Proceedings of SIGGRAPH '93*, volume 27 of *Computer Graphics*, pp. 263–272, Anaheim, California, 1993. ACM SIGGRAPH.

[19] P. Cachier, X. Pennec, and N. Ayache. Fast non-ridgid matching by gradient descent: study and improvements of the "demons"algorithm. Technical Report 3706, INRIA, Sophia-Antipolis, 1999.

[20] C. Chalopin and F. Kruggel. Automatic segmentation of focal brain lesions from MR images. IEEE Transactions on Medical Imaging: Submitted, 2002.

[21] C. N. Chen and D. I. Hoult. *Biomedical Magnetic Reconance Technology*. Adam Hilger, Bristol, New York, 1989.

[22] M. Chen, T. Kanade, D. Pomerleau, and H. A. Rowley. Anomaly detection through registration. *Pattern Recognition*, 1(32):113–128, 1999.

[23] G. E. Christensen. *Deformable shape models for neuroanatomy*. DSc.-thesis, Server Institue of Technology, Washington University, Saint Louis, 1994.

[24] G. E. Christensen, Rabbitt. R. D., and M. I. Miller. Deformable templates using large deformation kinematics. *IEEE Transactions on Medical Imaging*, 5(10):1435–1447, 1996.

[25] G. E. Christensen, M. I. Miller, and M. Vannier. A 3d deformable magnetic resonance textbook based on elasticy. In *AAAI Spring Symposium Series: Applications of Computer Vision in Medical Image Processing*, pp. 153–156. Stanford University, 1994.

[26] G. E. Christensen, R. D. Rabbit, and M. I. Miller. 3D brain mapping using deformable neuroanatomy. *Physics in Medicine and Biology*, 39:609–618, 1994.

[27] M.K. Chung, K.J. Worsley, T. Paus, C. Cherif, D.L. Collins, J.N. Giedd, J.L. Rapoport, and A.C. Evans. A unified statistical approach to deformation-based morphometry. *NeuroImage*, 14:595–606, 2001.

[28] A. Collignon, F. Maes, D. Delaere, D. Vandermeulen, P. Suetens, and Marchal G. Automated multi-modal image registration based on information theory. In Y. Bizais and R. Di Paola (Eds.), *Information Processing in Medical Imaging*, pp. 263–274, Amsterdam, 1995. Kluwer Academic Publishers.

[29] R. Crawfis and N. Max. Texture splats for 3d scalar and vector field visualization. In Gregory M. N. and D. Bergeron (Eds.), *Visualization '93*, pp. 261–266, San Jose, 1994. IEEE Computer Society Press.

[30] C. Davatzikos and R. N. Bryan. Using a deformable surface model to obtain a mathematical representation of the cortex. *IEEE Transactions on Medical Imaging*, 15(6): 785–795, 1996.

[31] C. A. Davatzikos, J. L. Prince, and R. N. Bryan. Image registration based on boundary mapping. *IEEE Transactions on Medical Imaging*, 15(1):112–115, 1996.

[32] L. K. de Leeuw and J. J van Wijk. Enhanced spot noise vector field visualization. In G. M. Nielson and D. Silver (Eds.), *IEEE Visualization*, pp. 233–239, Los Alamitos (CA), 1995. IEEE Computer Society Press.

[33] W. C. de Leeuw and J. J. van Wijk. A probe for local flow field visualization. In G. M. Nielson and D. Bergeron (Eds.), *Visualization '93*, pp. 39–45, San Jose, 1993. IEEE Computer Society Press.

[34] D. H. Eberly. *3D Game Engine Design - A Practical Approach to Real-Time Computer Graphics*. Academic Press, 2001.

[35] G. Engeln-Müllges and F. Reutter. *Formelsammlung zur Numerischen Mathematik mit Turbo Pascal Programmen*. Bibliographisches Institut & F. A. Brockhaus AG, Mannheim, 3rd edition, 1991.

[36] A. C. Evans, W. Dai, L. Collins, P. Neelin, and S. Marret. Warping of a computerized 3-d atlas to match brain image volumes for quantitative neuroanatomical and functional analysis. In *Proc. SPIE Medical Imaging V (1445)*, pp. 236–246, Bellingham (WA), 1991. SPIE Press.

[37] B. Fischer and J. Modersitzki. A super fast registration algorithm. In H. Handels, A. Horsch, T. Lehmann, and H.-P. Meinzer (Eds.), *Bildverarbeitung für die Medizin*, Informatik aktuell, pp. 169–173, Berlin, 2001. Springer-Verlag.

[38] M. Fornefett, K. Rohr, R. Sprengel, and H. S. Stiehl. Incorporating orientation attributes in landmark-based elastic medical image registration. In H. Niemann, H.-P. Seidel, and B. Girod (Eds.), *Proc. Image and Multidimensional Digital Signal Processing (IMDSP'98)*, pp. 37–40. infix Verlag, Sankt Augustin, 1998.

[39] L. K. Forsell. Visualizing flow over curvilinear grid surfaces using line intregral convolution. In R. D. Bergeron and A. E Kaufmann (Eds.), *Proceedings of Visualization '94*, pp. 240–247, Los Alamitos (CA), 1994. IEEE Computer Society Press.

[40] N. C. Fox, S. Cousens, R. Scahill, R. J. Harvay, and M. N Rossor. Using serial registered brain magnetic resonance imaging to measure disease progression in Alzheimer disease. *Archives of Neurology*, 57(3):339–344, 2000.

[41] S. Frantz, K. Rohr, and H. S. Stiehl. On the localization of 3d anatomical point landmarks in medical imagery using multi-step differential approaches. In F. Wahl and E. Paulus (Eds.), *19. DAGM-Symposium Mustererkennung*, pp. 340–347, Berlin, 1997. Springer-Verlag.

[42] S. Frantz, K. Rohr, and H. S. Stiehl. Refined localisation of three dimensional anatomical point landmarks using multi-step differential approaches. In K.M. Hanson (Ed.), *Proc. SPIE's International Symposium Medical Imaging 1998: Image Processing*, volume 3338, pp. 28–38, Bellingham (WA), 1998. SPIE, SPIE Press.

[43] P. A. Freeborough, N. C. Fox, and R. I. Kitney. Interactive algorithms for the segmentation and quantitation of 3-D MRI brain scans. *Computer Methods and Programs in Biomedicine*, 53:15–25, 1997.

[44] St. S. Fried. Pentium optimizations and numeric performance. *Dr. Dobbś Journal*, 1995. URL `http://www.ddj.com/documents/s=995/ddj9501a/9501a.htm`.

[45] D. E. Goldberg. *Genetic algorithms in search, optimization, and machine learning*. Addison-Wesley, Reading, Mass., 1989.

[46] A. Goshtasby, S. H. Gage, and J. F. Bartholic. A two-stage cross-correlation approach to template matching. *IEEE Transactions on Pattern Analysis and Machine Intelligence*, 6(3):374–378, 1984.

[47] D. H. Gottlieb and G. Samaranayake. The index of discontinuous vector fields. *New York Journal of Mathematics*, 1:130–148, 1995.

[48] B. Greer and G. Henry. High performance software on Intel pentium pro processors or micro-ops to teraflops. http://www.supercomp.org/sc97/proceedings/TECH/GREER/INDEX.HTM, 1997.

[49] U. Grenander and M. I. Miller. Computational anatomy: An emerging discipline. *Quarterly of Applied Mathematics*, pp. 617–694, 1998.

[50] G.M. Grimshaw, A. Adelstein, M.P. Bryden, and G.E. MacKinnon. First-language acquisition in adolescence: evidence for a critical period for verbal language development. *Brain and Language*, 63:237–255, 1998.

[51] A. P. Guéziec, X. Pennec, and N. Ayache. Medical image registration using geometric hashing. *IEEE Computional Science & Engineering*, 4(4):29–41, 1997.

[52] E.M. Haacke, Z.-P. Liang, and F. Boada. Image reconstruction using projection onto convex sets, model constraints and linear prediction theory for the removal of phase, motion, and gibbs artifacts in magnetic resonance and ultrasound imaging. *Optical Engineering*, 29:555–566, 1990.

[53] H. C. Hege and K. Polthier (Eds.). *Mathematical visualization : Algorithms, applications and numerics*. Springer, Berlin, 1998.

[54] F. Heitz, P. Perez, and P. Bouthemy. Multiscale minimization of global energy functions in some visual recovery problems. *Computer Vision, Graphics, and Image Processing*, 59(1):125–134, 1994.

[55] J. L. Helman and L. Hesselink. Representation and display of vector field topology in fluid flow data sets. *IEEE Computer*, 22(8):27–36, 1989.

[56] Th. Hierl and A. Hemprich. A novel modular retention system for midface distraction osteogenesis. *British Journal of Oral and Maxillofacial Surgery*, 38:623–626, 2000.

[57] Th. Hierl, R. Klöppel, and A. Hemprich. Midface distraction osteogenesis without major osteotomies: A report on the first clinical application. *Plastic and Reconstruction Surgery*, 108(6):1667–1672, 2001.

[58] A. J. S. Hin and F. H. Post. Visualization of turbulent flow with particles. In G. Nielson and R. Bergeron (Eds.), *Visualization '93*, pp. 46–52. IEEE Computer Society Press, 1993.

[59] M. Holden, D. L. G. Hill, E. R. E. Denton, J. M. Jariosz, T. C. S. Cox, and D. J. Hawkes. Voxel similarity measures for 3D serial MR brian image registration. In A. Kuba, M. Sámal, and A. Todd-Pokropek (Eds.), *Information Processing in Medical Imaging*, volume 1613 of *Lecture Notes in Computer Science*, pp. 472–477. Springer-Verlag, Berlin, 1999.

[60] H.H. Hoppe, T. DeRose, T. Duchamp, J.A. McDonald, and W. Stuetzle. Mesh optimization. In J. T. Kajiya (Ed.), *SIGGRAPH '93 Proceedings*, volume 27 of *Computer Graphics*, pp. 19–26, Anaheim (CA), 1993.

[61] IBM. Open visualization data explorer. http://www.research.ibm.com/dx/, 2001.

[62] S. C. Joshi and M. I. Miller. Landmark matching via large deformation diffeomorphisms. *IEEE Transactions on Medical Imaging*, 9(8):1357–1370, 2000.

[63] A. C. Kak and M. Slaney. *Principles of Computerized Tomographic Imaging*. Society of Industrial and Applied Mathematics, Philadelphia (PA), 2001.

[64] F. Kruggel and D. Barber. Image processing design report. Technical Report Deliverable 1.1a, http://www.ccrl-nece.de/simbio/ReportsEvents/deliverables.shtml, 2000.

[65] F. Kruggel and D.Y. von Cramon. Measuring the cortical thickness. In B. Werner (Ed.), *Workshop on Mathematical Methods in Biomedical Image Analysis*, pp. 154–161, Los Alamitos (CA), 2000. IEEE Computer Society. Peer-reviewed Proceedings.

[66] J.-H. Lee, M. Garwood, R. Menon, G. Adriany, P. Andersen, Ch. L. Truwit, and K. Ugurbil. High contrast and fast three-dimensional magnetic resonance imaging at high fields. *Magnetic Resonance in Medicine*, 34:308–312, 1995.

[67] L. Lemieux, R. S. N. Liua, and J. S. Duncan. Hippocampal and cerebellar volumetry in serially acquired MRI volume scans. *Magnetic Resonance Imaging*, 18(8):1027–1033, 2000.

[68] L. Lemieux, U. C. Wieshmann, N. F. Moran, D. R. Fish, and S. D. Shorvon. The detection and significance of subtle changes in mixed-signal brain lesions by serial MRI scan matching and spatial normalisation. *Medical Image Analysis*, 3(2):227–242, 1998.

[69] H. Lester, S. R. Arridge, K. M. Jansons, L. Lemieux, J. V. Hajnal, and A. Oatridge. Non-linear registration with variable viscosity fluid algorithm. In A. Kuba, M. Sámal, and A Todd-Pokropek (Eds.), *Information Processing in Medical Imaging*, volume 1613 of *Lecture Notes in Computer Science*, pp. 238–251. Springer-Verlag, Berlin, 1999.

[70] P. Lindstrom and G. Turk. Evaluation of memoryless simplification. *IEEE Transactions on Visualization and Computer Graphics*, 5(2):98–115, 1999.

[71] N. Lu. *Fractal Imaging*. Academic Press, San Diego, CA, 1997.

[72] K.-L. Ma and Ph. J. Smith. Virtual smoke: An interactive 3d flow viualisation technique. In A. Kaufman and G. Nielson (Eds.), *Visualization '92*, pp. 46–52, Los Alamitos (CA), 1992. IEEE Computer Society Press.

[73] F. Maes, A. Collignon, D. Vandermeulen, G. Marchal, and P. Suetens. Multimodality image registration by maximization of mutual information. *IEEE Transactions on Medical Imaging*, 2(16):187–198, 1997.

[74] J. B. A. Maintz and M. A. Viergever. A survey of medical image registration. *Medical Image Analysis*, 2(1):1–36, 1998.

[75] G. Malandain and J.-M. Rocchisani. Matching of 3d medical images with a potential based method. Technical report, INRIA Sophia-Antipolis, 1993.

[76] J. A. Markisz and J. P. Whalen (Eds.). *Principles of MRI (seleted topics).* Appelton & Lange, Stamford, Connecticut, 1998.

[77] W. Marquardt, D. An algorithm for least-square estimation of nonlinear parameters. *Journal of the Society for Industrial and Applied Mathematics*, 11(2):431–441, 1963.

[78] G. McKahn, D. Drachmann, M. Folstein, R. Katzman, D. Price, and E. M. Stadian. Clinical diagnosis of Alzheimer's disease: Report of the NINCDS-ADRA work group under the auspices of the department of helth and human services task force on Alzheimer's disease. *Neurology*, 34:839–944, 1994.

[79] O. Musse, F. Heitz, and J.-P. Armspach. Topology preserving deformable image matching using constrained hierarchical parametric models. *IEEE Transactions on Image Processing*, 10(7):1087–1093, 2001.

[80] P. Ning and J. Bloomenthal. An evaluation of implicit surface tilers. *Computer Graphics*, 13(6):33–41, 1993.

[81] L. G. Nyúl and J. K. Udupa. New variants of a method of MRI scale normalization. In A. Kuba, M. Sámal, and A. Todd-Pokropek (Eds.), *Information Processing in Mediacal Imaging (IPMI'99)*, volume 1613 of *Lecture Notes in Computer Science*, pp. 490–495, Berlin, 1999. Springer.

[82] C. C. Paige and M. A. Saunders. Solution of sparse indefinit systems of linear equations. *SIAM Journal of Numerical Analysis*, 12(4):866–869, 1975.

[83] B. Paul. The mesa 3d graphics library. http://www.mesa3d.org, 1999.

[84] W. Peckar, Ch. Schnörr, K. Rohr, and H. S. Stiel. Parameter-free elastic deformation approach for 2-d and 3-d registration using prescribed displacements. *Journal of Mathematical Imaging and Vision*, 10(2):143–162, 1999.

[85] D. L. Pham and J. L. Prince. An adaptive fuzzy C-means algorithm for image segmentation in the presence of intensity inhomogeneities. *Pattern Recognition Letters*, 20: 57–68, 1999.

[86] P. A. Philippou and R. N. Strickland. Vector field analysis and synthesis using three-dimensional phase portraits. *Graphical Models and Image Processing*, 6(59):466–462, 1997.

[87] J. W. Polley and A. A. Figueroa. Management of servere maxillary deficiency in childhood and adolescence through distraction osteogenesis with an external, adjustable, rigid distration device. *Journal of Craniofacial Surgery*, 8(3):181–185, 1997.

[88] J. W. Polley and A. A. Figueroa. Rigid external distraction: Its application in cleft maxillary deformities. *Plastic and Reconstructive Surgery*, 102(5):1360–1372, 1998.

[89] F. J. Post, T. van Walsum, and F. H. Post. Iconic techniques for feature visualization. In G. M. Nielson and D. Silver (Eds.), *Visualization '95*, pp. 288–295, Los Alamitos (CA), 1995. IEEE Computer Society Press.

[90] W. H. Press, S. A. Teukolsky, W. T. Vetterling, and B. P. Flannery. *Numerical Recipes in C*. Cambridge University Press, New York, 2nd edition, 1992.

[91] D. Rey, G. Subsol, H. Delingette, and N. Ayache. Automatic detection and segmentation of evolving processes in 3D medical images: Application to multiple sclerosis. In A. Kuba, M. Sámal, and A. Todd-Pokropek (Eds.), *Information Processing in Medical Imaging*, volume 1613 of *Lecture Notes in Computer Science*, pp. 154–167. Springer-Verlag, Berlin, 1999.

[92] A. Roche, G. Malandain, X. Pennec, and N. Ayache. Multimodal image registration by maximization of the correlation ratio. Technical report, INRIA Sophia-Antipolis, 1998.

[93] K. Rohr, R. Sprengel, and H. S. Stiehl. Incorporation of landmark error ellipsoids for images registration based on approximating thin-plate splines. In H. U. Lemke, M. W. Vannier, and K. Inamura (Eds.), *Computer Assisted Radiology and Surgery (CAR'97)*, pp. 234–239, Amsterdam, 1997. Elsevier Science.

[94] K. Rohr, H. S. Stiehl, R. Sprengel, T. M. Buzug, J. Weese, and M. H. Kuhn. Landmark-based elastic registration using approximating thin-plate splines. *IEEE Transactions on Medical Imaging*, 20(6):526–543, 2001.

[95] G. Scheuermann, H. Hagen, and H. Krüger. Clifford algebra in vector field visualization. In H.-C. Hege and K. Polthier (Eds.), *Mathematical Visualization*, pp. 343–351. Springer-Verlag, Heidelberg, 1998.

[96] W. Schroeder, K.W. Martin, and B. Lorensen. *The Visualization Toolkit: An Object-Oriented Approach to 3D Graphics*. Prentice-Hall, Upper Saddle River (NJ), 1996.

[97] L. A. Segel. *Mathematics Applied to Continuum Mechanics*. Dover Publishing, New York, 1987.

[98] D. Shreiner (Ed.). *OpenGL Reference Manual*. Addison Wesley, 3rd edition, 1999.

[99] R. Southwell. *Relaxation Methods in Engineering Science - a Treatise in Approximate Computation*. Oxford University Press, Oxford, England, 1940.

[100] L. H. Staib and X. Lei. Intermodality 3d medical image registration with global search. In M. E. Kavanaugh (Ed.), *Proceedings of the IEEE Workshop on Biomedical Image Analysis*, pp. 225–234, Los Alamitos (CA), 1994. IEEE Computer Society Press.

[101] D. Stalling and H.C. Hege. Fast and resolution independent line integral convolution. In S. G. Mair, G. S. Owen, K. Sullivan, J. McCord, and Th. A. DeFanti (Eds.), *Proceedings of SIGGRAPH '95*, pp. 249–256, Los Alamitos (CA), 1995. ACM SIGGRAPH.

[102] C. Studholme, D. J. Hawkes, and D. L. G. Hill. An overlap invariant entropy measure of 3d medical image alignment. *Pattern Recognition*, 32(1):71–86, 1999.

[103] J. Talairach and P. Tournoux (Eds.). *Co-Planar Stereotaxic Atlas of the Human Brain. 3-Dimensional Proportional System: An Approach to Cerebral Imaging*. Thieme, Stuttgart, 1988.

[104] P. Thévenaz. Intramodal registration software. http://bigwww.epfl.ch/thevenaz/registration/, 1997.

[105] P. Thévenaz, U. E. Ruttimann, and M. Unser. Iterative multi-scale registration without landmarks. In B. Werner (Ed.), *Proceedings of the 1995 IEEE International Conference on Image Processing (ICIP'95)*, volume III, pp. 228–231, Los Alamitos (CA), 1995. IEEE Computer Society.

[106] J. P. Thirion. New feature points based on geometric invariants for 3d image registration. Technical report, INRIA Sophia-Antipolis, 1993.

[107] J. P. Thirion. Fast non-rigid matching of 3d medical images. Technical report, INRIA Sophia-Antipolis, 1995.

[108] P. M. Thompson, J. N. Giedd, R. P. Woods, D. MacDonalds, A. C. Evans, and A. W. Toga. Growth patterns in the developing human brain detected using continuum mechanical tensor mapping. *Nature*, 404(6774):190–193, 2000.

[109] P. M. Thompson, D. MacDonalds, M. S. Mega, C. J. Holmes, A. C. Evans, and A. W. Toga. Detection and mapping of abnormal brain structure with a probabilistic atlas of cortical surfaces. *Journal of Computer Assisted Tomography*, 21(4):567–581, 1997.

[110] P. M. Thompson and A. W. Toga. *Brain Warping*. Academic Press, San Diego, 1998.

[111] K. Ugurbil, M. Garwood, J. Ellermann, K. Hendrich, R. Hinke, X. Hu, S.-G. Kim, R. Menon, H. Merkle, S. Ogawa, and R. Salmi. Magnetic fields: Initial experiences at 4t. *Magn. Reson. Quart.*, 9:259, 1993.

[112] M. Unser. Multigrid adaptive image processing. In B. Werner (Ed.), *International Conference on Image Processing (ICIP'95)*, volume I, pp. 49–52, Los Alamitos (CA), 1995. IEEE, IEEE Computer Society.

[113] J. J. van Wijk. Rendering surface-particles. In A. Kaufman and G. Nielson (Eds.), *Visualization '92*, pp. 54–61. IEEE Computer Society Press, 1992.

[114] A. R. Varma, J. S Snowden, J. J. Lloyd, P. R. Talbot, D. M. A. Mann, and D. Neary. Evaluation of the NINCDA-ADRDA criteria in the differentiation of Alzheimer's disease and fronto temporal dementia. *Journal of Neurology, Neurosurgery and Psychiatry*, 2(66):184–188, 1999.

[115] P. A. Viola. *Alignment by Maximization of Mutual Information*. PhD thesis, Massachusetts Institute of Technology, Cambridge (MA), 1995.

[116] K. Wadleigh and I. Crawford. *Software Optimization for High Performance Computing: Creating Faster Applications*. Prentice Hall, New Jersey, 2000.

[117] G. Wang, D. L. Snyder, J. A. O'Sullivan, and M. W. Vannier. Iterative deblurring for CT metal artifact reduction. *IEEE Transactions on Medical Imaging*, 15(5):657–664, 1996.

[118] P. Wesseling. *An Introduction To Multigrid Methods*. John Wiley & Sons Inc., Chichester, England, 1992.

[119] G. Wollny. Mia - a toolchain for medical image analysis. http://mia.sourceforge.net, 2002.

[120] G. Wollny and F. Kruggel. Computational cost of non-rigid registration algorithms based on fluid dynamics. *IEEE Transactions on Medical Imaging*, 11(8):946–952, 2002.

[121] G. Wollny, M. Tittgemeyer, and F. Kruggel. Segmentation of vector fields by critical point analysis: Application to brain deformation. In R. Kasturi, D. Laurendeau, and D. Suen (Eds.), *Proceedings of the 16th International Conference on Pattern Recognition*, pp. 524–527, Quebec City, Canada, 2002. IAPR.

[122] M. Woo, J. Neider, T. Davis, and D. Shreiner. *OpenGL Programming Guide*. Addison Wesley, Reading (MA), 3rd edition, 1999.

Curriculum Vitae

Name: Gert Wollny
Date of birth: 31. August 1968
Place of birth: Leipzig, Germany
Parent: Peter and Karin Wollny
Citizenship: German

1975-1983	Primary school in Leipzig
1983-1987	Extended school in Riesa (aimed education with focus on natural science)
1990 -1996	Studies of mathematics at the University of Leipzig
1996	Diploma thesis: “Ein Vergleich der Verfahren zur Lösung großdimensionaler, linear restringierter Verfahren von C. Kanzow sowie A. Friedlander, J. M. Martinez und S. A. Santos” (A Comparison of the Methods on the Solution of Linearly Constrained Minimization Problems introduced by C. Kanzow and by A. Friedlander, J. M. Martinez and S. A. Santos)
1996-1997	Freelance software developer
1997-1998	Software developer at the CTI- GmbH Leipzig
since 1998	Research associate at the Max-Planck-Institute of Cognitive Neuroscience in Leipzig, Department of Neurology, Work Group on Signal and Image Processing

Publications

Journal papers:

- Wollny, G. and Kruggel, F., Computational cost of non-rigid registration algorithms based on fluid dynamics, *IEEE Transactions on Medical Imaging*, 11(8), pp. 946-952, 2002
- Tittgemeyer, M., Wollny, G. and Kruggel, F., Visualizing deformation fields computed by non-linear image registration, *Computing and Visualization in Science*, 5(1), pp. 45-51, 2002

Conference proceedings

- Wollny, G., Tittgemeyer, M. and Kruggel, F., Segmentation of Vector Fields by Critical Point Analysis: Application to Brain Deformation, In Kasturi, R. and Laurendeau, D. and Suen, D. (Eds.), *Proceedings of the 16th International Conference on Pattern Recognition*, pp. 524-527, Quebec City, Canada, 2002
- Tittgemeyer, M., Wollny, G. and Kruggel, F., Monitoring structural change in the brain: Application to neurodegeneration, In J. Sporring, W. Niessen and J. Weickert (Eds.), *Proceedings of the International Workshop on Growth and Motion in 3D Medical Images*, pp. 9-16, 3D Lab-University of Copenhagen, 2002
- Wollny, G., Hierl, Th., Kruggel, F. and and Klöppel, R., Die Analyse von Zeitreihen am Beispiel einer suturalen Mittelgesichtsdistraktion In Handels, H., Horsch, A., Lehmann, T. and Meinzer, H.P. (Eds.), *Bildverabeitung für die Medizin*, pp. 63-66, Berlin: Springer, 2002
- Wollny, G. and Kruggel, F., Analyse von pathologischen Veränderungen in MRT-Zeitreihenaufnahmen In Handels, H., Horsch, A., Lehmann, T. and Meinzer, H.P. (Eds.), *Bildverabeitung für die Medizin*, pp. 275-279, Berlin: Springer, 2001

Published abstracts

- Tittgemeyer, M., Wollny, G. and Kruggel, F, Inverse bio-mechanical models of the human brain - Clinical application, *Proceeding: Workshop on Visual Analysis, Image*

Based Computing and Applications, http://www.icm.edu.pl/visual/, Warshaw, Poland, 2002

Talks

- Wollny, G., Hierl, Th. and Kruggel, F., Zeitreihenaufnahmen in der Analyse von Mittelgesichtsdistraktionen, *52. Kongress der Deutschen Gesellschaft für Mund-, Kiefer- und Gesichtschirurgie* Leipzig, Germany, 2002
- Wollny, G., Hierl, Th., Kruggel, F. and and Klöppel, R. Die Analyse der suturalen Mittelgesichtsdistraktion, *1. Jahrestagung der Deutschen Gesellschaft für Computer- und Roboter assistierte Chirurgie e.V. (CURAC 2002)*, Leipzig, Germany, 2002

Selbstständigkeitserklärung

Hiermit erkläre ich, die vorliegende Dissertation selbständig und ohne unzulässige fremde Hilfe angefertigt zu haben. Ich habe keine anderen als die angeführten Quellen und Hilfsmittel benutzt und sämtliche Textstellen, die wörtlich oder sinngemäß aus veröffentlichten oder unveröffentlichten Schriften entnommen wurden, und alle Angaben, die auf mündlichen Auskünften beruhen, als solche kenntlich gemacht. Ebenfalls sind alle von anderen Personen bereitgestellten Materialien oder erbrachten Dienstleistungen als solche gekennzeichnet.

Leipzig,

MPI Series for Human Cognitive and Brain Sciences:

1 Anja Hahne

Charakteristika syntaktischer und semantischer Prozesse bei der auditiven Sprachverarbeitung: Evidenz aus ereigniskorrelierten Potentialstudien

2 Ricarda Schubotz

Erinnern kurzer Zeitdauern: Behaviorale und neurophysiologische Korrelate einer Arbeitsgedächtnisfunktion

3 Volker Bosch

Das Halten von Information im Arbeitsgedächtnis: Dissoziationen langsamer corticaler Potentiale

4 Jorge Jovicich

An investigation of the use of Gradient- and Spin-Echo (GRASE) imaging for functional MRI of the human brain

5 Rosemary C. Dymond

Spatial Specificity and Temporal Accuracy in Functional Magnetic Resonance Investigations

6 Stefan Zysset

Eine experimentalpsychologische Studie zu Gedächtnisabrufprozessen unter Verwendung der funktionellen Magnetresonanztomographie

7 Ulrich Hartmann

Ein mechanisches Finite-Elemente-Modell des menschlichen Kopfes

8 Bertram Opitz

Funktionelle Neuroanatomie der Verarbeitung einfacher und komplexer akustischer Reize: Integration haemodynamischer und elektrophysiologischer Maße

9 Gisela Müller-Plath

Formale Modellierung visueller Suchstrategien mit Anwendungen bei der Lokalisation von Hirnfunktionen und in der Diagnostik von Aufmerksamkeitsstörungen

10 Thomas Jacobsen

Characteristics of processing morphological structural and inherent case in language comprehension

11 Stefan Kölsch

Brain and Music
A contribution to the investigation of central auditory processing with a new electrophysiological approach

12 Stefan Frisch

Verb-Argument-Struktur, Kasus und thematische Interpretation beim Sprachverstehen

13 Markus Ullsperger

The role of retrieval inhibition in directed forgetting – an event-related brain potential analysis

14 Martin Koch

Measurement of the Self-Diffusion Tensor of Water in the Human Brain

15 Axel Hutt

Methoden zur Untersuchung der Dynamik raumzeitlicher Signale

16 Frithjof Kruggel

Detektion und Quantifizierung von Hirnaktivität mit der funktionellen Magnetresonanztomographie

17 Anja Dove

Lokalisierung an internen Kontrollprozessen beteiligter Hirngebiete mithilfe des Aufgabenwechselparadigmas und der ereigniskorrelierten funktionellen Magnetresonanztomographie

18 Karsten Steinhauer

Hirnphysiologische Korrelate prosodischer Satzverarbeitung bei gesprochener und geschriebener Sprache

19 Silke Urban

Verbinformationen im Satzverstehen

20 Katja Werheid

Implizites Sequenzlernen bei Morbus Parkinson

21 Doreen Nessler

Is it Memory or Illusion? Electrophysiological Characteristics of True and False Recognition

22 Christoph Herrmann

Die Bedeutung von 40-Hz-Oszillationen für kognitive Prozesse

23 Christian Fiebach

Working Memory and Syntax during Sentence Processing.
A neurocognitive investigation with event-related brain potentials and functional magnetic resonance imaging

24 Grit Hein

Lokalisation von Doppelaufgabendefiziten bei gesunden älteren Personen und neurologischen Patienten

25 Monica de Filippis

Die visuelle Verarbeitung unbeachteter Wörter.
Ein elektrophysiologischer Ansatz

26 Ulrich Müller

Die katecholaminerge Modulation präfrontaler kognitiver Funktionen beim Menschen

27 Kristina Uhl

Kontrollfunktion des Arbeitsgedächtnisses über interferierende Information

28 Ina Bornkessel

The Argument Dependency Model: A Neurocognitive Approach to Incremental Interpretation

29 Sonja Lattner

Neurophysiologische Untersuchungen zur auditorischen Verarbeitung von Stimminformationen

30 Christin Grünewald

Die Rolle motorischer Schemata bei der Objektrepräsentation: Untersuchungen mit funktioneller Magnetresonanztomographie

31 Annett Schirmer

Emotional Speech Perception: Electrophysiological Insights into the Processing of Emotional Prosody and Word Valence in Men and Women

32 André J. Szameitat

Die Funktionalität des lateral-präfrontalen Cortex für die Verarbeitung von Doppelaufgaben

33 Susanne Wagner

Verbales Arbeitsgedächtnis und die Verarbeitung ambiger Wörter in Wort- und Satzkontexten

34 Sophie Manthey

Hirn und Handlung: Untersuchung der Handlungsrepräsentation im ventralen prämotorischen Cortex mit Hilfe der funktionellen Magnet-Resonanz-Tomographie

35 Stefan Heim

Towards a Common Neural Network Model of Language Production and Comprehension: fMRI Evidence for the Processing of Phonological and Syntactic Information in Single Words

36 Claudia Friedrich

Prosody and spoken word recognition: Behavioral and ERP correlates

37 Ulrike Lex

Sprachlateralisierung bei Rechts- und Linkshändern mit funktioneller Magnetresonanztomographie

38 Thomas Arnold

Computergestützte Befundung klinischer Elektroenzephalogramme

39 Carsten H. Wolters

Influence of Tissue Conductivity Inhomogeneity and Anisotropy on EEG/MEG based Source Localization in the Human Brain

40 Ansgar Hantsch

Fisch oder Karpfen? Lexikale Aktivierung von Benennungsalternativen bei der Objektbenennung

41 Peggy Bungert

Zentralnervöse Verarbeitung akustischer Informationen
Signalidentifikation, Signallateralisation und zeitgebundene Informationsverarbeitung bei Patienten mit erworbenen Hirnschädigungen

42 Daniel Senkowski

Neuronal correlates of selective attention: An investigation of electrophysiological brain responses in the EEG and MEG